New insights on dust properties from Planck intensity and polarization data

Lapo Fanciullo

NNT: 2015SACLS194

Thèse de Doctorat
de
L'Université Paris-Saclay
Preparée à
L'institut d'Astrophysique Spatiale d'Orsay

Ecole Doctorale n° 127
Astronomie et Astrophysique d'Île-de-France

Specialité de doctorat: Sciences de l'Univers

Par

M. Lapo Fanciullo

Nouveaux aperçus sur les propriétés des poussières
à partir des données Planck en intensité et polarisation

New insights on dust properties
from Planck intensity and polarization data

Thèse présentée et soutenue à Orsay, le 16 Décembre 2015

Composition du Jury:

M. Laurent Verstraete (Professeur, IAS, Orsay): Président
M. Ralf Siebenmorgen (Senior Astronomer, ESO, Garching): Rapporteur
M. Mika Juvela (University Lecturer, University of Helsinki): Rapporteur
Mme Karine Demyk (CR, IRAP, Toulouse): Examinatrice
M. Frédéric Galliano (CR, SAp, Saclay): Examinateur
M. Vincent Guillet (MCF, IAS, Orsay): Directeur de thèse
M. François Boulanger (DR, IAS, Orsay): Co-directeur de thèse

Acknowledgements

When I started my Ph.D. I had no idea how big really was the task before me. And, of course, I had no idea to how many people I would owe a debt of gratitude for helping me get to the end of this. I cannot thank each and every one of them, for if I did the acknowledgement section would be longer than the manuscript proper. Everyone who got me out of a problem (whether scientific, informatic or organizational), everyone who helped me put my worries in context and realize my worth, everyone who contributed towards making these three years not only an apprenticeship, but a truly enriching experience – all of them should know that they have my gratitude, even if not in ink on paper.

This said, some contributions are too important not to acknowledge explicitly. All my gratitude goes to Vincent Guillet, who went well above and beyond his duties as advisor: he helped me many times when I was stuck, keeping an eye not only on the scientific result, but also on my personal growth as a researcher. Perhaps most importantly, he helped me face that which cannot be confronted with science: the French administrative system. Without him, my doctoral experience would have been very different.

My gratitude also goes to the MISTIC group that welcomed and sustained me, providing intellectual stimulation, emotional support, occasional entertainment and quality coffee. Likewise, I am indebted to the unofficial THEMIS group – Ant, Nathalie, Melanie – with which I worked, and whose intellectual and emotional support helped me transition from old student to (hopefully) young scientist. Another thank goes to Steve, asker extraordinaire of tough questions, who supported me at distance.

The help received during a Ph.D. is not exclusively scientific in nature, and does not come from scientists alone. For this reason I wish to extend my thanks to the lovely ladies of the administration, at the IAS and elsewhere, who had the patience to walk me through the mazes of bureaucracy when I came to them, having forgotten the procedure followed the previous time and the one before. I am grateful to all the friends who supported me and endured my venting outside of the laboratory. And, of course, my biggest debt of gratitude is to those who remained behind me and gave me the best and the most support, despite receiving only my mood swings in exchange: mamma e babbo.

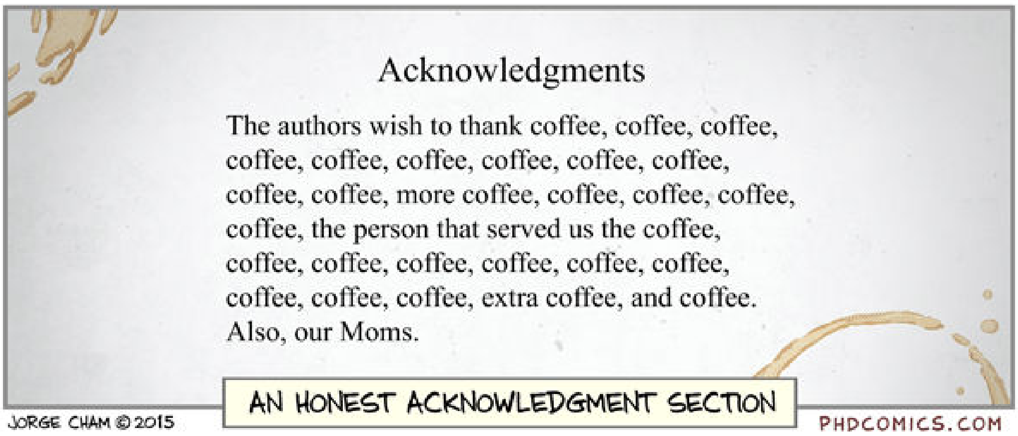

"Piled Higher and Deeper" by Jorge Cham, www.phdcomics.com

To devote the greater part of one's adult life to the lonely recording of the terrible emptiness between the stars is more than can be asked of someone entirely normal. It is perhaps with some realization of this that the Spatioanalytic Institute has adopted as its official slogan the somewhat wry statement, "We Analyze Nothing."

Isaac Asimov, *The Currents of Space*

Abstract

English

Interstellar dust is a key component of the interstellar medium (ISM). Not only does it play an important role in the physics and chemistry of the ISM, but its thermal emission can be used to trace the gas column density, and its polarization angle to trace the magnetic field orientation projected on the plane of the sky. Different dust models have been built to reproduce the main dust observables: extinction curve and albedo, spectral energy distribution (SED) from the near-infrared to the microwave continuum, polarization in extinction and emission, within cosmic elemental abundance constraints.

Our understanding of interstellar dust is, however, still incomplete; among other things, we do not fully understand the local variations in the emission and extinction properties of dust. The variation of the dust far infrared and submillimeter opacity from the diffuse ISM to molecular clouds is well established, and models have been proposed. With the *Planck* submillimeter survey we have, for the first time, a multi-wavelength, all-sky map of dust emission allowing for a precise measure of dust temperature, and therefore of dust opacity variations in the diffuse ISM. This thesis, based on the comparison of *Planck* data with extinction measures toward stars and QSOs, makes use of both dust models and data analysis to constrain the dust optical properties and evolution within the diffuse ISM, and to improve our understanding on the interplay between grain alignment and dust optical properties in the emission of polarized thermal radiation.

The first half of the thesis focuses on the total emission of dust in the diffuse ISM. The variations in the ratio of dust emission to extinction is used to constrain the variations of the dust optical properties. We fit the 20 SEDs normalized per unit extinction of *Planck* intermediate results XXIX with three dust models (Draine & Li 2007; Compiègne et al. 2011; Jones et al. 2013). The best agreement between model and observations is obtained for the model with the more emissive grains (Jones 2013), with optical properties derived from recent laboratory data on silicates and amorphous carbons. We develop a new estimator of the radiation field intensity G_0, which combines the dust SED and the extinction on the same line of sight. We show that this new estimator is less biased than the one obtained through the fitting of the dust SED. With their fixed optical properties, none of the models can simultaneously reproduce the variations of G_0 and of the shape of the SED. With our new estimator of G_0, we demonstrate that the variations in the dust optical properties and in the radiation field intensity give similar contributions to the scatter observed in the dust SED per unit extinction in the diffuse ISM.

The second half of the thesis focuses on polarized dust extinction and emission in molecular clouds. By confronting *Planck* and stellar observations to a dust model, we attempt to disentangle the effects of variations in the dust optical properties from the effects of variations in the grain alignment. We find a correlation between the ratio of polarized emission to polarized extinction, $R_{\mathrm{P/p}} = P_{353}/p_{\mathrm{V}}$, and the wavelength of maximum polarization in extinction, λ_{max}, which traces the typical size of the aligned grains. Using a new dust model for polarization based on *Planck* data, we show that the variation of the minimal size of aligned grains can reproduce the observed correlation, without any need for a change in the size distribution or in the optical properties of

grains. This scenario is also compatible with the drop of the fractions of polarization with $\lambda_{\max}$. Alternative models cannot however be ruled out.

Français

Les poussières interstellaires sont une composante clé du milieu interstellaire (MIS). Elles jouent non seulement un rôle important dans la physique et la chimie du MIS, mais elles servent également de traceur, du gaz via leur émission thermique, et du champ magnétique interstellaire via la polarisation de cette émission. De nombreux modèles de poussières reproduisent les principales observables sur les poussières (la courbe d'extinction, la distribution spectrale d'énergie (SED), la polarisation en extinction et en émission), tout en respectant les abundance cosmiques élémentaires.

Notre compréhension des poussières reste cependant toujours incomplète, en particulier sur l'origine physique des variations de l'extinction et de l'émission des poussières dans le MIS. Le changement d'opacité des poussières entre le milieu diffus et les nuages moléculaires est bien établi, et des modèles physiques d'interprétation ont été proposés. Avec ses cartes de l'émission submillimétrique de tout le ciel à plusieurs longueurs d'onde, le survey submillimétrique de *Planck* nous permet pour la première fois de mesurer la température des poussières, et d'étudier ainsi les variations d'opacité des poussières dans le milieu diffus. Cette thèse, basée sur une comparaison des données *Planck* avec des mesures en extinction en direction d'étoiles et de quasars, combine modélisation et analyse de données, afin de contraindre les variations des propriétés optiques des poussières dans le MIS diffus, et d'estimer les contributions respectives de l'alignement et de l'évolution des poussières à leur émission polarisée.

La première partie de la thèse se focalise sur l'émission non polarisée des poussières dans le MIS diffus. L'étude des variations de l'émission par unité d'extinction permet de contraindre les variations des propriétées optiques des poussières. Nous fittons les 20 SEDs normalisées en extinction de *Planck* Intermediate Results XXIX à l'aide de trois modèles de poussière (Draine & Li 2007; Compiègne et al. 2011; Jones et al. 2013). Le meilleur accord entre modèle et observations est obtenu pour le modèle utilisant les grains plus émissifs (Jones 2013), dont les propriétés optiques sont basées sur des données de laboratoires portant sur les silicates et carbones amorphes. En combinant la mesure de l'extinction et de la SED sur la même ligne de visée, nous obtenons un nouvel estimateur de l'intensité du rayonnement interstellaire G_0, qui s'avère moins biaisé que celui obtenu par un fit de la SED. Aucun des modèles n'arrive à reproduire simultanément les variations de G_0 et de la SED à propriétés optiques des poussières fixes. À l'aide de notre estimateur, nous démontrons que la variation des propriétées optiques et de l'intensité du rayonnement interstellaire ont des contributions semblables aux variations observées des SED dans le MIS diffus.

La seconde partie de la thèse se focalise sur l'extinction et l'émission polarisées dans les nuages moléculaires. En confrontant des données *Planck* et des observations stellaires à un modèle de poussières, nous tentons de séparer les effets dûs aux variations de l'alignement des poussières des effets dûs aux variations de leurs propriétés optiques. Nous trouvons une corrélation entre le rapport de la polarisation en émission à la polarisation en extinction, $R_{\mathrm{P/p}} = P_{353}/p_{\mathrm{V}}$, et la longueur d'onde de polarisation maximale en extinction, $\lambda_{\max}$, qui trace la taille typique des grains alignés. A l'aide d'un nouveau modèle de poussières basé sur les données *Planck*, nous démontrons que la variation de la taille minimale des grains alignés suffit à elle seule à reproduire la corrélation observée, sans avoir à modifier ni la distribution en taille ni les propriétés optiques des poussières, et qu'elle est de plus compatible avec la chute observée des fractions de polarisation avec $\lambda_{\max}$. D'autres interprétations ne sont cependant pas exclues.

Contents

Preface

The space between stars in the Galaxy, which appears empty at first glance, is actually permeated by a tenuous medium composed of gas, dust grains, relativistic particles (cosmic rays), magnetic fields and interstellar radiation, all interacting to create a structured and evolving environment: this is called **interstellar medium** or ISM. Despite constituting only about 10% of the galactic mass (Ferrière 2001), the ISM is of central importance in the evolution of the galaxy: the cleanest example of this is how stars are formed when gas filaments in the ISM undergo gravitational collapse, and how the elemental abundances in the ISM determine the chemical composition of the newborn stars; conversely, stars influence both the chemical composition and the structure of the interstellar medium by ejecting energy and matter (through stellar winds and supernova explosions) that has been processed in their interiors through thermonuclear reactions. Furthermore, it is the distribution of the ISM in the Galaxy and the way it is structured that determines where new stars are going to be born. In short, far from being a passive container for stars, the ISM is central in the evolution of the Galactic environment, and its study is indispensable for our comprehension of the Galaxy (see *e.g.* Draine 2011; Ferrière 2001).

Interstellar dust constitutes about 1% of the ISM in mass: once again the small number is misleading, because dust is an extremely important component of the interstellar medium. It is on the surface of dust grains that H_2 molecules are formed; dust is the component that extinguishes UV radiation in the interior of dark clouds, allowing chemical reactions to produce organic molecules that would otherwise be photolized; grain-gas collisions and the emission of photoelectrons from dust are the main source of gas heating in the diffuse ISM. Dust is important not only in itself, but also because it serves as a tracer of other components of the ISM. For instance, since atomic hydrogen is mixed with dust, dust thermal emission at infrared (FIR) and submillimetric (submm) wavelengths is used as a tracer for cool molecular hydrogen (H_2) in the Galaxy, which is hard to observe directly, as a way to measure galaxies mass. As another example, non-spherical dust grains align their short axes on magnetic field lines and polarize starlight, so that dust observation in polarization can be used to trace the direction of magnetic fields.

Our knowledge of the ISM in general and interstellar dust in particular, however, is still imperfect. Many questions, often interconnected, remain unanswered: how does the magnetic field influence matter? How does it interact with gravity and turbulence to regulate star formation? Where does dust come from, and how does it evolve over time? Our understanding of these issues is going to improve in the light of latest-generations surveys, such as *Planck*, which provide data of unprecedented quality and sky coverage. These data are already changing our way of understanding dust and the ISM. The present thesis inserts itself in this panorama, showing how the comparison between new data and models brings new light on the subject of dust properties and their evolution.

The thesis is articulated as follows: Chapter 1 is a general introduction to the subject of interstellar dust and the related topics that help putting it in context. A section on the interaction between matter and radiation introduces the concepts which will be used in the subsequent chapters; the current knowledge on the ISM and interstellar dust is reviewed and we introduce the dust models that are used or adapted in the rest of the thesis.

Chapter 2 focuses on a candidate dust component: hydrogenated amorphous carbon, and the evolution of its optical properties in the ISM under the effect of UV radiation. Two different dust models containing this material are considered, and their UV-driven evolution is estimated and compared to *Planck* observations.

Chapter 3 focuses on the 20 $A_{\rm V}$-normalized SEDs presented in Planck Collaboration Int. XXIX (2014) which represent the Galactic dust SED in the diffuse ISM at different temperatures. Fits with both a modified black body and physical models show that these SEDs cannot be reproduced by dust with fixed optical properties: variations in the refractive index of dust materials – presumably driven by processes of dust evolution – play a role comparable with the variations of interstellar radiation field. We give the first estimate of the variations in optical properties in the diffuse ISM.

Chapter 4 presents the work done so far in the comparison of polarized dust emission and extinction in translucent and dark clouds, using both *Planck* and stellar data. Employing polarization ratios such as $R_{\rm P/p} = P_{\rm sub}/p_{\rm V}$ helps disentangle the effects of magnetic field orientation, dust alignment and dust optical properties. Observations are shown to be consistent with a dust model where the only factor in polarization efficiency is the grain alignment function.

Since the work presented in this thesis is part of larger *Planck* effort to understand interstellar dust, it builds upon and expands results by other authors. For this reason, Chapters 2, 3 and 4 all begin with the description of a *Planck* paper that informed or inspired my work in that chapter, and which is necessary to understand the implications of my results.

Part I

Toward a major update of dust models

Chapter 1

Introduction

Contents

Phase	Material	Volume	Mass	Density (cm^{-3})	T (K)
HIM	H II	$\sim 50\%$	$\sim 0.1\%$	~ 0.005	$\sim 10^{5-6}$
WIM	H II	$\sim 10\%$	3 - 10%	0.2 - 0.5	$\sim 10^4$
WNM	H I	$\sim 40\%$	20 - 25%	~ 0.6	~ 5000
CNM	H I, H_2	$\sim 2\%$	$\sim 70\%$	$\gtrsim 30$	$10 - 100$

Table 1.1. ISM phases, adapted from Draine (2011) and Ferrière (2001).

1.1 The interstellar medium

1.1.1 ISM phases

The ISM is a very dynamic, structured and heterogeneous environment. It is common to subdivide it into *phases* which are in approximate pressure equilibrium and differ from each other in temperature, density and state of the main gas component (hydrogen): ionized, neutral and atomic, neutral and molecular. This division was pioneered by McKee & Ostriker (1977) and has repeatedly been sustained by both observations and simulations (*e.g.*, Ferrière 2001; Hennebelle & Iffrig 2014). It should be born in mind that this division does not describe a static environment in strict equilibrium: phases interact with and transform into each other (see Sect. 1.1.4).

HIM

The Hot Ionized Medium, or HIM, is a gas that has been heated by supernova shocks to a very high temperature (T $\sim 10^5 - 10^6$ K) and that is collisionally ionized. It mainly emits in the soft X-rays and in the radio (due to brehmsstrahlung, *i.e.* free-free emission from high-energy electrons); it can be observed in absorption in the lines of highly ionized species such as O VI and N V (See the review by Spitzer 1990 and refs. therein). It makes up a large volume fraction – perhaps half – of the Galactic ISM, and it is thought to extend well above and below the Galactic disk (Draine 2011); however, due to its extremely low density, it contributes a very small fraction ($\sim 0.1\%$) of the overall ISM mass. It is also called **coronal gas** due to its similarity to the gas in the Sun's corona (Draine 2011).

WIM

The Warm ionized Medium is an ionized gas, with a temperature of the order of 10 000 K (Haffner et al. 1999). Its source of ionization is hypothized to be the UV radiation from hot massive stars, especially recently-formed O stars (Domgorgen & Mathis 1994). This gas is observed mainly in the recombination lines of hydrogen, especially the H_α (656.3 nm) and the other Balmer lines. A different source of information on the WIM are the radio pulses of pulsars, where radio waves of different frequency are delayed by an amount proportional to the distance traversed and the electron density of the intervening ISM. A measure of this dispersion allows to reconstruct the distribution of interstellar electrons or vice versa (Cordes & Lazio 2003; Draine 2011), and since the WIM is much denser than the HIM – it comprises $\sim$ 10% of the volume and a similar, or slightly inferior, fraction of the mass (Draine 2011; Ferrière 2001) – tracing the electron density is equivalent to tracing the WIM.

UV-ionized hydrogen is also typical of the so-called **H II regions**, areas that surround hot stars in dense clouds. Their gas is similar, in temperature and ionization state, to the diffuse WIM, although it is denser and concentrated in localized regions instead of filling the space between denser clouds. Sometimes, to emphasize both the difference and the similarities between these two media, the WIM is called **diffuse H II gas**.

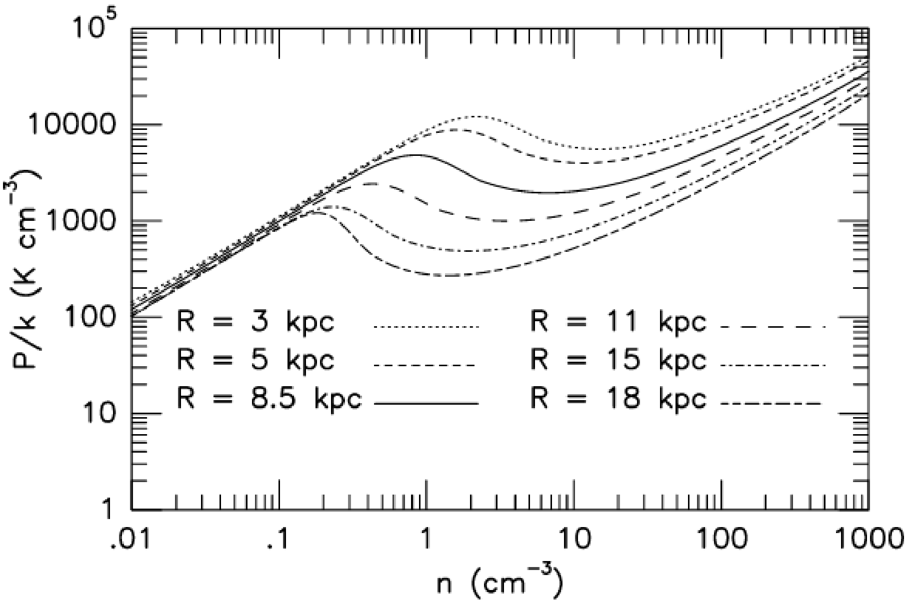

Fig. 1.1. The phase diagram of atomic ISM, showing thermal pressure P/k as a function of the numeric density of H atoms n. For those pressures at which more than one density is possible, two atomic phases of the ISM – WNM and CNM – coexist. The different curves are calculated at different Galactocentric distances (the Sun being at 8.5 Kpc) with different intensities of the heating processes (cosmic rays, UV-driven emission of electrons from dust). From Wolfire et al. (2003).

WNM

The Warm Neutral Medium is a phase with a relatively high temperature of $\sim 5\,000$ K, but composed of neutral atomic hydrogen. It is mainly heated by dust photoelectron emission and by cosmic rays; it cools by fine structure line emission – from species such as CII and OI – and Ly$_\alpha$ emission. (Wolfire et al. 1995, 2003). It is mainly seen in emission in the HI 21 cm line, since at high temperature the stimulated emission dominates on absorption (Ferrière 2001 and refs. therein). Its lines are characteristically wide due to thermal Doppler broadening. It is one of two thermally stable states for the neutral gas, the other being CNM. It constitutes about 40% of the ISM volume and 25% of the ISM mass (Draine 2011). For certain pressure ranges, the WNM can coexist with a colder phase: the CNM (Wolfire et al. 1995, 2003, see Fig. 1.1).

CNM

The Cool Neutral Medium is a neutral phase with a temperature of the order of $\sim 10 - 100$ K. Mainly heated by cosmic rays and photoelectron from dust like the WNM, but cooled by the efficient 158-μm CII emission line. It is much denser than the other phases, thanks to its low temperature ($n_H \sim 10 - 10^2$ cm^{-3} in the atomic phase, even higher in the molecular one – see later) and concentrates over 70% of the ISM's mass in only 1-2% of the volume (Draine 2011). Most of the CNM (in volume) is composed of atomic hydrogen, since the H_2 molecules are rapidly dissociated by the radiation present in a narrow range of UV wavelengths. The atomic CNM can be observed in extinction and in emission at 21 cm, with lines that are much narrower than the WNM 21 cm emission due to the smaller thermal Doppler widening. Some parts of the CNM are dense enough that the absorption band at the wavelength of H_2 dissociation becomes optically thick. H_2 molecules are then shielded from radiation by other H_2 molecules. This is called *self-shielding*, and where it takes place molecular hydrogen can form in quantity and form the so-called **molecular clouds**. The classification of molecular clouds involves several factors including their density, composition and size (*e.g.* van Dishoeck et al. 1993; Planck Collaboration XI 2014 and the division in LVC, IVC and HVC), but for our purposes we can adopt a simplified classification based on their column density – or alternatively, since gas is accompanied by dust, on the extinction A of stars behind them. We can use for this purpose the extinction on the flux through the cloud, integrated over the V photometric filter ($\sim$ 550 nm): $A_{\rm V}$, measured in magnitudes (see Sect. 1.3.1). With this definition, we may distinguish between *translucent clouds* ($1 \lesssim A_{\rm V} \lesssim 3$) and *dark clouds* ($A_{\rm V} \gtrsim 5$).

Translucent clouds are composed of both atomic and molecular hydrogen. Their $A_{\rm V}$ of order unity means that their extinction is sufficiently low for UV radiation to penetrate them, influencing their heating and chemistry. These low $A_{\rm V}$s also imply column densities of $10^{20} - 10^{21}$ cm^{-2} (see the extinction curve in Sect. 1.3.1); this, combined with a typical translucent cloud size of 0.1-1 pc (in the neighborhood of 10^{18} cm), means that their number densities n_H range from a few 10^2 to a few 10^3 cm^{-3}.

Dark clouds are very different: they are dense ($n_H \geq 10^3 - 10^4$ cm^{-3}), their mechanical equilibrium is determined by self-gravitation, and their central regions are opaque to UV and optical radiation. This last feature is central to their chemistry: for instance, dust grains are covered by H_2O and other ices, and cosmic rays are the main source of heating because only IR light (from stars or dust) now penetrates so deeply. The thermal speed at the typical temperatures of dark clouds ($T = 10 - 20$ K, for which $\sqrt{3kT/m_{H_2}} = 0.35 - 0.5$ km/s) is smaller than the observed velocity dispersions (e.g. ~ 1 km/s in Solomon et al. (1987)), so there must be an important contribution from internal turbulent motions and shocks. These are the clouds where stars are typically formed.

The H_2 gas is very hard to observe directly, since the ground state of the H_2 molecule has no dipole moment: having no electric dipole transitions, but only quadrupole transitions, much less probable, it cannot be observed in emission. Molecular clouds, therefore, are mapped not by directly observing H_2, but by proxies. The most important of these is CO, the emission lines of which – most notably the one at $\lambda = 2.6$ mm – are used to trace H_2 mass. The ^{12}CO 2.6 mm line, however, is often optically thick and therefore it mostly traces the envelopes of clouds[1]. One option for tracing cloud cores is to measure ^{13}CO, which has a much lower optical depth[2]. But since the self-shielding for CO and H_2 is different, the two molecules do not trace exactly the same medium. There exists an intermediate regime with almost no HI and no CO yet, but only (invisible) H_2. This is called the “dark gas” (Reach et al. 1994; Grenier et al. 2005; Planck Collaboration Early XIX 2011).

Another important tracer of CNM is the far infrared and submillimeter dust emission, since the dust-to-gas ratio seems to be rather constant across the galaxy, though not among galaxies (*e.g.* Bohlin et al. 1978). It has the advantage of tracing both the atomic and the molecular gas, including dark gas, on one hand; and that the ISM is transparent at far infrared and submillimeter wavelengths, so all the dust on a line of sight is detected, on the other. A disadvantage, however, is that the temperature and optical properties of the dust are not uniform, and an uncertainty is introduced whenever this is not taken into account. The non-uniformity of dust properties is expanded upon in Sect. 1.3.4 and constitutes the main topic of Ch. 3. For dense clouds a proper treatment of radiation transfer is also necessary (*e.g.* Ysard et al. 2012). Finally, interstellar dust is not only present in the CNM: while this contains most of the Galactic gas – and therefore most of the dust – the WNM and WIM give non-negligible contributions to the dust emission.

[1] Despite the fact that ^{12}CO traces only shows the outer layer of clouds it can be shown, using some empirically-derived relation between dark cloud observables and under some assumptions on the virialization of clouds, that a roughly linear relation exists between the ^{12}CO brightness of a molecular cloud and its mass (see *e.g.* Bolatto et al. 2013).

[2] This is because ^{13}C is much less abundant than ^{12}C: Wilson & Rood (1994) obtained a ^{12}C/^{13}C abundance ratio of 76 ± 7, although the ratio can vary depending on the zone (*e.g.* Stahl et al. 2008)

Wavelength range [μm]	Power density [W m^{-3}]
0-0.0912	0
0.0912-0.11	$38.57 \cdot (\lambda/1\,\mu m)^{3.4172}$
0.11-0.134	$2.045 \cdot 10^{-2}$
0.134-0.246	$7.115 \cdot 10^{-4} \cdot (\lambda/1\,\mu m)^{-1.6678}$

Table 1.2. The functional form for the radiation field at $\lambda < 0.246\,\mu$m in the Solar neighborhood, presented in Mezger et al. (1982) and used in Mathis et al. (1983).

1.1.2 The interstellar radiation field (ISRF)

The interstellar dust interacts with radiation, and since the absorption and emission by dust depend on the wavelength, it is important to know the spectrum of the radiation in which dust is immersed. We can expect the radiation field to depend on the surroundings – such as whether a star or another source of radiation is close or a nearby dark cloud covers part of the sky. It is a common simplification, however, to consider dust as being heated by an *average* radiation field emitted the stars and ISM throughout the galaxy. This average field is what is called the *InterStellar Radiation Field*, or ISRF. Modeling the ISRF is a task that has been undertaken for a long time: see *e.g.* Habing (1968); Mezger et al. (1982); Mathis et al. (1983). Mezger (1990) contains a historical overview on the subject.

One of the most widely used ISRF models, and the one we use in this thesis, is the ISRF for the solar neighborhood as calculated by Mathis et al. (1983), which is dominated by starlight between 912 Å and 8 μm and by dust emission between 8 μm and 1 mm. The UV component of the spectrum between 912 and 2460 Å is modeled as a combination of power laws and constant values (tab. 1.2); these reproduce a smoothed-out version of the Gondhalekar et al. (1980) spectrum, which was based on UV observations integrated by modeling. Between 2460 Å and 8 μm the spectrum is a sum of three blackbodies at different temperatures, meant to modelize different stellar components: Galactic disk stars at 7500 and 4000 K and red giants at 3000 K. Between 8 μm and 1 mm the spectrum is based on the observed dust emission in the region at $l \sim 30°$, $b \sim 0°$, integrated over the whole sky and weighted on model of dust abundance as a function of distance from the Galactic center. The model does not include the long-wavelength components that dominate longward of 1 mm, such as the Cosmic Microwave background (CMB), the synchrotron emission from electrons accelerated by the Galactic magnetic fields and the free-free emission from electrons in the WIM (see *e.g.* Spitzer 1998 and refs. therein). This has a negligible effect on dust models, since dust is transparent at long wavelengths.

The ISRF thus calculated is an average value for the diffuse ISM in the Solar neighborhood[3]. Inside translucent and molecular clouds, because of extinction, the intensity of radiation will generally be less (unless there is a nearby source like a star). Extinction will depend on the wavelength, so a solution of the radiation transfer equation is needed to know the radiation field inside the cloud. Regions in the vicinity of stars and star aggregations obviously have a much more intense radiation field, dominated by the star's or aggregation's spectrum. Dust models for the diffuse ISM, however, are concerned with zones far from any particular star association and where the extinction is low. In such regions, the error made in employing a simplified extinction model is not greater than the uncertainties of a complex radiation transfer model. An approximation often used for modeling the diffuse ISM is that the ISRF has a fixed shape of the spectrum, and only the intensity changes. This is implemented in dust models by introducing a dimensionless intensity parameter corresponding to the ratio between the ISRF intensity in our model and the average Galactic ISRF. We choose

[3]The ISRF tends to be more intense close to the Galactic center. Mathis et al. (1983) showed ISRF models for various Galactocentric distances: unless otherwise noted, when we mention "the Mathis et al. (1983) ISRF" we intend the model for the Solar neighborhood, *i.e.* at the Galactocentric distance of the Sun.

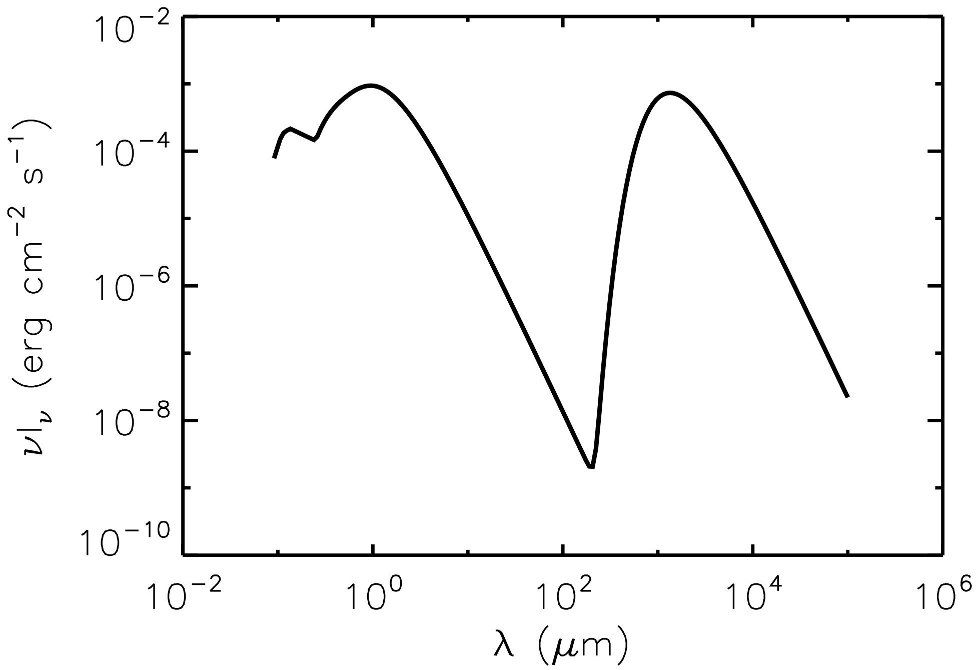

Fig. 1.2. An example of ISRF model. This is the default spectrum used within the DustEM tool (Sect. 1.3.3), consisting of the star components from Mathis et al. (1983) and the CMB black body. The model neglects mid-IR emission from dust (Sect. 1.3), but since dust absorption is very low at those wavelengths, the effect on dust heating is minimal.

to follow the DustEM convention (Sect. 1.3.3) and call the intensity parameter G_0. By definition, $G_0 = 1$ where the ISRF equals its average Solar Neighborhood value as given in Mathis et al. (1983). Darker zones have $G_0 < 1$ while brighter zones have $G_0 > 1$.

1.1.3 The Galactic magnetic field

The interstellar space in the Galaxy is permeated by a magnetic field with an average intensity of a few to a few tens μG (by comparison, the dipole magnetic field of Earth has an intensity of ~ 0.3 G at the equator). This field was first discovered when Hall (1949) and Hiltner (1949a,b) found that over all the sky reddened stars – *i.e.* stars whose light has been extinguished by the interstellar medium – show a linear polarization of a few percent, which was attributed to elongated interstellar dust particles aligned by the Galactic magnetic field. Following decades of observations, we now have a full-sky map of the interstellar magnetic field (*e.g.* Heiles 2000; Planck Collaboration Int. XIX 2015); we also know that the magnetic field is constituted of a regular component roughly parallel to the Galactic plane (deviations are of the order of 10°, see Ferrière (2001)) plus a turbulent component on a smaller scale.

The magnetic field has a great importance in Galactic evolution, shaping and structuring the ISM at all scales: the vertical distribution of matter in the Galactic disc can be explained if magnetic pressure adds itself to thermal and turbulent pressure to counterbalance gravitational attraction (Boulares & Cox 1990); the magnetic field is necessary to explain the dynamics of molecular clouds (see Sect. 1.1.1 and Planck Collaboration Int. XXXV 2015) and it regulates star formation, mainly by slowing down gravitational collapse (Federrath & Klessen 2012).

There are several different methods to trace the magnetic field, each giving information on a different aspect of the field (Hildebrand 1988).

Dust extinction and emission: Non-spherical interstellar dust grains tend to align with their shorter axis parallel to the magnetic field: since the overall dust extinction is more efficient for the polarization parallel to the long axes, starlight acquires a polarization that traces the field direction (see Sect. 1.3.2 and Ch. 4). Thermal dust emission is also more efficient for the polarization parallel to the long axes, making it another polarized tracer of magnetic field lines. The main limitations of dust polarization as a tracer of the magnetic field are that it only traces the field component perpendicular to the line of sight (*i.e.* parallel to the plane of the sky), $\mathbf{B}_\perp$, and that it does not give a direct measure of the field intensity. The latter limitation can be overcome with a statistical study: Chandrasekhar & Fermi (1953) showed that, assuming field lines are perturbed by turbulence in the ISM, field strength determines the amplitude of distortions, with stronger fields resulting in straighter field lines and more uniform polarization angles over the sky. The typical dispersion in polarization angles (10°) corresponds to a $\sim 7\,\mu$G Galactic field.

Zeeman splitting: For certain atomic and molecular lines, an external magnetic field can subdivide certain electronic energy levels, causing a splitting of the line that is proportional to the field intensity. The splitting is usually very small: for the HI 21-cm line – one of the most commonly used in Zeeman observations – it is much narrower than the line itself, and cannot be observed directly. There is a way around this: for a field parallel to the line of sight, the two split lines are circularly polarized and have opposite handedness (Sect. 1.3.2), so the observed line has a recognizable polarization profile and a total circular polarization $\propto \mathbf{B}_\parallel$.[4] Field strengths obtained this way are also of the order of a few μG, although they give lower values than Chandrasekhar-Fermi due to systematic effects. Other emission lines of interest for Zeeman measurements are OH masers (Heiles & Robishaw 2009).

Synchrotron emission: In regions with a large abundance of free, high-energy electrons, free-free radiation is emitted by the electrons spiralling around magnetic field lines. This radiation is strongly polarized in the direction orthogonal to the magnetic field that accelerates the electrons: it traces the magnetic field on the plane of the sky $\mathbf{B}_\perp$, but the polarization angle on the sky is orthogonal to that of dust extinction. Its intensity depends on both the magnetic field strength and the electron abundance spectrum, so we need an estimate of the latter to estimate the field intensity (Ferrière 2001).

Faraday rotation: When an electromagnetic wave travels through free electrons, its plane of linear polarization rotates as the wave propagates. The angle of rotation is equal to $\lambda^2 \cdot$ RM, where RM is the rotation measure: $RM = \int_0^L n_e\, \mathbf{B}_\parallel\, dL$. Given an estimate of the electron density a measure of $\mathbf{B}_\parallel$ can be obtained. Since it increases with λ this effect is mainly observed in the radio. Pulsars are usually employed as the background sources for the radiation (*e.g.* Han & Qiao 1994).

1.1.4 The interstellar matter lifecycle

The ISM is a dynamic environment, where magnetic field, stars and all the previously described phases of the ISM interplay, evolve and influence each other. This section intends to convey a general idea of how the ISM evolves over time and of the processes that enter it.

One of the most important concepts in this topic is that the ISM undergoes a "life cycle" that involves star formation. The diffuse ISM condenses to form molecular clouds, inside the

[4] The Zeeman splitting also induces a linear polarization proportional to $\propto \mathbf{B}_\perp$, but since this is a second order effect, it is usually too weak to detect (Heiles & Robishaw 2009)

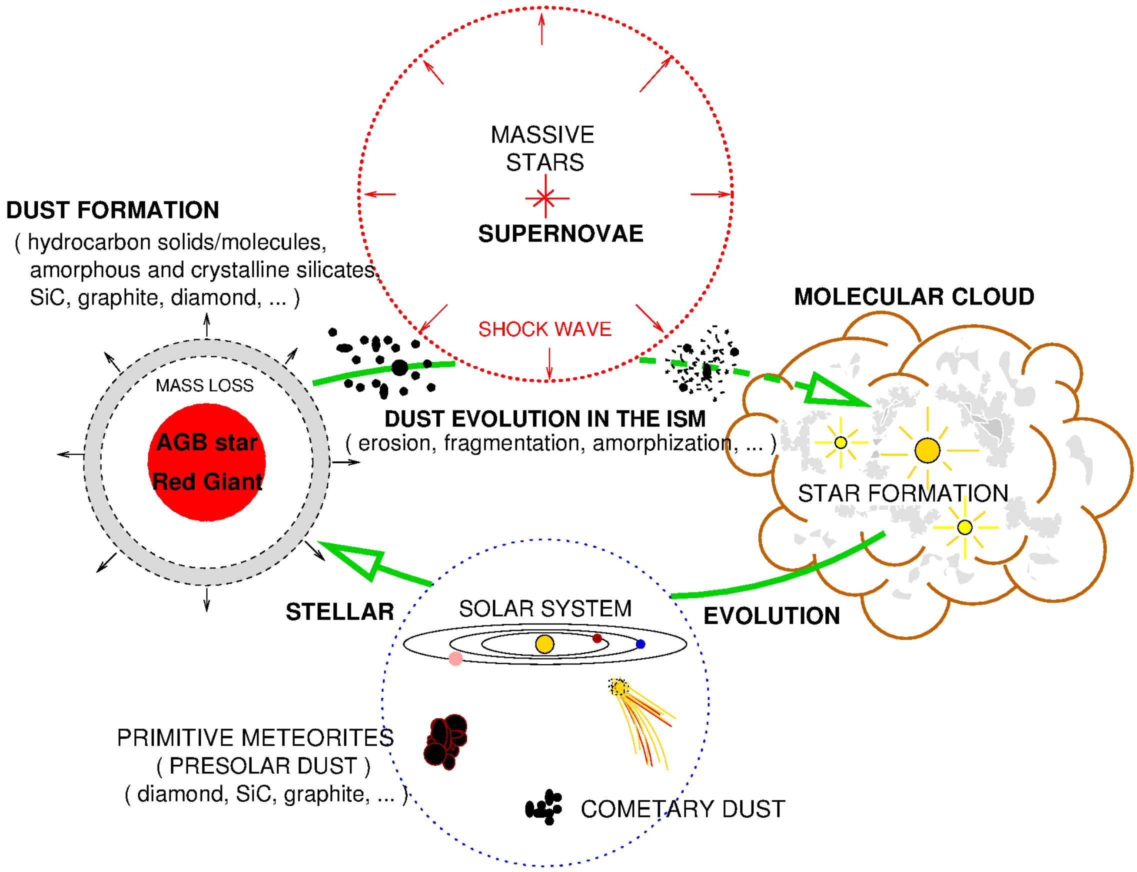

Fig. 1.3. Schematic representation of the life cycle of interstellar dust. Formation in the atmospheres of red giants and AGBs (but possible also elsewhere – see text), evolution influences by supernova shocks and residence in dense molecular clouds. Cometary dust and presolar meteorites can contain grains of interstellar dust, and their analysis can give us precious insights on it. From Jones (2004)

densest clouds gravitational collapse forms stars, stars process matter in their interiors through thermonuclear reactions, matter from stars is finally returned to the ISM through stellar winds and supernova explosions. In the process the ISM evolves chemically, being continually enriched in helium and metals.

In addition to this cyclical process, there are continuous interactions between components of the ISM. Shocks from supernova explosions form shells of compressed interstellar gas, which then cool, fragment and may form molecular clouds where new stars are formed. On the other hand, newly formed stars emit high-velocity winds that inject energy and momentum in the surrounding dense cloud material. This could hold dense clouds against gravitational collapse, preventing the formation of new stars. In the case of massive stars (O and B), that are often grouped in associations, this injection could be powerful enough to disrupt the parent molecular cloud and return it to the state of diffuse ISM. Ionizing stellar radiation also controls the WIM (see Ferrière 2001 and refs. therein).

In the complex evolution of Galactic environment, dust also forms and evolves influenced by the surrounding ISM. Dust formation is not yet completely understood: according to classic theories, dust would form in the outer atmospheres of AGB stars, where the conditions are conductive to the formation of solid materials (such as silicates or carbonaceous materials). Stellar winds would then expel them in the outer ISM. However, the ISM is periodically swept by supernova shocks that should destroy grains much faster than stars can supply them (*e.g.* Jones et al. 1994; Bocchio et al. 2014), so at least part of the dust should form directly on the ISM (Draine 2006).

A dust grain's lifetime, before supernova shocks destroy it, has been estimated at $4 \cdot 10^8$ years (McKee 1989; Jones & Nuth 2011). In this period of time, it will cycle in and out of molecular clouds. The diffuse ISM condenses into dense clouds and, after star formation, dense clouds are dissipated by the newly formed stars. The time scale for this cycle, although no precise value can be known, has been estimated to be of the order of 10^7 years[5] , so a dust grain should undergo it several times during its lifetime. In the meanwhile, dust will evolve due to several processes: photoprocessing of materials, accretion of gas on the grains, partial destruction by supernova shocks, formation of aggregates of grains.

1.2 Radiation-matter interaction

Most of our information on interstellar dust comes from radiation in one form or the other: the dust absorption spectrum, the scattered starlight, the emission SED, over a wavelength range that goes from the γ rays all the way up to microwaves. To extract information about dust from the observed electromagnetic radiation, therefore, we need to understand how the radiation interacts with small particles of matter. In this chapter we introduce the optics of absorption, scattering and emission of radiation on the part of small particles, to apply to the observations of dust in the following chapters. We follow mainly Draine (2011), Whittet (2003), Kruegel (2003) and the references therein.

1.2.1 The optical properties of matter

Cross-sections: extinction, absorption and scattering

A beam of irradiance (or intensity) I passing through a cloud of absorbing and/or scattering grains will lose energy. In the simplified case where all grains are identical and they are uniformly distributed in space, the extinction of the beam can be written as following:

$$dI = -I\, C_{\rm ext}\, n\, dL \tag{1.1}$$

where n is the number density of grains, $C_{\rm ext}$ is the extinction cross-section of a single grain, and L is the length travelled in the cloud. Since we can expect this cross-section to be proportional to the collection area, one often uses the extinction efficiency $Q_{\rm ext} = C_{\rm ext}/\pi\, a^2$, where a is the grain radius (if spherical) or the radius of a sphere of equivalent volume (if not spherical). The extinction is the sum of absorption and scattering, so that we have

$$\begin{aligned} C_{\rm ext} &= C_{\rm abs} + C_{\rm sca} \\ Q_{\rm ext} &= Q_{\rm abs} + Q_{\rm sca} \end{aligned} \tag{1.2}$$

Integrated over distance, Eq. 1.1 gives Beer's law:

$$I = I_0\, e^{-\tau} \tag{1.3}$$

where the quantity $\tau = n\, C_{\rm ext}\, L$ is an adimensional quantity called *optical depth*. Since the extinction is generally measured in magnitudes, $A_\lambda = -2.5\, log(I/I_0)$, the relation between extinction and optical depth is $A_\lambda = 1.086\, \tau$.

[5] McKee (1989) took $3 \cdot 10^7$ years as an estimate of the time necessary for radiation from massive stars to ionize cold clouds. He then argued that, since WIM only constitutes about 10% of the mass of ISM, the opposite process should be about ten times faster.

Aside from the grain composition, the parameters that control the efficiency factors Q_{abs}, Q_{sca} are the grain size a (radius of the sphere of equivalent volume) and the wavelength λ; in fact, the quantity of interest is the adimensional size factor $x = 2\pi a/\lambda$. The dependence of Q_{abs} and Q_{sca} on the material composing the grains is a question of that material's complex refractive index.

The refractive index

The **refractive index** of a material[6], $m = n + ik$, describes how the propagation of electromagnetic radiation changes inside that material. The quantities n and k are also called *optical constants*, although this name is improper since they depend on the wavelength. The real part of the refractive index n is related to the change in the speed of propagation in the wave and to scattering, while the imaginary part of the refractive index, k, is related to the absorption.

1.2.2 Optical theory for solids

Uniform spherical particles: the Mie and Debye theory

When one has the refractive index of a material, the dust efficiency factors Q_{abs} and Q_{sca} can be obtained by solving Maxwell's equations with the right boundary conditions on the grain's surface. This was first done by Mie (1908) and Debye (1909) for spheres, outside the context of interstellar dust. Since then, generalizations for non-spherical shapes – either exact or approximated – have been found; see van de Hulst (1957); Bohren & Huffman (1983) and Bohren & Huffman (1983) for a comprehensive discussion on scattering, Greenberg (1968) for a discussion focused on interstellar dust grains.

The behavior of Q_{abs} and Q_{sca} can be separated in different regimes depending on the value of the size factor $x = 2\pi a/\lambda$:

Geometrical optics regime: when $x \gg 1$ (or $\lambda \ll a$, wavelength much smaller than the grain size), the grain behaves as a “macroscopic” object. Absorption follows the geometrical cross-section: $C_{abs} = S$, where S is the geometric area. According to Babinet's principle (Kruegel 2003), in this regime the cross-section for scattering – if the grain is seen from sufficiently far away [7] – equals that for absorption (see *e.g.* van de Hulst 1957), so $C_{sca} = S$. The extinction cross-section is the sum of the absorption and scattering cross sections: $C_{ext} = C_{abs} + C_{sca} = 2S$. Since in this regime the extinction cross-section is independent of wavelength it is also called “grey extinction”. A grey extinction means that no information on grain size can be retrieved from the analysis of the dust extinction law at those wavelengths: for $x \gg 1$, extinction is independent of λ and grain size. In the particular case of spherical grains, where the geometrical cross-section is πa^2, we have $Q_{abs} = Q_{sca} = 1$ and $Q_{ext} = 2$.

Electrostatic or Rayleigh regime: This is usually described as the case where the wavelength is much larger than the grain size, $x \ll 1$, but most of the time, when the term “Rayleigh regime” is mentioned, one is actually referring to the case $|m|x \ll 1$, i.e. when the refracted wavelength is much larger than the grain size. In this regime one has (Bohren & Huffman 1983)

$$\begin{aligned} Q_{\mathrm{abs}} &= 4x \,\mathrm{Im}\left(\frac{m^2-1}{m^2+2}\right) \\ Q_{\mathrm{sca}} &= \frac{8}{3}x^4\left|\frac{m^2-1}{m^2+2}\right|^2 \end{aligned} \tag{1.4}$$

[6] The definition of refractive index can use either sign. Here we follow the convention of Bohren & Huffman (1983).

[7] From sufficiently far away that diffraction (i.e. the small-angle scattering around the borders of the grain) becomes important, or from sufficiently far away that the grain's shadow can no longer be distinguished.

In the case where $(m^2+1)/(m^2+2)$ is a slowly varying function of wavelength – which excludes, for instance, metallic particles – then $Q_{abs} \propto \lambda^{-1}$ and $Q_{sca} \propto \lambda^{-4}$. One consequence of this is that $Q_{sca} \ll Q_{abs}$, so extinction is essentially due to absorption only. Another important consequence is that, since $Q_{abs} \propto a$, the absorption coefficient is proportional to the volume of the grain, $C_{abs} \propto a^3$: for an ensemble of grains in the Rayleigh regime, absorption is proportional to their total volume, so we cannot constrain their size, only their total mass.

Ondulatory or Mie regime: The case $x \sim 1$ is the hardest to treat, although it can be solved numerically. In general it can be said that in this regime extinction has a very strong dependence on λ, led by scattering: Q_{ext} can be much higher than 2.

An example of Mie scattering can be seen in Fig. 1.4, from Kruegel (2003), where $Q_{\rm abs}$ and $Q_{\rm sca}$ are shown as a function of x for materials of different absorptivity. For computational simplicity, each curve is calculated at fixed optical properties even if the refractive index of real materials is wavelength dependent; for this reason it is preferable to regard the curves of Fig. 1.4 as the effects of variable particle size at fixed wavelength rather than the other way around.

Several features of the curve are apparent. As discussed above, for $x \to 0$ (Rayleigh regime) we see the extinction vanish, while for large x (geometrical optics) the extinction efficiency settles around 2, with equal contributes from absorption and scattering. The intermediate regime is characterized by large oscillations with superimposed smaller ripples, which are a result of interference in the refracted light inside the particle. The first peak, where extinction is maximum, occurs at about $8(n\text{-}1)$, which is around 4 for the refractive index shown in figure. Increasing the absorption coefficient damps both the large oscillations and the ripples, as light is absorbed inside the sphere and has less chance to interfere. At large enough absorption (not shown in figure) the oscillations all but vanish.

Composite grains: the effective medium theories

So far we have only seen the Mie theory applied to spherical and uniform grains, but it would be interesting to also treat grains composed of multiple substances: it is known, for instance, that dust grains in dense clouds accrete a coating of ices (see 1.3.4); at the same time, the study of GEMS ("Glass with Embedded Metals and Sulfides", see 1.3.1) suggests that interstellar silicates might contain iron inclusion.

The Mie theory allows an exact solution for core-mantle spherical particles, as first found by Aden & Kerker (1951): like in the case of the uniform sphere, the basic idea is to solve Maxwell's equations with the right boundary conditions, except that the boundaries now include the interface between the core and the mantle of the particle as well as the interface between the mantle and the exterior. The method can be generalized to an arbitrary number of coatings.

Regarding the case of inclusions, it is possible to treat a mix of different media – each with its complex refractive index m – as if it was a single medium with an effective refractive index m_{eff}, which can be subjected to treatment according to Mie theory. Effective medium theories can also be used to model porous grains: it suffices to use vacuum as one of the materials, *i.e.* to set $n = 1$, $k = 0$ for it.

Let us assume, following Kruegel (2003), that a particle is composed of many homogeneous subparticles for which we use the subscript j: then each material occupies a volume fraction f_j of the grain ($\sum_j f_j = 1$) and the displacement field in each subparticle is $\epsilon_j \, \mathbf{E}_j = m_j^2 \, \mathbf{E}_j$. The effective refractive index is defined by $\sum_j m_j^2 \, f_j \, \mathbf{E}_j = m_{eff}^2 \sum_j f_j \, \mathbf{E}_j$. Also, if the subparticle is much smaller than the wavelength, it can be approximated as an inclusion in an extended medium, subjected to a spatially-uniform but time-variable field $\mathbf{E}'$. In this case there is a linear relation between the field in the inclusion and the field in the medium: $\mathbf{E}_j = \beta \, \mathbf{E}'$, where β can be calculated knowing

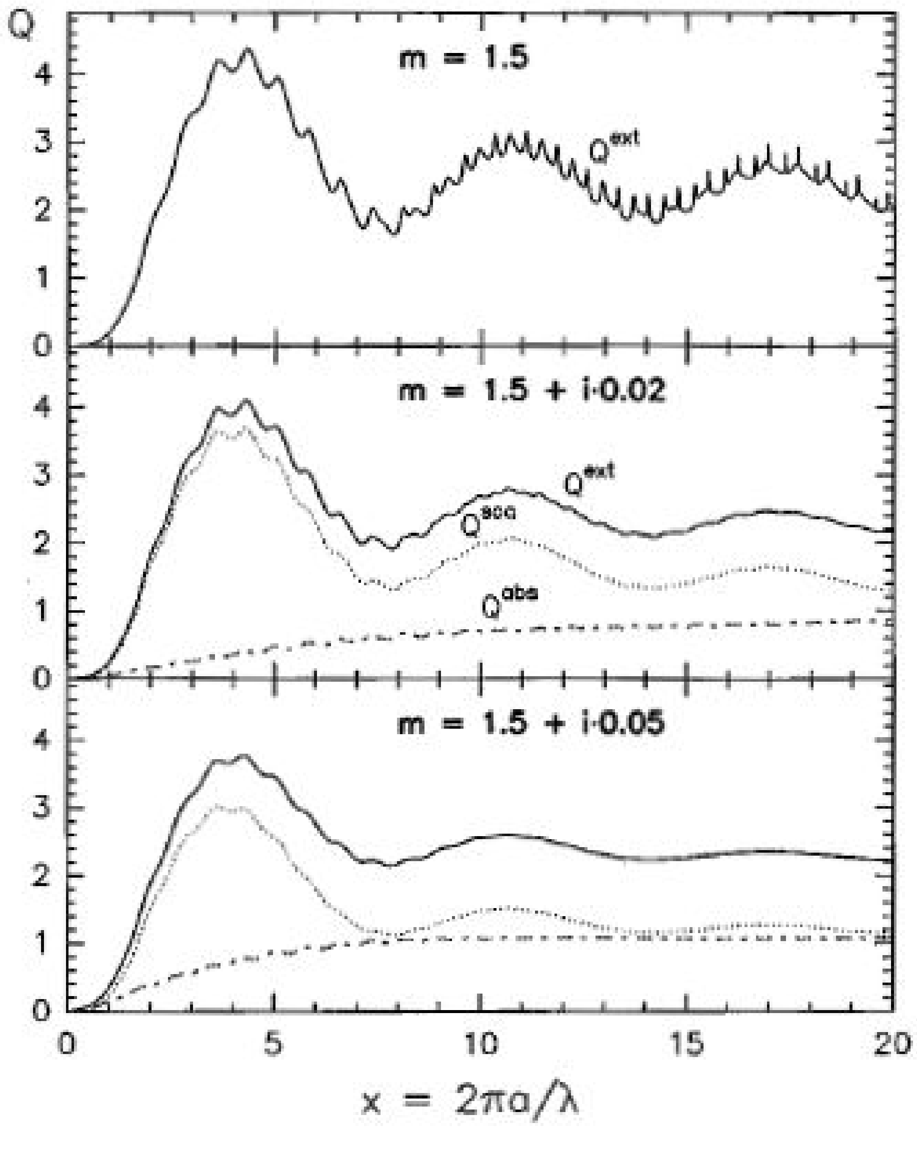

Fig. 1.4. $Q_{\rm ext}$ as a function of x for materials of different absorptivity. From Kruegel (2003).

the materials used and the shape of the inclusion[8]. Putting these two results together yields the Bruggemann rule

$$\sum (m_j^2 - m_{eff}^2)\, f_j\, \beta_j = 0 \tag{1.5}$$

Given the m_j of the various components and the values of the β_j, m_{eff}^2 can be determined from a complex polynomial of order N, where N is the number of materials.

Bruggeman's rule treats all materials in the same way. If the particle is composed of a matrix with embedded subparticles, we may want to treat the matrix as a special case. Calling m_m, f_m the parameters for the matrix and m_i, f_i those for the inclusions, we obtain the Garnett mixing rule:

$$m_{eff}^2 = \frac{f_m\, m_m^2 + \sum f_i\, \beta_i\, m_i^2}{f_m + \sum f_i\, \beta_i} \tag{1.6}$$

Unlike Bruggeman, the Garnett rule is not symmetric with respect to the inclusions and the matrix, so it is important to choose which material is going to be regarded as the matrix. The Bruggeman rule is useful when grains are mixtures of different materials in similar amounts (such as silicates, carbon, ices and vacuum); instead, when considering contaminations by very small impurities such as metal atoms or PAHs (Sect. 1.3.2), the Garnett rule is more appropriate.

Non-spherical grains and the discrete dipole approximation (DDA)

While we have mentioned uniquely spherical grains until now, many domains – including the study of the ISM, as evidenced by the discovery of interstellar polarization (Sect. 1.3.2) – deal with particles that present some degree of elongation or other types of asymmetry. The effects of shape on the optical properties of dust grains have been computed analytically for infinite cylinders and (in the Rayleigh regime) spheroids. Aside for the effects on polarization, which we will see in Sect. 1.3.2, the main consequence of nonsphericity is to increase the $Q_{\rm abs}$ of the grain in the Rayleigh regime: the effect of this on thermal equilibrium (Sect. 1.2.3) means that nonspherical grains are colder than spherical grains of the same volume (Greenberg & Shah 1971; Siebenmorgen et al. 2014).

For grains of arbitrary shapes one needs to rely on numerical solutions. One of the most common, in which grains are put together out of discrete "building blocks", is the so-called *discrete dipole approximation* or DDA first described by Purcell & Pennypacker (1973). In DDA, a grain subjected to an electromagnetic wave is discretized into an array of subvolumes. If each subvolume is in the Rayleigh regime, their response to the field can be approximated as a dipole. The grain is therefore contructed as an array of dipoles, and its scattering and absorption cross-sections are calculated as the integrated response of the dipoles to the electric field of the incoming electromagnetic wave, including the effects of interaction between dipoles. There is a wide variety of methods to carry out DDA calculations; we will outline briefly here, as an example, the version described by Draine & Flatau (1994). The grain is divided in an array of N subvolumes, denoted by the subscript j; for each subvolume a polarizability α_j can be calculated knowing the target material. If there is an electric field, each subvolume will develop a dipole moment $\mathbf{P}_j = \alpha_j \cdot \mathbf{E}_j$. In the case where there is an incident electromagnetic wave on the grain, $\mathbf{E}_j$ is the sum of the incident wave and the electric field due to the other dipoles:

$$\mathbf{E}_j = \mathbf{E}_{inc,j} - \sum_{k \neq j} \mathbf{A}_{jk} \mathbf{P}_k \tag{1.7}$$

[8] For instance, a spherical dielectric inclusion yields $\beta = \frac{3\, m_m^2}{m_i^2 + 2\, m_m^2}$, where m_m is the refractive index of the medium and m_i that of the inclusion (Kruegel 2003).

where $\mathbf{E}_{inc,j} = \mathbf{E}_0 e^{i\mathbf{k}\cdot\mathbf{r}_j - i\omega t}$, and $-\mathbf{A}_{jk}\mathbf{P}_k$ is the contribution of the dipole k to the electric field in position j. Each element $\mathbf{A}_{jk}$ is a 3×3 matrix. The $\mathbf{P}_j$ are obtained by solving a system of $3N$ complex linear equations

$$\sum_{j=1}^{N} \mathbf{A}_{jk}\mathbf{P}_k = \mathbf{E}_{inc,j} \tag{1.8}$$

Both the absorption and extinction cross section can be calculated from the $\mathbf{P}_j$:

$$C_{ext} = \frac{4\pi k}{\mid \mathbf{E}_0 \mid^2} \sum_{j=1}^{N} \mathrm{Im}(\mathbf{E}^*_{inc,j} \cdot \mathbf{P}_j)$$

$$C_{abs} = \frac{4\pi k}{\mid \mathbf{E}_0 \mid^2} \sum_{j=1}^{N} \mathrm{Im}[\mathbf{P}_j \cdot (\alpha_j)^{-1*}\mathbf{P}^*_j] - \frac{2}{3}k^3 \mid \mathbf{P}_j \mid^2$$

where the asterisk denotes the complex conjugate (Draine 1988). The scattering cross section is obtained as the difference of the previous two: $C_{sca} = C_{ext} - C_{abs}$.

The great advantage of DDA is that it can be used for grains of any shape, even for the optical properties of irregularly-shaped aggregates. On the downside, discretization does not permit using very fine structures: computation times become prohibitively long for grains composed of more than $\sim 5 \cdot 10^4$ dipoles. Furthermore, structures smaller than 2 dipoles on each side tend to give spurious results. This makes it impossible to, for instance, model grains covered with an arbitrarily thin layer of some material.

1.2.3 Dust emission and absorption

The far infrared spectral index β

At first approximation, the extinction efficiency factor in the far infrared and submillimeter follows a power law: $Q_{\mathrm{abs}} \propto \lambda^{-\beta}$, with typical β values around 2. This is consistent with simple models of solid state matter: for instance, since no specific mechanism for absorption and emission is expected in the FIR/mm range in amorphous silicates, the opacity in that range is expected to come from the long-wavelength wings of the observed mid-infrared vibrational bands. If the MIR bands are modelled as (temperature-independent) Lorentz oscillators[9], their asymptotic behaviour is indeed expected to be a power law. The real optical properties are more complex, though, as shown *e.g.* in Coupeaud et al. (2011):

- Q_{abs} increases with temperature in amorphous materials, as tested on a temperature range between 10 and 300 K. On the other hand, β (at a fixed wavelength) decreases with temperature.
- Even at a single temperature, the $Q_{\mathrm{abs}}(\lambda)$ for amorphous materials does not follow a simple power law: the index β should actually be referred to as $\beta(\lambda)$, with a large change in value around 500-700 μm. The nature of the change depends on the material: β increases at long wavelength for the chemical composition of olivine, but it decreases in pyroxene-like materials. The change in β is more evident at low temperature.
- In crystalline materials, however, Q_{abs} is independent of temperature, so whichever process is the cause of it, it only acts in disordered materials.

[9] Lorentz oscillators are employed for crystals, while interstellar dust grains are probably amorphous (Sect. 1.3); however, the asymptotic behaviour of MIR bands is the same in the two cases.

The observed variation of $Q_{\rm abs}$ with temperature is small at temperatures relevant to dust in the diffuse ISM (10-20 K, see following sections), so it does not present a significant problem. The variation of β with wavelength, however, happens right in the middle of the *Planck* bands. Futhermore, there is a non-trivial relation between the optical properties of a single grain and the astronomical observations of dust, which include contributions from grains of disparate sizes, temperatures and compositions. Counterintuitively, this sometimes means that astronomical data is consistent with a single-β model: Coupeaud et al. (2011) show that a mix of dusts of different composition gives a good approximation of a $\beta = 2$ model. This means that the physical meaning of the parameter β should be carefully considered.

Modified black body

Interstellar dust grains absorb energy in the form of photons from the ISRF, which transfer electrons to excited states. The energy can then be reemitted by the electron itself if it is excited enough to be emitted as a "photoelectron", or the state can decay radiatively by emitting a photon (luminescence). Most often, though, the energy is redistributed through the grain in many vibrational modes, *i.e.* heat, to be later emitted as thermal radiation. It is a good approximation, therefore, to equate the power absorbed by the grain to the power emitted by thermal radiation. According to Kirchhoff's law, the emission cross-section at any wavelength is equal to the absorption cross-section at that same wavelength (Kruegel 2003). The emission SED for a population of identical grains is then of the form

$$I_\lambda = \tau_\lambda \cdot B_\lambda(T) \tag{1.9}$$

where $B_\lambda(T)$ is the blackbody emission at the temperature T of the grains and τ_λ is the optical depth (see Eq. 1.1 and following). We will see soon that, at the typical T of dust in the ISM, the Planck function peaks in the far infrared: if we decide to approximate the absorption as a power law (see previous section), we obtain the widely used *modified black body* model of dust emission:

$$I_\lambda = B_\lambda(T) \cdot \tau_0 \cdot (\lambda/\lambda_0)^{-\beta} \tag{1.10}$$

where β its spectral index and τ_0 its optical depth at the reference wavelength λ_0.

A modified blackbody is empirically a good fit to a uniform population of grains in the optically thin limit. However, the conditions under which dust is really a single modified blackbody are generally not met in the ISM. We have already explained how a fixed exponent β is only an approximation of laboratory data. Another issue is that not all grains are going to have the same temperature: the grain equilibrium temperature depends on its size, as we will see later in this section, as well as its composition and structure. This means that thermal emission becomes more complex if dust comprises more than one grain population, as most current models do. Furthermore, the intensity of the ISRF on the line of sight may be not uniform. All the complications listed have the same effect: what we observe is not a single modified blackbody, but a superposition of dust spectra at different temperatures. This introduces a well-known distortion in the fit-derived parameters (*e.g.* Shetty et al. 2009a,b): the superposed modified black body spectra appear as a modified black body with a wider peak. In interpreting this spectrum as a single dust component the fit derives a β that is lower than the actual value; this in turn results in an overestimated T and an underestimated τ_0.

Even with all the complications listed, a modified black body gives a very good fit to the SED of dust at 100 μm or longer, as shown *e.g.* in Planck Collaboration XI (2014). The model parameters thus obtained, however, should be interpreted carefully, as they do not correspond to the local properties of dust, nor they have a simple relation with a mean weighted on dust mass.

Grains at equilibrium temperature

The temperature of a dust grain can be calculated by solving the energy balance:

$$\int_0^\infty Q_{\rm abs}(\lambda)\, I_{\rm ISRF}(\lambda)\, d\lambda = 4\pi \int_0^\infty Q_{\rm abs}(\lambda)\, B_\lambda(T)\, d\lambda \tag{1.11}$$

The result depends on the details of the optical properties of the grain and on the spectral shape of the interstellar radiation field $u_{\rm ISRF}$, but even an approximate treatment can give interesting insights on the matter. We start by noting that, in typical interstellar conditions, the ISRF is most intense in the UV, optical and NIR, while the Planck function for the emission peaks in the far infrared: therefore, the $Q_{\rm abs}$ that are relevant to the left and the right side of Eq. 1.11 belong to different regimes. The right side depends mostly on $Q_{\rm abs}$ in the Rayleigh regime which, as we have seen, is proportional to $a\,\lambda^{-\beta}$, where a is the grain radius and β has a value around 2. In this approximation, the integral of the right side of 1.11 amounts to $a\,T^{4+\beta}$, multiplicative constants aside. This simple result already provides an interesting insight: the power absorbed/reemitted scales like temperature to the fifth or sixth power (depending on the value of β), meaning that it takes a very large variation in absorption and/or in the ISRF to make a significant change in grain temperature. Let us proceed now by regarding the left side of Eq. 1.11 and supposing that, in the UV-NIR range most relevant for absorption, the particles are not much smaller than the wavelength (we will see in the rest of the chapter that this is realistic for grains in thermal equilibrium). In this case no overall trend is evident for $Q_{\rm abs}$ with respect to λ and a (Sect. 1.2.2), so it is reasonable – in first approximation – to adopt a constant close to 1 for the value of $Q_{\rm abs}$. The left side of 1.11 is then independent of both size and wavelength, which leads to $T \propto a^{-1/6}$ (if one takes $\beta = 2$): larger grains are colder grains. See Draine (2011) for a more detailed calculation of T and its dependencies on the ISRF and the grain size.

The relation obtained is however valid only for a certain range of sizes. For grains that are small enough, the right side of Eq. 1.11 is also in the Rayleigh limit: then the dependence of $Q_{\rm abs}$ on a cancels out, and grain temperature becomes independent of size. Similarly, if grains were large with respect to wavelength both in emission and in extinction (which would require much larger grains than those found in the ISM, but should happen in planetary disks), $Q_{\rm abs}$ would be independent of grain size and the temperature would level off to some limit.

Stochastically-heated grains

All of the previous section is based on an unstated assumption: that a dust grain balances absorption and emission by reaching a well-defined temperature. However, as Greenberg (1968) was the first to realize, very small particles might not have a stable temperature. Every single absorbed photon increases the internal energy of a grain by a discrete amount; in a particle small enough that its energetic content is not large compared to the photon's, this means that the temperature also increases by a discrete amount. Since radiative cooling is more efficient at high temperature, and the smaller a particle is the sparser are its interactions with photons, a very small particle also has time to cool significantly between absorption events. Fig. 1.5 shows the temperature as a function of time for graphite particles: it is evident that, for typical ISRF intensities (left panel), only grains with $a \sim 20$ nm or larger can be said to have an equilibrium temperature. The right panel shows the time-dependent temperature for the same grains in a ISRF which is 100 times more intense than the average: here, due to the more frequent photon events, even grains as small as 5 nm have constant temperatures; however, the smallest grains still show very large fluctuations. For this reason small grains are described by a *temperature distribution* $P(T)$ rather than by a single temperature T like larger grains. Everything else being equal, $P(T)$ becomes wider as grains become smaller, as shown in Fig. 1.6.

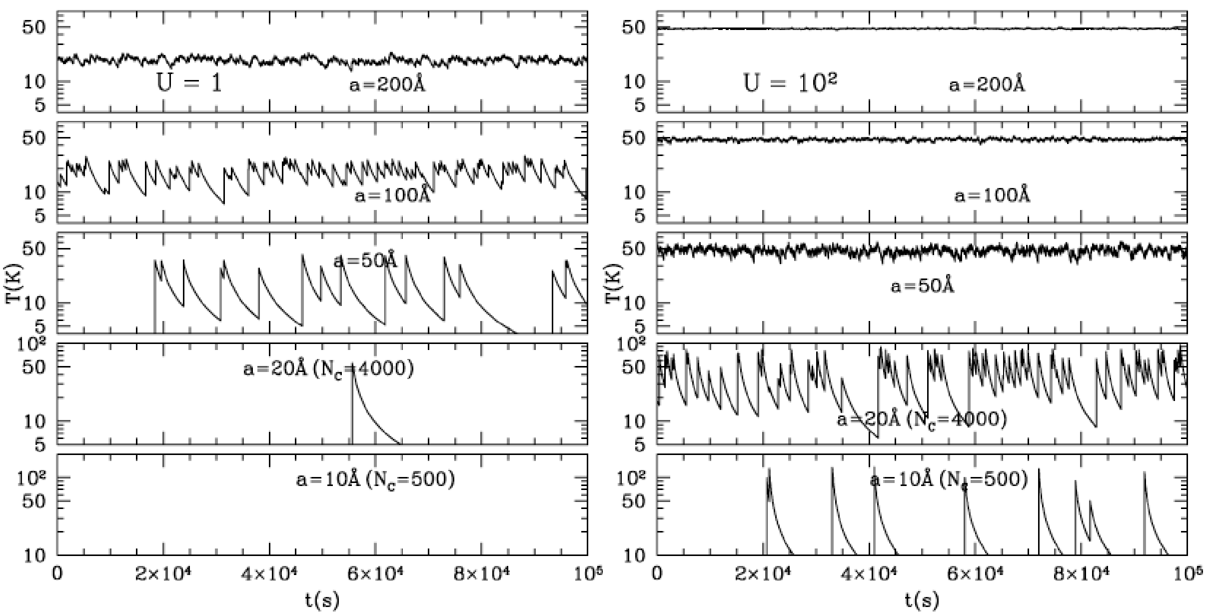

Fig. 1.5. Simulations of dust grain temperature as a function of time, for different grain sizes and ISRF intensities. The larger temperature fluctuations in smaller grains are evident. From Draine (2011)

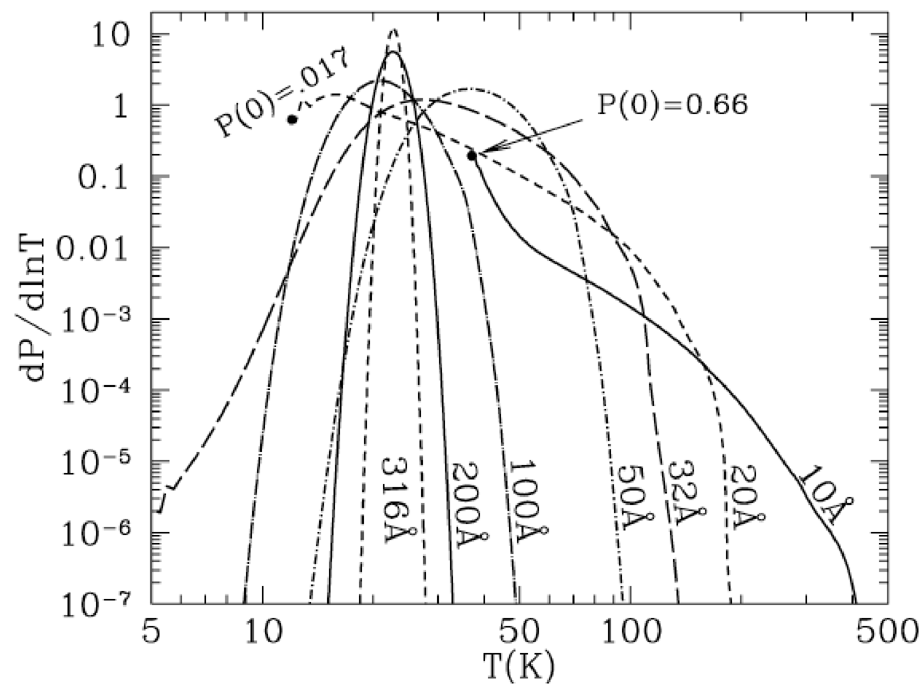

Fig. 1.6. Temperature distribution function $dP/d\ln T$ for carbonaceous grains, calculated at seven different sizes. From Draine (2011)

Albedo

The albedo is defined as the ratio of scattering over total extinction (Whittet 2003):

$$Al = \frac{Q_{\rm sca}}{Q_{\rm ext}} \tag{1.12}$$

and by definition it is a real number between 0 and 1.

Albedo provides the most basic information on the scattering properties of a particle; for a more complete description one would need the full scattering function $\Phi(\Theta)$, *i.e.* the amplitude of the scattered radiation as a function of the angle Θ between the direction of the incident light and the direction of scattering: in case of axial symmetry, this means $C_{\rm sca} = 2\pi \int_0^\pi \Phi(\Theta)\, \sin(\Theta)\, d\Theta$.

A more concise representation of the scattering properties of the particle is given by the *asymmetry factor* g, which is the mean value of $\cos(\Theta)$ weighted over the scattering function:

$$g = \frac{C_{\rm sca}}{2\pi} \frac{\int_0^\pi \Phi(\Theta)\, \cos(\Theta)\, \sin(\Theta)\, d\Theta}{\int_0^\pi \Phi(\Theta)\, \sin(\Theta)\, d\Theta} \tag{1.13}$$

g is a number between -1 (completely backward-directed scattering) and 1 (completely forward-directed scattering). Isotropic scattering implies $g \sim 0$, but the opposite is not true ($g \sim 0$ can be obtained by any function with back-to-front symmetry).

1.3 Interstellar dust observations and models

An interstellar dust model is characterized by the abundance of the elements locked up in the dust, as well as the details of the composition of grains and their morphology and size distribution. An ideal interstellar dust model should fit all of the observational constraints on dust; a real dust model may not fit all constraints at once – also because they show regional variations – but it should be able to simultaneously fit at least a basic set of constraints. The current observational constraints on dust comprise (Dwek 2005; Jones et al. 2013):

- The wavelength-dependent extinction;
- The thermal emission SED;
- The elemental abundance constraints that come from ISM elemental depletion;
- The polarization of both starlight and thermal dust emission;
- The dust albedo and scattering;
- The “anomalous” microwave emission;
- The extended red emission seen in various nebulae (Berné et al. 2008 and refs. therein);
- The materials of interstellar origin found in meteorites;
- The production of photoelectrons needed to heat the neutral photodissociation regions;
- The observations pertaining to X-ray sources, such as diffraction haloes and the fine structure in the X-ray absorption edges (*e.g.*, Costantini et al. 2005);

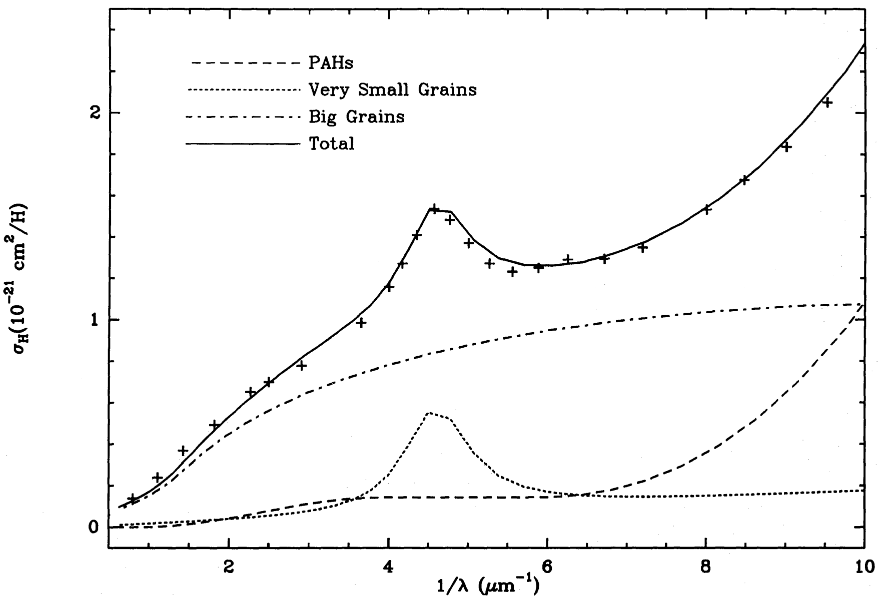

Fig. 1.7. The extinction curve of the diffuse ISM at UV and visible wavelengths. The total curve as well as the individual contributions of the three dust components are shown. Big grains dominate in the visible and IR (approximately $\lambda > 500$ nm or $1/\lambda < 2\,\mu\mathrm{m}^{-1}$), but the contribution of the PAHs, the smallest grains, explodes at short wavelengths. In this model the 217-nm bump comes from the very small carbonaceous grains and the FUV rise from the PAHs, but different models may have different subdivisions. From Desert et al. (1990).

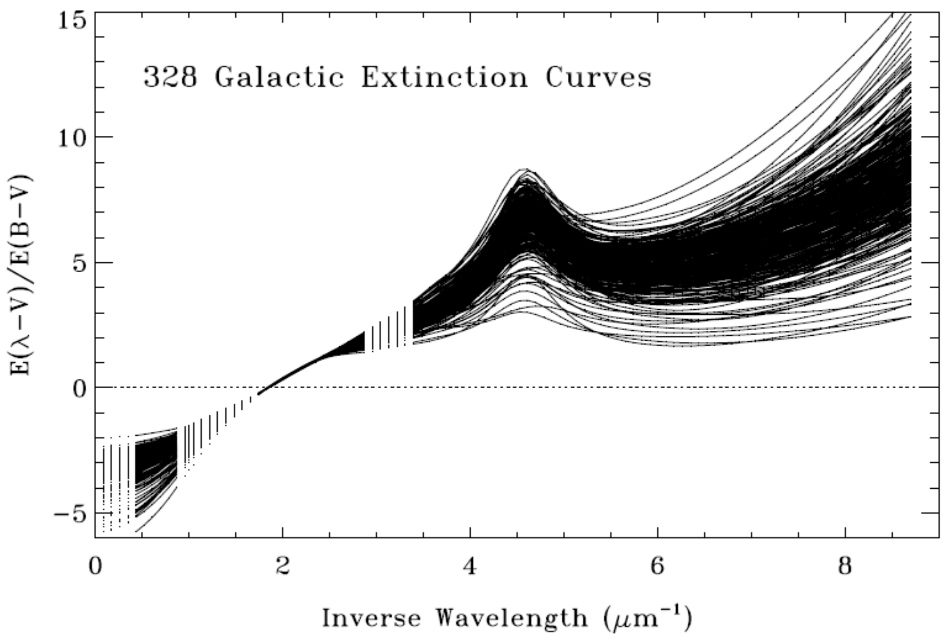

Fig. 1.8. Variations in the Galactic extinction curve. The apparent uniformity of extinction curves near the V band is an artefact of normalization. From Fitzpatrick & Massa (2007)

1.3.1 Dust observables (unpolarized)

Extinction curve

The so-called *extinction curve* is the wavelength-dependent dust extinction A_λ. It is often shown as a function of the inverse wavelength, $1/\lambda$, when one needs to put in evidence its features in the ultraviolet. The average Galactic extinction curve has the shape shown in Fig. 1.7, although it can present variations (Fig. 1.8); also, the average extinction curve in other galaxies can have very different shapes (*e.g.* Li et al. 2015 and refs. therein). As we can see in Fig. 1.7, the extinction curve presents three main features:

A linear component, proportional to λ^{-1}. This is especially visible between ~ 1 and $\sim 2\ \mu\text{m}^{-1}$, but it also extends in the ultraviolet, beneath the other features. Since for grains larger than the wavelength extinction tends to flatten (geometrical optic limit, see Sect. 1.2.2), the presence of a rise in extinction at short wavelengths means that the dust size distribution must extend to extremely small grains – this is why the power-law distributions introduced by Mathis et al. (1977) have been so successful (see Sect. 1.3.3).

The 2175 Å bump, a broad absorption feature of variable intensity and width, but remarkably constant central wavelength. It is thought to come from the $\pi \rightarrow \pi^*$ transition in small carbonaceous particles. While historically it has been explained with graphite particles, most modern models attribute it to PAHs (Sect. 1.3.3). Other materials are however possible: nanoparticles of the a-C(:H) material proposed in Jones et al. (2013) are an example that we will see better in Sect. 1.3.3 and Ch. 2.

The FUV rise, a non-linear increase in slope in the far ultraviolet (FUV) beyond $5\,\mu\text{m}^{-1}$ ($\lambda < 200$ nm). This is interpreted as a contribution from a population of extremely small grains ($\lesssim$nm) in the Rayleigh regime.

A measure of the amount of dust extinction is the V-band extinction A_V, *i.e.* the extinction integrated over the visual or V photometric band, centered around 550 nm with a FWHM of 90 nm. Another measure of dust extinction is the differential extinction – or reddening – E(B-V), *i.e.* the difference between extinction in the blue B-band (450 nm center, 90 nm FWHM) and in the V-band. The ratio of total to differential extinction, $R_\text{V} = A_\text{V}/\text{E(B-V)}$, measures (the inverse of) the slope of the linear region, and thus the typical size of the grains: R_V gets higher (otherwise said, extinction becomes grayer) for larger grain sizes. In the optical regime extinction would be flat ($Q_\text{abs} = 2$), meaning an infinite R_V. The typical value for R_V in the diffuse ISM is 3.1, but in some dense regions it can reach values greater than 5 (Cardelli et al. 1989; Mathis 1990).

In the infrared the extinction curve is compatible with a simple power law, $A_\lambda \propto \lambda^{-\alpha}$. Earlier observations suggested that the power law exponent α be essentially fixed (Mathis 1990), with value of ~ 1.84, but the notion of a universal α has been challenged by more recent results (Fitzpatrick & Massa 2009). The infrared is also interesting because of the information provided by infrared extinction features. While the only feature found in the UV range is the aforementioned 2175 Å bump, which indicates the presence of aromatic carbonaceous materials, the rich spectroscopic features of the infrared extinction curve provide a wealth of information on the dust composition. The two best known bands are those at 9.7 and 18 μm (Fig. 1.9), which are proof of the presence of silicates: they correspond to the Si–O stretching and O–Si–O bending mode, respectively. The fact these bands are wide and smooth indicates that interstellar silicates are mainly amorphous, since the features of crystalline silicates are narrow and sharp. Another important absorption feature at 3.4 μm is typical of the C–H stretch mode and indicates the presence of aliphatic carbon in the ISM. Inside molecular clouds ($A_\text{V} \gtrsim 3$) dust grains accrete mantles of volatile ices, which provide

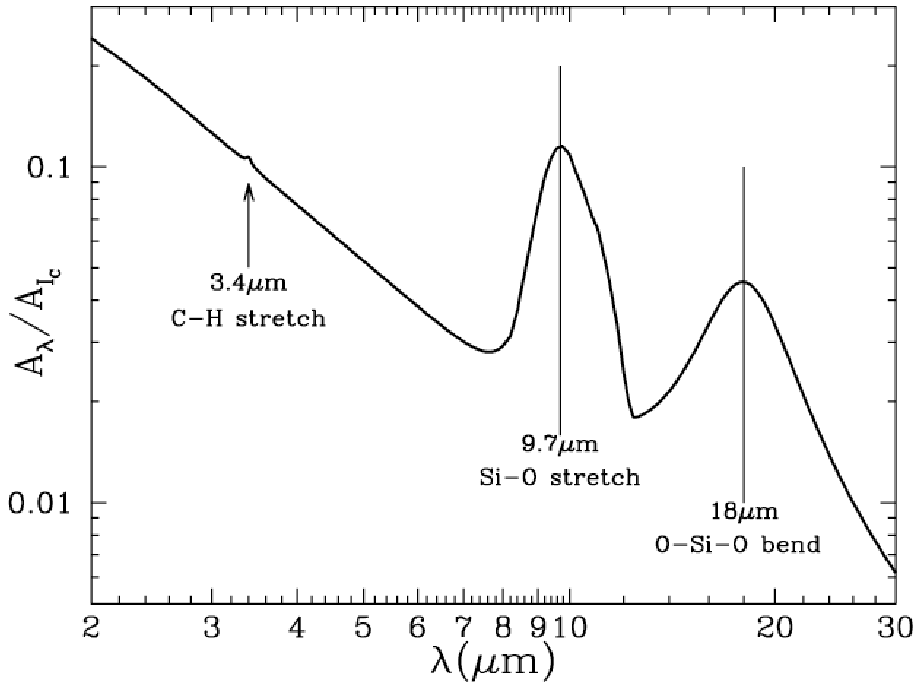

Fig. 1.9. Typical IR extinction curve showing the absorption bands of aliphatic carbon (3.4 μm) and amorphous silicates (9.7 and 18 μm). From Draine (2011)

many more identifiable molecular lines; one of the most often mentioned is the 3.05 μm line for the O–H stretching mode typical of H_2O ice.

Due to the fact that dust and gas are well mixed, extinction does not only give information about dust: it can also be used as a tracer of the gas column density, which makes it an invaluable tool in the calculation of the masses of clouds and galaxies. In this kind of calculations a conversion ratio, assumed fixed, is applied to a measure of extinction: A_V or E(B-V) are often used, but extinction in a NIR band is also a common choice because of the relative invariance, in these bands, of extinction with anything else but dust mass. A typical E(B-V)-to-column-density conversion ratio is $5.8 \cdot 10^{20}$ H cm^{-2} mag^{-1}, from the seminal work of Bohlin et al. (1978) and confirmed by Rachford et al. (2009).

Emission SED

Dust grains in the ISM can absorb energy, mainly in the form of interstellar radiation, which they emit back in the form of thermal radiation. Thus, thermal dust emission can be observed, covering wavelengths between the NIR and the microwave range. The typical dust SED, shown in Fig. 1.10, can again be separated in 3 components:

NIR and MIR emission bands that are observed between 3 and 30 μm (see *e.g.* Tielens et al. 1999 for a review). Since these bands correspond to bending and stretching modes of C–H and C–C–C bonds, they have been attributed to the so-called *polycyclic aromatic hydrocarbons* or PAHs: molecules composed of aromatic carbon rings and hydrogen (Leger & Puget 1984; Allamandola et al. 1985; Li & Draine 2001). As seen in Sect. 1.2.3, PAHs are too small to attain thermal equilibrium: for this reason they are at times well above equilibrium temperature, and most of the energy is radiated away at short (near- and mid-IR) wavelengths. Alternatives to

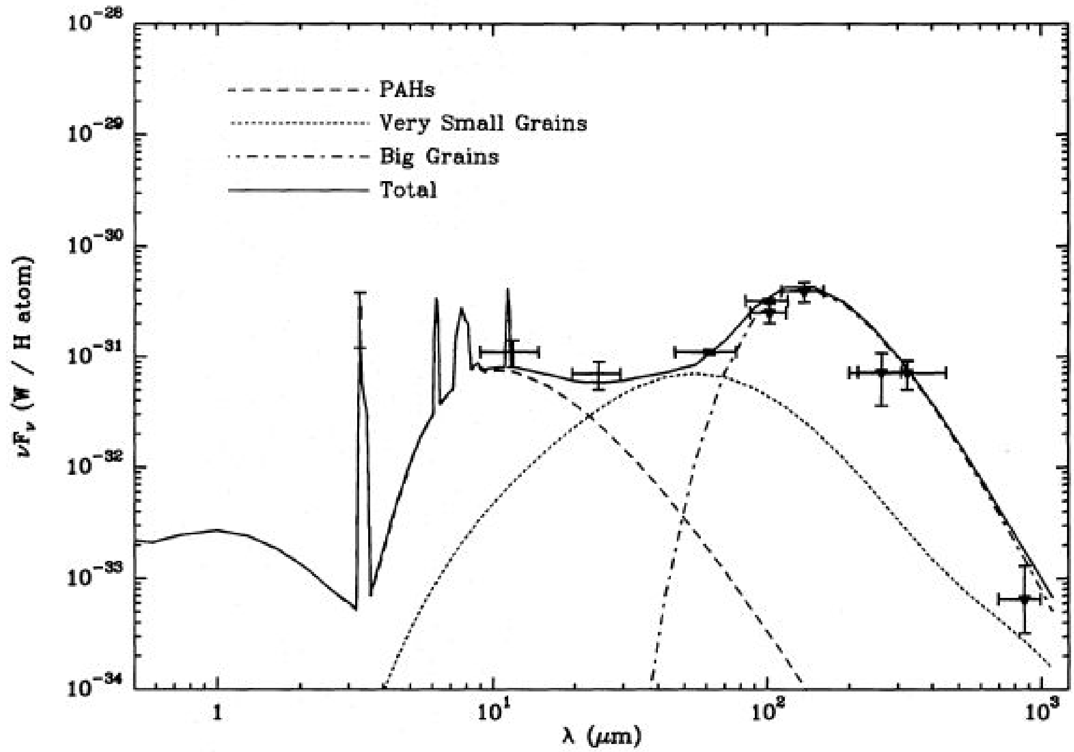

Fig. 1.10. Model of the interstellar dust emission for the diffuse ISM. Each of the three components dominates a different wavelength range. From Desert et al. (1990).

PAHs as the carriers of these bands exist (see *e.g.* Jones et al. 2013 and Ch. 2 of this thesis), but all of them are carbonaceous particles of molecular size.

A continuum between 20 and $\sim 100\,\mu$m which is in excess of the spectrum extrapolated from grains in thermal equilibrium (see below). To explain this, a population of very small grains (VSGs) is usually invoked. These are grains still small enough that they are not in thermal equilibrium, but they present a narrower temperature distribution than the carriers of NIR/MIR bands. They are also large enough that quantum effects are not readily apparent, so that they radiate in a continuum rather than in bands.

An emission continuum at $\sim 100\,\mu$m and beyond which can be very well fit with a modified black body, peaking around $140\,\mu m$. This emission is thought to come from big grains contributing most of the visible and infrared extinction: these grains are large enough to be in thermal equilibrium with the interstellar radiation field, so they have a constant temperature of $\sim$ 20K in the diffuse ISM[10].

Since dust emission – like extinction – is proportional to dust mass, it is a common practice in astrophysics to calculate ISM column densities by converting FIR and submm maps into extinction, with a conversion factor (Schlegel et al. 1998 being one of the most used maps). The maps thus obtained have the advantage of tracing all of the ISM and not only the matter that is between the

[10]Even the T of big grains is not completely uniform, since several populations of big grains may coexist, each with different absorption and emission efficiencies and therefore a different equilibrium temperature. Even within a single population, big grains with different sizes will have different Ts. However, temperature variations between big grains are not important enough to qualitatively modify the emission spectrum.

observer and the source on which extinction is observed. Also, maps from emission are naturally continuous, while extinction maps derived from the reddening of background sources need to be interpolated. The constancy of the conversion factor however is a concern, and we will also see this better in Ch. 3.

Elemental abundances

The composition of interstellar dust can be constrained by studying the composition of the ISM. The measured elemental abundances in a reference phase – the Sun's surface or, more recently, B-type young stars – are compared to the observed gas-phase abundances in the different phases of the ISM. In this way it was discovered that several elements are less abundant in the ISM than in the reference phase, sometimes by a large factor: this phenomenon is called *depletion*. These elements, which are called *metals*[11], are mainly Fe, Si, Mg, and to a smaller extent C and O, all constituents of dust (Savage & Sembach 1996).

Direct analysis: meteoric and interplanetary grains

Dust grains from the ISM have entered the Solar System during its formation and were included in meteors. Today, these so-called *pre-solar grains* can be found inside meteorites and their study provides important insights on the matter outside the Solar System (See *e.g.* Anders & Zinner 1993; Zinner 1998; Clayton & Nittler 2004). Since the material of the solar nebula has been heavily processed in the formation of the Solar System, the signature of presolar materials has been lost for the most part. However, some meteorites such as carbonaceous chondrites – which form at a relatively low temperature (~ 350 K) – conserved some grains in a relatively unchanged state (*e.g.* Cameron 1973).

Materials whose extrasolar origin has been identified so far include nano-diamonds, silicon carbide (SiC), graphite, silicon nitride (Si_3N_4) and oxides such as corundrum and spinel (see Anders & Zinner 1993; Zinner 1998; Clayton & Nittler 2004 for overviews). A class of amorphous silicate grains with metallic/sulfide inclusion, the GEMS[12] (*Glass with Embedded Metal and Sulfides*, Bradley 1994) is particularly interesting because, since their origin is interstellar at least in part (Keller & Messenger 2011), they may give insight on both the composition and the structure of interstellar big grains.

Extrasolar grains are recognizable thanks to their isotopic abundances, that present huge anomalies compared to solar abundances. These anomalies are explainable if grains formed in stellar environments – such as supernovae, AGB stars, novae – where nucleosynthetic processes enriched them in particular isotopes. For instance, nano-diamonds are found to contain xenon that is enriched in both high- and low-mass isotopes, and is therefore called Xe-HL. These isotopes are typical of supernova processes – photodisintegration of nuclei, neutron or proton captures (Heymann & Dziczkaniec 1979)) – so nano-diamonds have a clear supernova origin. SiC grains have more varied origins, but a high $^{20}Ne/^{22}Ne$ ratio – where ^{22}Ne is attributed to ^{22}Na decay – is an indicator that the grain has originated in a nova (Amari et al. 1995). Therefore, the importance of studying these isotopic anomalies transcends interstellar dust: after identifying the stellar environment of dust formation, it gives constraints on models of stellar nucleosynthesis. An example of how nova nucleosynthesis can be constrained through pre-solar grain isotopic composition is in José et al. (2004) and references therein.

[11] In astrophysics, the term "metal" refers to all those elements that are neither hydrogen nor helium.

[12] There is no relation between these and "*Planck*'s Dusty GEMS" (*Gravitationally Enhanced subMillimetre Sources*) recently described in Cañameras et al. (2015).

1.3.2 Dust observables (polarized)

Light polarization

In addition to intensity and frequency, electromagnetic radiation is characterized by its state of polarization. Let us consider a plane monochromatic wave propagating in the z direction:

$$\mathbf{E} = \mathbf{A}\cos(kz - \omega t) - \mathbf{B}\sin(kz - \omega t)$$

where the real vectors $\mathbf{A}$ and $\mathbf{B}$ are independent of position. At a fixed position, such as $z = 0$, the electric vector traces an ellipse over time, called the vibration ellipse:

$$\mathbf{E} = \mathbf{A}\cos\omega t + \mathbf{B}\sin\omega t$$

We then say that the wave is *elliptically polarized*. Elliptical polarization is the most general polarization possible for a monochromatic wave. Particular cases arise when either $\mathbf{A}$ or $\mathbf{B} = 0$, in which case the ellipse degenerates into a segment and the light is *linearly polarized*; and when $|\mathbf{A}| = |\mathbf{B}|$ and $\mathbf{A}\cdot\mathbf{B} = 0$, in which case the ellipse is a circle and the light is *circularly polarized*.

An arbitrary monochromatic beam can be decomposed into two beams with orthogonal polarization: for instance, two linearly polarized beams with orthogonal directions of polarization, or two circularly polarized beams with opposite handedness (the direction of rotation of the electric vector: clockwise and counterclockwise rotations are orthogonal). This is not only a mathematical artifice; as we will see in the next paragraphs, one can build a polarizer that transimits only one of these components (Bohren & Huffman 1983).

The polarization of light can be completely characterized using the parameters of the vibration ellipse: axial ratio, azimuth of the long axis and handedness. However, these quantities are not practical, mainly because they are very hard to measure. In practice, polarization is usually described in tems of the *Stokes parameters*, an equivalent description of polarized light with much greater usefulness.

Stokes parameters

To introduce the Stokes parameters and how they can be measured, let us consider an experiment consisting of a monochromatic beam shot through a perfect polarizer (*i.e.* a polarizer that does not change the amplitude of the transmitted component) and into a detector that measures the beam intensity, independent of polarization.

The electric field, referred to two orthogonal unitary vectors $\hat{\mathbf{e}}_\parallel$ and $\hat{\mathbf{e}}_\perp$, is $\mathbf{E} = \mathbf{E_0}\, e^{ikz - i\omega t}$, with $\mathbf{E_0} = E_\parallel\,\hat{\mathbf{e}}_\parallel + E_\perp\,\hat{\mathbf{e}}_\perp$. If no polarizer is in front of the detector, this will measure an intensity $I = E_\parallel\, E_\parallel^\star + E_\perp\, E_\perp^\star$. Now let us consider a linear polarizer that only transmits the component parallel to $\hat{\mathbf{e}}_\parallel$: the radiance is now $I_\parallel = E_\parallel\, E_\parallel^\star$. When the same polarizer is rotated by 90° to only transmit the component parallel to $\hat{\mathbf{e}}_\perp$ the radiance becomes $I_\perp = E_\perp\, E_\perp^\star$. A measure of linear polarization is then $Q \equiv I_\parallel - I_\perp = E_\parallel\, E_\parallel^\star - E_\perp\, E_\perp^\star$. What happens if the linear polarizer is at 45° angles from the $\hat{\mathbf{e}}_\parallel$ and $\hat{\mathbf{e}}_\perp$ unit vectors, rather than parallel or perpendicular to them? Let us call I_+ (respectively I_-) the intensity transmitted by a polarizer turned by +45° (−45°) with respect to $\hat{\mathbf{e}}_\parallel$. A measure of linear polarization is then $U \equiv I_+ - I_- = E_\parallel\, E_\perp^\star + E_\perp\, E_\parallel^\star$. Note that the values of Q and U depend on the choice of the basis vectors $\hat{\mathbf{e}}_\parallel$ and $\hat{\mathbf{e}}_\perp$. Finally, with circular polarizers one can measure the transmitted intensity for right-circular and left-circular light, I_R and I_L. Circular polarization can be parametrized by $V \equiv I_R - I_L = i(E_\parallel\, E_\perp^\star - E_\perp\, E_\parallel^\star)$ (Bohren & Huffman 1983).

To resume,

$$\begin{aligned} I &= E_\parallel\, E_\parallel^\star + E_\perp\, E_\perp^\star \\ Q &= E_\parallel\, E_\parallel^\star - E_\perp\, E_\perp^\star \\ U &= E_\parallel\, E_\perp^\star + E_\perp\, E_\parallel^\star \\ V &= i\,(E_\parallel\, E_\perp^\star - E_\perp\, E_\parallel^\star) \end{aligned} \tag{1.14}$$

It should be noted that, while the mathematical formulation in Eq. 1.14 is only valid for monochromatic beams, the empirical definition that precedes it is independent of all assumptions on the beam.

The four Stokes parameters provide the same information as the three ellipsoidal parameters, meaning that they are not independent of each other: one has $I^2 \geq Q^2+U^2+V^2$, where the equality is valid for completely polarized light and the right side is 0 for unpolarized light.

Polarization intensity and angle: P and ψ

When one works on linear polarization the quantities Q and U are sometimes impractical, since they both depend on the local frame of reference for polarization and therefore change with rotation, in a way not independent of one another. It is thus common to build from them a measure of linear polarization that does not depend on rotation: the *polarized intensity* $P = \sqrt{Q^2 + U^2}$. This quantity is equivalent to the maximum intensity that could be transmitted by a perfect polarizer on which a beam of intensity I shines. The *polarization fraction* P/I is also used.

The angle information that is lost in P can be summed up in another quantity: the *polarization angle* or *direction*, $\psi = \frac{1}{2}\arctan(U, Q)$. Remark that the use of the notation $\arctan(U, Q)$ rather than $\arctan(\frac{U}{Q})$ implies that the angle has a periodicity of 180°; with the definition we gave it is defined on the range $[-90°, 90°]$. The Stokes parameters Q and U can be obtained back from P and ψ using the formulas $Q = P\cos(2\psi)$, $U = P\sin(2\psi)$.

While P is in many ways more practical than Q and U, it has a drawback: since it is a quadratic quantity, if there is any noise on Q and U the calculated value of P will be positively biased, as was shown *e.g.* by Simmons & Stewart (1985)[13]. It can be shown that, if the actual polarization intensity is P_0 the observed polarization squared P^2 has an expectation value of $P_0^2+\sigma_\mathrm{P}^2$ for gaussian noise, where σ_P is the uncertainty on P. Clearly, the bias is important mainly in cases with low S/N. Several debiasing methods for P have been created, as described *e.g.* in Montier et al. (2015).

Starlight polarization

It has been observed that the light from stars is, sometimes, linearly polarized to a few percent, and that this polarization is correlated with the reddening from extinction (Hall 1949; Hiltner 1949a,b). It was soon understood that this phenomenon was due to the extinction from non-spherical dust grains (Davis & Greenstein 1951)[14]. Grains damp better the component of the oscillating electric field that is parallel to their longer axis, meaning that unpolarized light, passing through a grain,

[13] The simplest way of seeing this is to imagine the case where the true values of Q and U – call them Q_0, U_0 – are 0. The measured values of Q and U may be positive or negative due to noise, but $P^2 = Q^2 + U^2$ will invariably be positive.

[14] Dust grains can polarize radiation even when they are spherical, through Mie scattering: if unpolarized light shines on a sphere, the scattered light has a polarization that depends, on the grain composition, on the size of the grain compared to the wavelength, and on the direction of scattering (Kruegel 2003). However, one constant aspect in the complex panorama of scattering on spheres is that forward-scattered and backward-scattered light always has zero polarization. In the type of polarization that we are discussing, the polarizer (dust) lies on the line of sight between the observer and the star, meaning that we only observe forward-scattered light. The fact we observe polarization therefore requires the dust grains to be non-spherical.

gets polarized perpendicular to the grain's long axis. If grains in the ISM were randomly oriented, the overall effect on starlight polarization would be zero; however, grains tend to orient their short axis parallel to the local magnetic field. The observation of starlight polarization therefore showed at once that dust grains are nonspherical, that a Galactic magnetic field exists, and gave an observable to trace its orientation – or at least its projection on the plane of the sky.

It was predicted that the thermal emission of dust should also be polarized (Stein 1966), once again because the emission is more efficient for the polarization parallel to the longer axis of the grain. When far infrared and submillimeter observation became widespread, this was indeed found to be the case. Remark that, since the axis of maximum thermal emission is also the axis of maximum starlight damping, the polarization of starlight and that of dust thermal emission are perpendicular to each other.

When the ISM is polarizing its optical depth depends on the direction of polarization of the light that passes through. We can thus define the optical depth for the direction of polarization that gets maximally damped, $\tau_\perp$, and the optical depth for the direction of polarization that gets minimally damped, $\tau_\parallel$. The two polarizations in question are perpendicular to each other; the names of the two optical depths were chosen because they correspond to the optical depths of the directions orthogonal and perpendicular to the observed polarization of starlight.

Following Draine & Fraisse (2009) we divide equally, between the two polarization modes, the flux I_0 of incident light before extinction. After extinction the flux is $I_0(e^{-\tau_\parallel} + e^{-\tau_\perp})/2$ and the polarization fraction is

$$p = \frac{e^{-\tau_\parallel} - e^{-\tau_\perp}}{e^{-\tau_\parallel} + e^{-\tau_\perp}} = \tanh(\Delta\tau) \tag{1.15}$$

where $\Delta\tau = (\tau_\parallel - \tau_\perp)/2$. In term of grain properties, this means that polarization depends directly on $C_{\mathrm{ext},\parallel} - C_{\mathrm{ext},\perp}$, which of course opens the question of how to calculate these cross-sections when they depend on the grain orientation.

Polarization cross-section for spheroidal grains

The polarization of starlight and dust emission does not tell us anything about the shape of the grains except that they are not spherical. The first models that attempted to reproduce polarization used grains in the shape of infinitely long cylinders, the only shape other than spheres for which analytical calculations are possible. Nowadays, more realistic spheroidal models are usually employed: for these, an analytical expression of the polarization efficiency can also be obtained in the Rayleigh regime.

A spheroid is an ellipsoid with two axes of equal length, and it is characterized by the lengths a and b of its axes, where a is the axis of rotational symmetry and b is the length of the other 2 axes. Oblate (flattened) spheroids have an axial ratio $b/a > 1$, while prolate (elongated) spheroids have $b/a < 1$.

A grain's polarization cross-section ultimately depends on the difference between the extinction cross-sections at different orientations, as well as the orientation of the grain compared to the incident light. The extinction cross-sections for spheroidal grains are, as per Li et al. (2002),

$$C_{\mathrm{abs}}^{\parallel,\perp} = \frac{2\pi}{\lambda V} \mathrm{Im} \left\{ \frac{m^2 - 1}{(m^2 - 1)\, L^{\parallel,\perp} + 1} \right\} \tag{1.16}$$

where V is the particle volume and the factor $L^{\parallel,\perp}$ is the shape depolarization factor for the light polarized, respectively, parallel or perpendicular to the symmetry axis of the spheroid. The shape

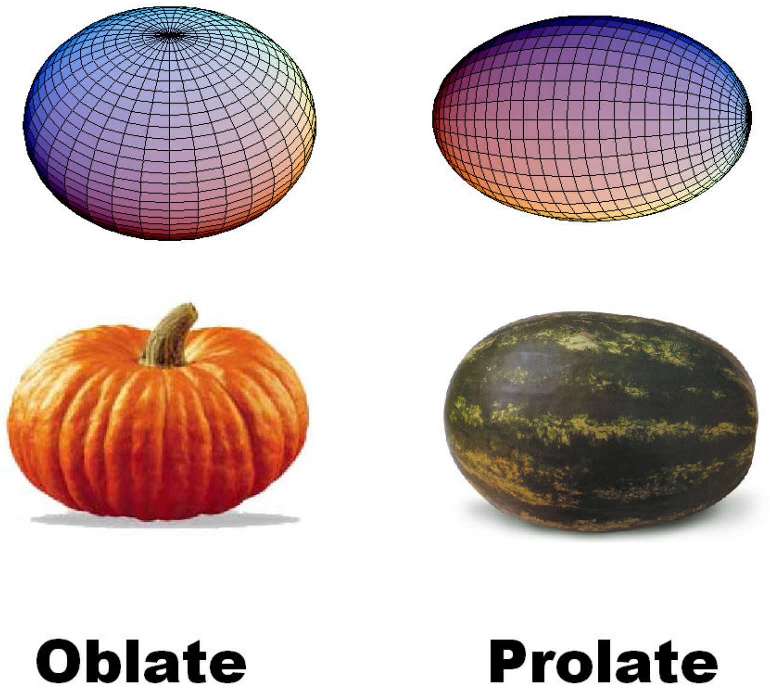

Fig. 1.11. Schema of oblate and prolate spheroids.

factor is equal to

$$L^{\parallel} = \begin{cases} \frac{1-e^2}{e^2}\left[\frac{1}{2e}\ln\left(\frac{1+e}{1-e}\right)-1\right], & e=\sqrt{(b/a)^2-1} \qquad \text{for oblates} \\ \frac{1-e^2}{e^2}\left(1-\frac{1}{e}\tan^{-1}e\right), & e=\sqrt{1-(b/a)^2} \qquad \text{for prolates} \end{cases} \tag{1.17}$$

where e is the eccentricity of the spheroid and $L_{\perp} = (1 - L^{\parallel})/2$.

The Rayleigh reduction factor

The observed polarization cross-section for grains depends on the grain orientation compared to the direction of light propagation, the latter of which corresponds to the line of sight to the observer. Since the grain orientation ultimately depends on the direction of the magnetic field lines, it can be described in terms of two angles: the angle β between the grain's symmetry axis and the field line and the angle between the line of sight and the field lines, or its complementary, the more commonly used angle γ between the plane of the sky and the field line. One has maximum polarization cross-section when the alignment is perfect ($\beta = 0$) and the magnetic field is parallel to the plane of the sky ($\gamma = 0$). When grains are not in these condition, the polarization cross section is decreased. In the Rayleigh regime it can be calculated analytically (Greenberg 1968) that the polarization cross-section, after averaging on grain spinning, is

$$P = P_{\max} R \cos^2 \gamma \tag{1.18}$$

where the factor R, which depends uniquely on β, is the so-called Rayleigh Reduction Factor

$$R = \frac{3}{2}(\cos^2\beta - \frac{1}{3}) \tag{1.19}$$

In most cases, not all interstellar grains will have the same β, so R comes from an average on the β distribution. The Rayleigh reduction factor equals 1 for perfect alignment ($\cos^2\beta = 1$ for all grains) and 0 for randomly aligned grains ($\langle\cos^2\beta\rangle = 1/3$).

Eq. 1.18 is certainly valid for polarization in emission, which is seen in the far infrared and therefore in the Rayleigh regime. The same formula is not valid for polarization in extinction, which is mainly observed in the optical and near-infrared wavelength: while it is often used to obtain a rough estimate of polarization in extinction from models, one is likely to introduce some systematic error in doing so.

Line-of-sight depolarization

Another polarization reduction factor arises from a disordered magnetic field. Starlight that passes through several dusty regions, each with a different magnetic field (and dust grain) orientation, will be less polarized than if it had passed a single region of uniform magnetic field orientation. This effect is called line-of-sight depolarization. This can be more easily visualized by considering the extreme case: starlight, having been polarized by the aligned dust in a region, enters a new region where the magnetic field is rotated by 90°, so the dust now depolarizes the light.

Lee & Draine (1985) show that the effect of depolarization, under a few assumptions, is similar to imperfect alignment. Let us decompose the magnetic field into a uniform (or "ordered") component plus a random ("disordered") component, and call θ the angle between the two components. If the random component is azimuthally symmetric, it can be shown that Eq. 1.18 becomes $P = P_{\max}\, R\, F\, \cos^2\gamma$, where we have defined the line-of-sight depolarization factor $F = \frac{3}{2}(\langle\cos^2\theta\rangle - \frac{1}{3})$.

Alignment processes

As we have seen the polarization of radiation by dust, both in extinction and in emission, implies that dust grains are non-spherical and that they are oriented by some mechanism. Today we know that the orientation is given by the local magnetic field, but the process or processes involved are still a matter of debate. Here we expose the most popular ones, following Hildebrand (1988), Kruegel (2003), Andersson (2012) and references therein.

To understand the reasons for grain alignment we must first understand the basics of grain dynamics. Dust grains in space can be assimilated to spinning tops: first, they are in rotation due to the random impacts with gas atoms and molecules; second, their axis of rotation coincides with their axis of greater moment of inertia due to several damping effects; finally, their rotation axis precesses around the magnetic field lines due to their magnetic moment acquired through the Barnett effect (Barnett 1915) just like a spinning top precesses around the vertical (a "gravitational field line", if one wills). Given these properties of the grain, the following scenarios are possible:

Magnetic relaxation: originally proposed by Davis & Greenstein (1951). Silicate grains, containing iron atoms, are paramagnetic, and therefore in a magnetic field $\mathbf{B}$ they acquire a dipole moment: $\mathbf{m} = V\chi\mathbf{B}$, where V is the grain volume and χ is the magnetic susceptibility. The torque that the magnetic field exerts on a magnetized grain is $\tau = \mathbf{m}\times\mathbf{B}$; since χ is complex, the dipole moment $\mathbf{m}$ "lags behind" during the rotation and it is not parallel to $\mathbf{B}$, meaning that the torque is non-zero (Kruegel 2003). This torque dissipates rotational energy and causes a change in angular momentum that lies in the same plane as $\mathbf{B}$ and the rotation axis; the final result is that the rotation axis aligns with the magnetic field, after which the torque is zero.

It was found that the original Davis-Greenstein mechanism, employing paramagnetic grains and "thermal " rotation caused by impacts with atoms, cannot work in the ISM under normal conditions: the timescale to align grains (10^6 yr) would be much longer than the timescale for impacts to disalign the grain. Several proposed scenarios can help solve this problem. **Superparamagnetism** (Jones & Spitzer 1967) is a phenomenon found in paramagnetic materials with small inclusions of ferromagnetics, small enough that each inclusion behaves like a single domain. The resulting material behaves qualitatively like a paramagnet, but with magnetic susceptibilities up to 10^6 times larger, of the order of those found in ferromagnets. The torque becomes correspondingly large as a result. **Suprathermal rotation** (Purcell 1979) suggests that the rotation of grains is not driven by stochastic collisions, but by emission of photons or H_2 from fixed locations on the grain, which would allow for much faster spinning. This would not decrease the alignment time scale – both the torque and the angular momentum increase directly with rotation – but the time limit for disalignment would come not from gas damping, but from the lifetime of emitting locations on the grains.

Radiative torques (RATs): proposed by Dolginov & Mytrophanov (1976), it started getting attention in the 1990s (*e.g.* Draine & Weingartner 1996, 1997). In this theory the angular momentum of the grains changes due to light scattering. A grain with defined helicity will have different scattering cross-sections for the right-hand and the left-hand circularly polarized components. If the radiation field is anisotropic, angular momentum is transferred to the grain, which will both spin-up and align the grains around its axis of precession: the magnetic field lines.An analytic description of this model is in Lazarian & Hoang (2007).

Amount of starlight polarization

Fig. 1.12 shows the relation observed between the polarization fraction in the V band, p_V, and the extinction A_V. Many different values of p_V are possible for each value of extinction, depending on the orientation of the magnetic field and the depolarization; however, there is a value for the "highest polarization possible" for each A_V, as indicated by the solid line – a linear function of A_V – that traces the envelope of the data cloud. This corresponds to the "ideal" polarization in the case where the Rayleigh reduction factor equals 1 and the magnetic field is uniform in the plane of the sky. It is the value that dust polarization models need to be able to reproduce. The value of "ideal" polarization is of $\sim 3\%$ per A_V magnitude ($\sim 9\%$ per E(B-V) magnitude).

Wavelength dependence of starlight polarization: the Serkowski curve

In lines of sight where starlight is polarized, the polarization fraction as a function of λ has a typical shape: it attains a maximum in the optical or near IR and declines on both sides of the peak, towards the UV and IR. Serkowski et al. (1975) found that the curve of the polarization fraction can be fitted, at optical wavelengths, with the following empirical formula:

$$p = p_\mathrm{max}\, e^{-K\, ln^2(\lambda/\lambda_\mathrm{max})} \tag{1.20}$$

where p_max is the maximum of the polarization fraction and λ_max is the wavelength at which the maximum occurs. The factor K was assumed to be constant and estimated equal to 1.15 by Serkowski et al. (1975) paper, but Wilking et al. (1980, 1982) found that not only it can vary, it is also linearly correlated with λ_max:

$$K = c_1\, \lambda_\mathrm{max} + c_2 \tag{1.21}$$

where the current best values for c_1 and c_2 are 1.66 ± 0.09 and 0.01 ± 0.05 respectively (Whittet 2003). Eq. 1.20 is called *Serkowski curve* when K is fixed to 1.15 and *Wilking curve* when K is a

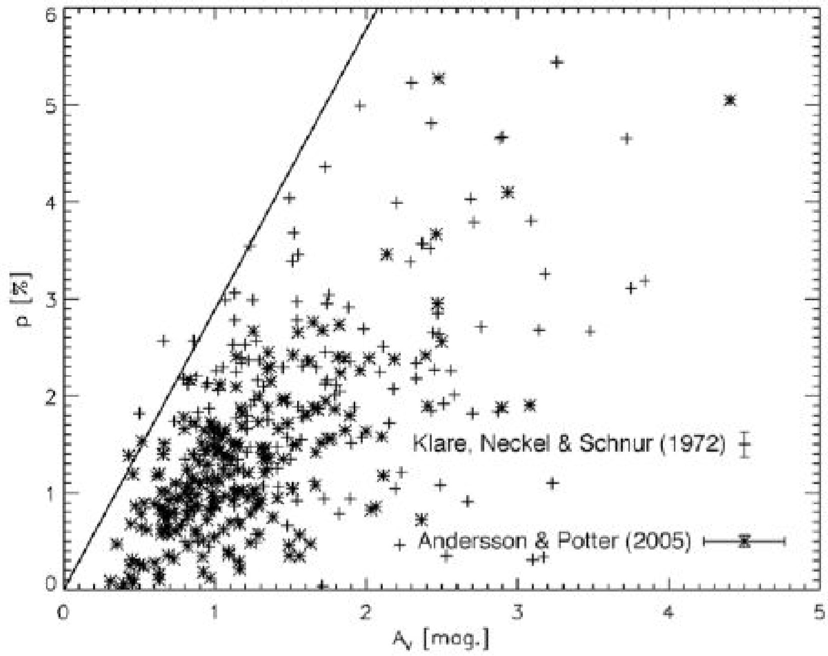

Fig. 1.12. The extinction-polarization relation is characterized by an upper envelope that corresponds to the maximum polarization efficiency, measured at $\sim 3\%$ per A_V magnitude. From Andersson et al. (2015) and refs. therein.

free parameter; while Eq. 1.21 is sometimes referred to as *Wilking law*. K parametrizes the width of the Wilking curve, or rather its narrowness, since the higher is K, the narrower is the peak.

The Serkowski/Wilking curve is only a good fit relatively close to the polarization peak, but it underestimates the actual polarization both in the UV and in the NIR for $\lambda \gtrsim 2\,\mu$m. A better fit for the polarization fraction at $\lambda \gtrsim 1\,\mu$m and up to $\sim 5\,\mu$m is a power law, $p(\lambda) \propto \lambda^{-\beta}$, with typical β values of 1.6 to 2 (Martin et al. 1992). This law is also purely empirical and it is just a simplification of the actual infrared polarization curve, but infrared polarization is notable in that it is uncorrelated to variations in the optical parameters, such as λ_max and K. The ultraviolet polarization curve also presents an excess compared to the extrapolated Serkowski/Wilkins curve, as shown by Martin et al. (1999).

The shape of the polarization curve offers a great wealth of informations about dust grains and their alignment. If all grains were aligned and had similar optical properties, for instance, we would expect the polarization curve and the extinction curve to have the same shape. This is indeed observed in the infrared, where both curves follow a power law with a spectral index of $1.5-2$: this suggests that big dust grains are well aligned and they have fairly homogeneous characteristics. On the other hand, in the UV the value of polarization decreases despite an increase in extinction. This means that small grains are not good polarizers: either they are spherical or the alignment process is only efficient for large grains. The bulk of polarization comes from big grains, as can also be shown in the following way: for a grain of size a and refraction index m, polarization is most efficient when $2\pi a|m-1| \sim \lambda$, as shown *e.g.* in Whittet (2003) for cylindrical particles. Thus, if polarization peaks at $\lambda_\mathrm{max} = 550$ nm, the typical aligned grain – assuming $m = 1.6$, typical of silicates at this wavelength – will measure about 150 nm. This argument underlines two other important notions: that λ_max depends on chemical composition as well as on size, and that the Serkowski polarization comes mainly from scattering, since it falls in the Mie region (Sect. 1.2.2). The dependence of λ_max

on the size of aligned grains, coupled with the positive correlation between K and $\lambda_{\max}$ (*i.e.* , the Wilkins curve narrows as $\lambda_{\max}$ increases), has been interpreted as evidence that regions with high $\lambda_{\max}$ have a narrower size distribution of aligned grains. This could mean that $\lambda_{\max}$ is high in these regions not because grains are larger in average, but because the size threshold for alignment is higher. Finding the actual relation between physical alignment and polarized observables is not trivial however, since, among other things, the $K - \lambda_{\max}$ relation should be corrected for artificial anticorrelations introduced by the fitting procedure. The relation between $\lambda_{\max}$ and the size of aligned grains will be further explored in Ch. 4

Polarized spectral features

The spectral features already discussed in Sect. 1.3.1 are sometimes polarized, which provides a great deal more information. The $9.7 - \mu$m feature of silicates, for instance, is polarized (Smith et al. 2000), which means that silicate grains are aligned. Likewise, the water and CO ice features are polarized (Whittet et al. 2001a; Hough et al. 2008), indicating that grains are aligned even in the depths of molecular clouds. On the other hand, the polarization of the $3.4\,\mu$m feature of aliphatic carbon is compatible with zero (Chiar et al. 2006), so the alignment status of carbonaceous grains is uncertain: since the 2175 Å bump nearly certainly comes from very small particles and is rarely seen polarized, the possibility that big grains of aromatic carbon are aligned has not yet been excluded (Hoang et al. 2013).

1.3.3 Dust models

A dust model specifies the composition, size distribution and morphology of one or more dust populations to explain the dust observables presented at the beginning of Sect. 1.3 (ideally all of them, in practice at least a part). It can also be used in reverse, to fit an observable or series of observables and recover the value of one or more free model parameters – for instance, the thermal emission of dust can be used to constrain both the dust mass and the ISRF intensity (more on this in Ch. 3).

No unique grain model exists, but most modern grain models share characteristics that, over the course of time, have been discovered to well reproduce observations. For instance, since Mathis et al. (1977) were able to fit the dust extinction curve from the UV to the NIR with a power-law size distribution, $dn/da \propto a^{-3.5}$, many models have big grains distributed as a power law with an exponent of $\sim 3 - 4$. This type of size distribution is called "Mathis-Rumpl-Nordsieck", or just MRN, after the authors of Mathis et al. (1977). From the point of view of optical properties, many models use the refractive indices given in the seminal work of Draine & Lee (1984) for graphite and "astronomical silicates", or "astrosilicates"– so called because they are derived from astronomical mid-infrared dust spectra and extrapolated to longer wavelengths, rather than being measured in the lab. Naturally, alternative materials do exist, as we will see in the rest of this section and in Ch. 2. When the discovery of mid-IR emission bands pointed to the existence of molecule-sized carbonaceous grains in the ISM (Sect. 1.3.1 and 1.4), PAH became a frequent component in dust models, such as that of Desert et al. (1990). A good portion of modern dust models thus follow the so-called "Silicate-Graphite-PAH" paradigm.

While a presentation of all modern dust models is not feasible, we will nonetheless describe in greater detail three dust models, representing rather different schools of thought, which we will use in our work in Ch. 2 and 3:

Draine & Li (2007), hereafter **DL07**, is emblematic of the astrosilicate-graphite-PAH model. It is one of the most popular dust models, often used to estimate dust and gas masses in Galactic and extragalactic environments by fitting dust emission (Draine et al. 2007; Aniano et al. 2012; Planck Collaboration Int. XXIX 2014). Its silicate grains use the optical properties from (Li & Draine

2001), which are an updated version of the (Draine & Lee 1984) silicates: the far infrared spectral index, originally extrapolated from mid-infrared astronomical observations, has been empirically adjusted to reproduce the FIRAS spectra of Finkbeiner et al. (1999)[15] and the recently measured WMAP point at 94 GHz. These optical properties pertain to silicates that are contaminated by other materials, including possibly a carbonaceous dust component. As to the population of carbonaceous grains, their optical properties are assumed to vary continuously from those of graphite for large sizes ($\gg 10^5$ C atoms) to those of PAHs for small sizes ($\lessapprox 10^5$ C atoms). The size distributions employed are those found by Weingartner & Draine (2001). This model also has a non-trivial description of the ISRF, which we will detail in Ch. 3.

Compiègne et al. (2011), hereafter **C11**, includes both astrosilicates (with the optical properties described in (Li & Draine 2001)) and PAHs, but its big carbon grains use optical properties of hydrogenated amorphous carbon (”BE” type), as derived from laboratory data by Zubko et al. (1996). The model is composed of several distinct populations: two “big grain” populations (power laws with exponential cutoffs at large sizes), one lognormally-distributed population of VSG, also with BE-type optical properties, and one lognormally-distributed population of PAHs. The separation of the carbon grains into three population does not reflect a physical constraint; it is a necessity dictated by modelling.

Jones et al. (2013), hereafter **J13** (also called THEMIS), is a core-mantle model with optical properties that are derived from laboratory measurements, both for silicates and carbon. It features a lognormal distribution population of big silicate grains, modelled as amorphous forsterite-like materials with iron inclusions and amorphous aromatic carbon mantles. Big carbon grains form a second lognormal distribution; they comprise aliphatic cores and aromatic mantles. A power law of small aromatic grains extends down to sub-nm sizes and takes the place of PAHs. The optical properties of the carbon used in J13 are those of the optEC$_{(s)}$(a) model, described in Jones (2012a,b,c) and in Ch. 2: the optEC$_{(s)}$(a) model is flexible enough to compute the optical properties over a wide range of grain sizes and carbon-to-hydrogen ratios (which reflect in the band gap of the material).

The DustEM tool

DustEM (`http://www.ias.u-psud.fr/DUSTEM/`) is a software written in Fortran 95, developed jointly by the IAS (Institut d’Astrophysique Spatiale) of Orsay and the IRAP (Institut de recherche en astrophysique et planétologie) of Toulouse for the purpose of modelling interstellar dust extinction and absorption. It takes a dust model made of an arbitrary number of grain types and reads as input tables of size- and wavelength-dependent characteristics of each grain type: the absorption and scattering coefficient $Q_{\rm abs}$ and $Q_{\rm sca}$, the heat capacity C and the average scattering angle cosine $g =< cos(\theta) >$, the latter being used only for models including radiation transfer. The outputs are the model’s total and polarized intensities, extinction and polarization cross-sections per H atom ($N_H = NI + 2N_{H_2}$) as a function of wavelength.

DUSTPROP is an IDL code that calculates the cross-section coefficients $Q_{\rm abs}$, $Q_{\rm sca}$, and $Q_{\rm pol}$, as well as the heating capacity C and the average scattering angle g for the grains given the grain geometry and its complex refractive index $m(\lambda) = n(\lambda) + ik(\lambda)$, which depends on its composition. Possible grain geometries include uniform spheres and spheroids (through the T-MATRIX code) and core-mantle spheres, but if greater flexibility in the choice of shapes is needed, there is the possibility to use the *Discrete Dipole Approximation* (DDA).

[15] The high-Galactic latitude Finkbeiner et al. (1999) spectra, extrapolated from *IRAS*, predicted a different SED than that subsequently observed by *Planck* (Planck Collaboration Int. XXIX 2014).

1.3.4 Observational evidence for dust evolution

We already know that the ISM, and dust with it, undergoes an evolutionary cycle (Sect. 1.1.4). The nature of this evolution has been revealed over time by observations.

Molecular clouds

It is now well established that dust in dense clouds is not the same as dust in the diffuse ISM. The spectroscopic analysis of dark clouds revealed the signatures of volatile molecules in the solid state, which indicates the formation of an ice mantle on dust grains (*e.g.* Whittet et al. 1983, 2001b; Hollenbach et al. 2009). The most famous spectroscopic signature is that of water ice at 3.0 μm, but many other substances have been identified, such as CO, CO_2, NH_3, H_2CO, N_2 and O_2. Ices are usually found in lines of sight with $A_V \gtrsim 3$ since, at lower extinctions, ice photodesorption is more efficient than formation (Tielens & Hagen 1982).

Another index of dust evolution is the "infrared color" I_{60}/I_{100}, *i.e.* the ratio of the flux at 60 μm over the flux at at 100 μm: I_{60}/I_{100} is lower in molecular clouds than in the diffuse ISM, meaning that very small grains in clouds either vanish or undergo a change in properties (Boulanger et al. 1990; Laureijs et al. 1991), which has been attributed to the formation of ice mantles (Laureijs et al. 1991; Boulanger et al. 1994).

Another clue came from dust temperature: the COBE FIR maps revealed that big grains are much colder in molecular clouds than in the diffuse ISM (Lagache et al. 1998), and the question arose of whether this resulted from the extinction of the ISRF in dense environment or from a change in the optical properties of dust. Subsequently, the comparison of submm observation from PRONAOS, IRAS and COBE with extinction maps obtained from star counts brought to the conclusion that ISRF extinction alone cannot explain the fall in temperature (Bernard et al. 1999; Stepnik et al. 2003; Planck Collaboration Early XXV 2011). Since the low temperatures in molecular clouds correlate with the areas of low 60/100 μm ratio, it was hypothesized that small grains and PAHs could coagulate on big grains in dense clouds: this would create fractal ("fluffy") aggregates, increasing the dust FIR opacity (Wright 1987; Köhler et al. 2011) and lowering its temperature.

Diffuse ISM

Unlike dark clouds, the diffuse ISM was considered a place where the dust properties would be relatively uniform: the lower density means that atoms are less likely to accrete on grains; also, the grains themselves rarely collide during their permanence in the diffuse ISM, so that shattering and coagulation is negligible.

This idea is gradually changing in the face of new evidence. The dust extinction curve shows variations (See Fig. 1.8, from Fitzpatrick & Massa 2007) that may result from differences in the grain size distribution or in the chemical composition (Cecchi-Pestellini et al. 2010 model the variations in the extinction curve that can be expected from the accretion of carbon over dust grains). Bot et al. (2009) measured the I_{60}/I_{100} and I_{160}/I_{100} colors in diffuse clouds (cirrus) at high Galactic latitude and found that their variations are anti-correlated, a result that is not completely reproduced by current models where only the ISRF intensity changes.

It is however with *Planck* that diffuse-ISM data become available for the whole sky at wavelengths sampling past the dust emission peak. Much more detailed analysis becomes then possible, and Planck Collaboration XI (2014) shows – with a full-sky modified black body fit on *Planck* and IRAS data – that the far infrared and submillimeter opacity of dust can change as much as a factor of ~ 2 and that its variation is anti-correlated with that in T, meaning that even in the diffuse ISM dust temperature depends – perhaps primarily – on dust opacity.

Planck Collaboration Int. XXIX (2014) also performs an all-sky fit on*Planck* and IRAS data, using the dust model by Draine & Li (2007). Compared to the A_V directly measured from extinction, the A_V predicted by the model – derived from the submillimeter opacity – is off by a factor that depends on dust temperature, again showing that dust opacity and temperature are correlated. A more detailed analysis will follow in Ch. 3.

Unlike for dense clouds, our understanding of dust variability in the diffuse ISM – its extent and its causes – is still in its infancy. To improve it, more studies will be needed in the far infrared and submillimeter domain; both unpolarized, as with the studies presented, and polarized, to study the evolution of grain shapes. One of the most powerful tools today for this kind of studies is the *Planck* mission.

1.4 Space observatories for the study of the ISM

The study of the ISM was revolutionised with the arrival of space observatories and other high-altitude instruments (such as stratospheric balloons), which allowed to observe the wavelength domains typical of dust emission – infrared, submillimetric and microwave – free from atmospheric interference. We present here a brief historical panorama of the observatories and instruments which allowed us to observe the ISM, leading to *Planck*. It is of note that many of these observatories were built for cosmological studies of the CMB; however, they need to measure the foregrounds to the CMB – which include dust and other ISM emission – in order to subtract them; for this reason, cosmological instruments are also powerful instrument for Galactic physics.

IRAS

The *InfraRed Astronomical Satellite*, active in 1983, mapped the sky in four infrared bands at 12, 25, 60 and 100 μm, with an angular resolution of 4'; it was optimized for the detection of point sources. IRAS led to major advances in all astronomical fields concerned with infrared observations: the number of extragalactic sources observed in the 10-to-100 μm range was increased from a few dozens to 20 000 allowing their systematic study, it detected the first protostars and the first dust shells around other stars (Soifer et al. 1987; Beichman 1987). In the study of the ISM, its major contributions were the discovery of structures at all Galactic latitudes in the dust emission maps – the so-called "infrared cirrus" – and the discovery that dust thermal emission is ubiquitous even at short wavelengths (12 and 25 μm), leading to the inclusions of VSGs and PAHs in dust models (see Sect. 1.2.3, "Stochastically heated grains").

COBE

The *COsmic Background Explorer* is a satellite launched in 1989 to study the Cosmic Microwave Background (CMB). It definitively proved that the CMB is a black body with $T \sim 2.7$ K and it measured for the first time the anisotropies in its temperature – of the order of 10^{-5} on an angular scale of 7° – opening a new era for cosmology (Smoot et al. 1992; Boggess et al. 1992). Galactic astrophysics also benefited from the satellite, thanks to two instruments in particular: the Diffuse Infrared Background Experiment (DIRBE) and the Far Infrared Absolute Spectrophotometer (FIRAS).

DIRBE measured the spectrum of the sky over 10 bands covering $\lambda = 1$ to $300\,\mu$m, with an angular resolution of 0°.7. Its precise calibration but low resolution make it complementary to *IRAS*. Schlegel et al. (1998) combined IRAS maps with the 100 and 240 μm DIRBE data to produce the widely used SFD map of dust emission at 100 μm, with DIRBE-like sensitivity and IRAS-like resolution.

Instrument	LFI			HFI					
Center ν (GHz)	30	44	70	100	143	217	353	545	857
Center λ (μm)	10 000	6 820	4 280	3 000	2 100	1 380	850	550	350
Polarized?	Yes	Yes	Yes	Yes	Yes	Yes	Yes	No	No
FWHM (arcmin)	33	28	13	9.4	7.0	4.7	4.4	3.8	3.7

Table 1.3. The characteristics of the *Planck* instruments, as per Planck Collaboration Early I (2011).

FIRAS produced spectra of the whole sky between $\lambda = 100\,\mu$m and 1 cm, with a resolution of 7°, which provided the main map of Galactic dust emission for a long time.

Archeops

The stratospheric balloon *Archeops* made three successful flights between 1999 and 2002, carrying a prototype of the *Planck* HFI instrument. This measured the sky in intensity in four bands centered at 143, 217, 353 and 545 GHz. The 353 GHz band also measured the sky in polarization. Archeops produced important science results both as temperature maps – filling the gap between the large scale anisotropies found by COBE and the small scale anisotropies found in previous observations (Benoît et al. 2003) – and as polarization maps – providing the first large-coverage map of Galactic (dust) polarized emission (Benoît et al. 2004).

WMAP

The *Wilkinson Microwave Anisotropy Probe* is the satellite that succeeded COBE and was launched by NASA in 2001. It effected the first full-sky measurement of polarization, in five bands between 23.5 and 94 GHz and with angular resolutions between 13' and 50', the best until *Planck*. It allowed the first reconstruction of the power spectrum of (anisotropies of) the polarized CMB (Jarosik et al. 2011 and refs. therein).

Planck

Planck is a space observatory placed in the L_2 Lagrange point of the Earth-Sun system, 1.5 million km from Earth. Active between 2009 and 2013, its purpose was to study the cosmic microwave background (CMB) with unprecedented sensitivity and angular resolution (Tauber et al. 2010; Planck Collaboration Early I 2011). The new data thus obtained on the polarization and the angular power spectrum of the CMB anisotropies allowed to better constrain the cosmological models.

The *Planck* observatory consisted of two instruments, with characteristics resumed in Tab. 1.3. The Low Frequency Instrument (LFI) is a set of radiometers cooled to 20 K to scan the sky in three bands, centered around frequencies of 30, 44 and 70 GHz (10, 6.8 and 4.3 mm respectively). The High Frequency Instrument (HFI) is composed of 52 bolometers, 20 of which (the “spider-web bolometers”) are sensitive to intensity alone, while the remaining 32 (the “polarization-sensitive bolometers”) are arranged in orthogonally-oriented pairs to detect polarization. The HFI bolometers are cooled to 0.1 K and observe in bands spanning between 100 GHz and 857 GHz (λ between 3 mm and 350 μm); for frequencies up to 353 GHz ($\lambda \geq 850\,\mu$m) polarization is also measured.

The use of two different instruments and many bands allows to correct for the systematics of each instrument on its own, and to characterise and reconstruct the wavelength-dependent foregrounds to the CMB: the synchrotron emission, free-free emission and the anomalous microwave emission that fall in the frequency domain of LFI, as well as the thermal dust emission in the HFI domain.

The *Planck* HFI instrument provided full-sky maps of the three Stokes parameters for linear polarization, I, Q and U, as well as their correlations II, IQ, IU, QQ, QU and UU(Planck Collaboration VIII 2015). They are pixelized according to the HEALPix scheme with $N = 2048$ (Górski et al. 2005), so that each pixel has a side of approximately 1'.7, or about a third of the minimum *Planck* beam size – as much as is needed to avoid image degradation according to Nyquist's theorem.

Chapter 2

Dust photoprocessing: the Jones et al. 2013 model

Contents

2.1 Context

As presented in Ch. 1, Sect. 1.3.4, results from the latest generation of surveys in the microwave and sub-mm domain (*Planck*, *Herschel*) suggest that the optical properties of dust in the diffuse ISM are not fixed, but change from region to region and, within regions, from the outside to the inside of structures. Interstellar dust models need to explain this variability, which is likely due to dust evolution.

During the first year of thesis I concentrated on a class of materials that are very interesting in the perspective of explaining dust variability: the hydrogenated amorphous carbons collectively known as a-C(:H) (Robertson 1986; Jones 2012a,b,c). The optical properties of these materials can be modified by UV photoprocessing, so that the dust properties will vary with the environmental conditions and previous dust history. We worked on a few models containing a-C(:H), looking for physical parameters that could reproduce the variations of dust emission observed by *Planck*. In particular, we explored the effects of varying the amount of a-C(:H) photoprocessing and of carbon accretion on grains from the gas phase. This work, presented here for completeness, did not lead to any published article[1] as it was not conclusive; however, the same work helped calibrate the Jones et al. (2013) model and include it in the DustEM tool; the exploration of the (non-trivial) interplay of carbon photoprocessing and accretion also aided in the application of J13 to dust evolution scenarios (Jones et al. 2014).

2.2 *Planck* Collaboration XI: all-sky modified black body fit

It will be useful, before describing my own work on the subject of dust evolution, to present other results obtained by the *Planck* collaboration, which constitutes the basis for my analysis. The present section will therefore be devoted to the results of the *Planck* sub-mm survey on dust evolution, and in particular to the modified black body fit of Planck Collaboration XI (2014).

Dust emission in the sub-mm domain, which comes from big grains in thermal equilibrium, is empirically well-fit by a modified black body (Planck Collaboration Early XXIV 2011; Planck Collaboration XI 2014). Maps of the dust T, β and τ_0 are therefore available for the full sky (see Ch. 1, Sect. 1.2.3 and in particular Eq. 1.10).

The analysis in Planck Collaboration XI (2014) concentrates on wavelengths of 100 μm and longer, where emission is dominated by dust grains in thermal equilibrium. The paper fits the *IRAS* band at 100 μm and the *Planck* bands at 350, 550, and 850 μm. The limitation of having only four bands in observation also precludes the possibility of using more sophisticated models, but the fit is empirically good.

Since the dust and gas are well mixed in the ISM (*e.g.*, Bohlin et al. 1978) the hydrogen column density $N_{\rm H}$ is used in this case as a proxy for dust abundance. The atomic hydrogen column density, $N_{\rm H_I}$, is retrieved using the LAB data on 21-cm emission (Kalberla & Haud 2015). The *Planck* ^{12}CO $J = 1 \rightarrow 0$ emission map provides a first-order estimate of the amount of molecular hydrogen[2]. This gives the following estimate for the total hydrogen column density:

$$N_{\rm H} = N_{\rm H_I} + 2\, W_{\rm CO}\, X_{\rm CO} \tag{2.1}$$

where $W_{\rm CO}$ is the CO flux measured in K km s^{-1} and the conversion parameter $X_{\rm CO}$ is not constant,

[1]The content of the present chapter was presented in poster format at the conference *The Life Cycle of Dust in the Universe*, Taipei, 18-22 November 2013 (See Appendix B and Fanciullo et al. 2013).

[2] Several emission lines of CO – including the $J = 1 \rightarrow 0$ 2.6-mm line – fall within the *Planck* bands, giving a significant contribution to the 100, 217 and 353 GHz maps. Several component separation methods have been devised to estimate CO contamination in the *Planck* bands and, as a consequence, construct maps of CO emission at the same wavelengths (Planck Collaboration XIII 2014).

but it has a typical value of $2 \cdot 10^{20}\,\mathrm{H_2\,cm^{-2}\,K^{-1}\,km^{-1}\,s}$ (Bolatto et al. 2013). This estimate does not take into account the "dark gas" not associated with CO nor the WIM, for lack of a proper template (Planck Collaboration Early XIX 2011; Planck Collaboration XI 2014).

Dust radiance

An important concept introduced in Planck Collaboration XI (2014) is that of *radiance*, the total power emitted by dust grains in thermal equilibrium $\mathcal{R} = \int_\lambda I_{\lambda,\mathrm{BG}}$. This, through the conservation of energy, also corresponds to the power absorbed by grains in thermal equilibrium. If one assumes that the emission of big grains follows a modified blackbody, the integration over wavelength yields the following formula for radiance (Planck Collaboration XI 2014):

$$\mathcal{R} = \tau_0 \frac{\sigma_s}{\pi} T^4 \left(\frac{kT}{h\nu_0}\right)^\beta \frac{\Gamma(4+\beta)\zeta(4+\beta)}{\Gamma(4)\zeta(4)} \,. \tag{2.2}$$

The functions Γ and ζ are the Gamma and Riemann zeta function, respectively, and σ_s the Stefan-Boltzmann constant. The reference wavelength chosen for τ_0 is $\lambda_0 = 850\,\mu\mathrm{m}$ (see Ch. 1, Sect. 1.2.3), corresponding to the central wavelength of the 353 GHz *Planck* band. The radiance is a very useful and powerful tool. Firstly, it is a very robust parameter, without the problems of noise-caused correlations or bias that affect T, β or τ_0 alone and that were described *e.g.* by Shetty et al. (2009b,a). Also, even if it is measured in the submillimeter, $\mathcal{R}$ is independent of the dust submillimeter optical properties. This counterintuitive fact is a direct consequence of the conservation of energy: since the power emitted is the power that has been absorbed, it is completely determined by the ISRF and the optical properties of big grains in absorption, mainly in the UV-to-NIR wavelength range. The optical properties in the far infrared to millimeter range modulate the shape of the SED, but not its total value integrated on λ. This means that $\mathcal{R}$ can be considered a "heating power" for big grains, integrating the effect of the dust absorption (or, to use observable quantities, the dust extinction curve and the albedo), as well as the ISRF intensity.

Variable dust optical properties

The use of the far infrared dust opacity as a tracer of gas column density (*e.g.*, Schlegel et al. 1998) implicitly assumes that the dust specific opacity is constant. One of the purposes of Planck Collaboration XI (2014) is to test the validity of this assumption: the result is that, as shown in the top of Fig. 2.1, even in the diffuse ISM (defined in the paper as the lines of sight where $N_{\mathrm{H_I}} < 2.5 \times 10^{20}\,\mathrm{cm^{-2}}$) the ratio τ_0/N_H is not constant. Its anti-correlation with T shows it is a biased tracer of gas density. On the other hand, the middle of Fig. 2.1 shows that $\mathcal{R}/N_\mathrm{H}$ is remarkably independent of T, meaning it may be a better N_H tracer.

The data resumed in Fig. 2.1 are not important just for calibration: they give useful insights on the physical properties of the ISM medium, since they provide a strong argument against dust with uniform submillimeter opacity in the diffuse ISM. If we assume the following:

- N_H as defined in Eq. 2.1 is a reliable tracer of dust column density;
- τ_0 can be used, as a first order approximation, as a tracer of overall submillimeter dust opacity, even though it does not match exactly the opacity of any individual dust population; and
- The shape of the ISRF spectrum does not present important variations in the diffuse ISM;

then the top of Fig. 2.1 shows clearly that, between temperature extremes, the grains' opacity varies by a factor ~ 2 and only dust with low opacity can reach high temperatures (> 22 K). At the same time, the near-constancy of $\mathcal{R}/N_\mathrm{H}$ suggests that the intensity of ISRF is independent of N_H, and

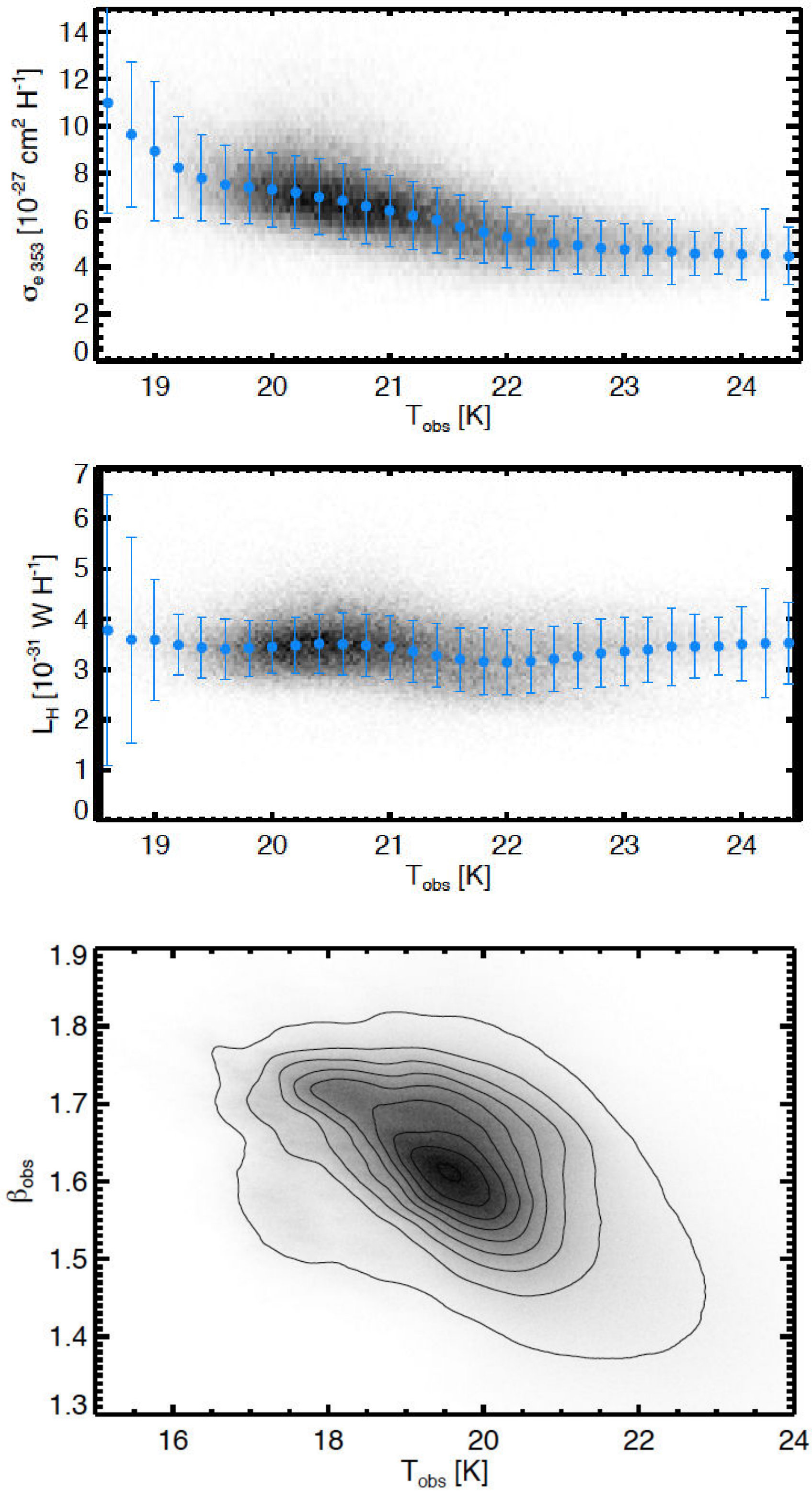

Fig. 2.1. Correlations between modified blackbody parameters as discovered by Planck Collaboration XI (2014). From top to bottom: $\tau_0/N_{\rm H}$ vs. T and $\mathcal{R}/N_{\rm H}$ vs. T in the diffuse ISM ($1 \times 10^{20}\,{\rm cm}^{-2} < N_{\rm H_I} < 2.5 \times 10^{20}\,{\rm cm}^{-2}$); β vs. T over all the sky.

therefore is not responsible for the observed variations of T with N_{H}. While it could be argued that $\mathcal{R}/N_{\mathrm{H}}$ depends on the albedo as well as the radiation intensity, and so does not necessarily trace the ISRF, one would need albedo to be anti-correlated with radiation field to reproduce the results shown. Also, grains that emit the same power but have different temperatures – as is observed in the middle of Fig. 2.1 – must have different submillimeter opacities. The conclusion of Planck Collaboration XI (2014) is that in the diffuse ISM dust submillimeter opacity is an important factor in explaining the non-uniformity of dust temperature, while no evidence was found that ISRF intensity plays a greater or comparable role.

2.3 Carbon evolution in models

We set out to explain the correlations found by Planck Collaboration XI (2014) in the diffuse ISM and shown in Fig. 2.1, which are indicators of dust evolution:

- Dust temperature and spectral index β are negatively correlated;
- Dust temperature and submillimeter opacity τ_0/N_{H} are negatively correlated;
- The total power emitted per unit of gas mass, $\mathcal{R}/N_{\mathrm{H}}$, is roughly independent of dust T;

as well as to reproduce the observed range for the model parameters. Some candidate materials for carbonaceous dust components, the so-called *hydrogenated amorphous carbons*, are known for being very susceptible to alterations in the ISM, due to processes such as photodissociation, thermal annealing, hydrogenation, gas-phase accretion and shattering (*e.g.*, Jones et al. 1990; Mennella et al. 2001; Bocchio et al. 2014). Recently, a model has been proposed (Jones 2012a,b,c) that allows to simulate the effects of such alterations, and includes naturally the possibility of simulating the chemical evolution of dust.

2.3.1 The optEC$_{(\mathrm{s})}$ a-C(:H) model

The family of hydrogenated amorphous carbon materials is composed of aromatic (hydrogen-poor) ring domains linked by aliphatic and olefinic (hydrogen-rich) bridges. These materials cover a wide range of aromatic-to-aliphatic (or, alternatively, carbon-to-hydrogen) abundance ratios, as we explain in more detail in Appendix A. Materials that are mostly aromatic are called a-C, while mostly-aliphatic materials are a-C:H. The symbol for all hydrogenated amorphous carbons, independent of carbon to hydrogen ratio, is a-C(:H). The optical and thermal properties of a-C(:H) depend of course on its composition, determined primarily by the carbon-to-hydrogen abundance ratio. What makes a-C(:H) so interesting as a candidate dust material is that heat and UV photons can break its C–H bonds, causing the grain mantle to become more aromatic. This means that a-C(:H) grains photoprocessed in the diffuse ISM will evolve: dust in different regions – with different processing histories – would have different properties and SEDs (Figs. 2.2 and 2.3). Since the processing of grains is short compared to their time spent in the diffuse ISM, the outer ~ 20 nm of a-C(:H) grains would be a-C, as well as the entire volume of grains smaller than ~ 20 nm (Jones 2012b).

The use of a-C(:H) in dust models has however been limited by the comparative lack of experimental data: refractive indices have been measured in the lab for only a small and sparse sample of this vast family of materials (Jones 2012b). As a temporary remedy until more complete experimental data are available, a model of a-C(:H) optical properties was created by Jones, which includes the laboratory data known of at the time of publication and calibrated on them to create a coherent picture for all hydrogenated amorphous carbon (Jones 2012a,b,c). This model is called *optical properties prediction tool for the Evolution of Carbonaceous solids*, or optEC$_{(\mathrm{s})}$. The characteristics of the different types of a-C(:H) within the optEC$_{(\mathrm{s})}$ model are as follows:

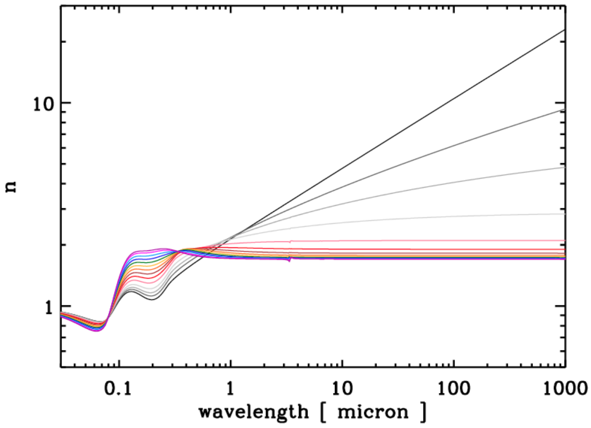

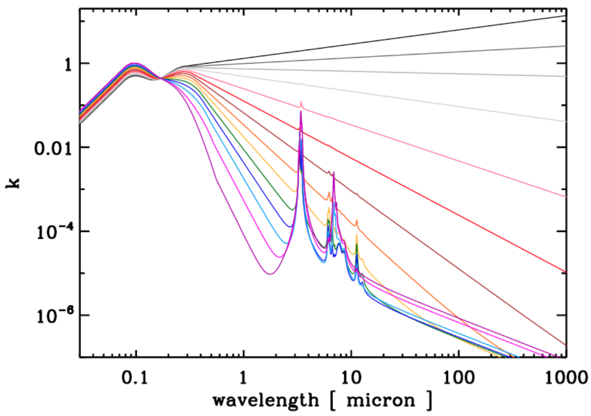

Fig. 2.2. Real (left) and imaginary (right) part of the refractive index for optEC$_{(s)}$ materials as a function of the wavelength, for various bandgaps E_g. Color coded according to Tab. 2.1. From Jones (2012b).

Composition effects: The optical properties of the bulk material are completely determined by the abundance of hydrogen atoms, which in most cases is proportional to the material's Tauc band gap E_g (Jones 2012a,b), though the proportionality fails for values of E_g close or inferior to 0. Typical values of the Tauc band gap are ~ 0.1 eV for a-C and $\gtrsim 1$ eV for a-C(:H), with a maximum of ~ 2.6 eV. From Fig. 2.2, we see two main differences between mainly-aromatic and mainly-aliphatic materials: firstly, a-C has a much higher opacity than a-C:H in the far infrared and submillimeter range, since it has larger aromatic (and well-conductive) domains; secondly, the shape of the infrared bands between ~ 3 and $\sim 15\,\mu$m changes, since different H abundances reflect in different relative abundances of the various C–H bond types.

Size effects: For very small grains the optical properties of a-C(:H) depend on the grain size as well as the properties of the bulk material. Very small grains show enhanced infrared bands and, in the case of a-C, lower submillimeter continua, closer to those of a-C:H. The band enhancement comes from the larger surface-to-volume ratio of small grains, which increases the relative weight of surface grain hydrogenation and the presence of C–H bonds. The level of the continuum is determined by the size of aromatic cluster domains: in bulk a-C these can measure several nm (Jones 2012c), so that grains with low E_g and radii of $\lesssim 1$ nm have smaller aromatic clusters than the bulk material, which makes them more "aliphatic-like". An empirical rule is that cluster size effects become important for radii $a \leq (E_g + 0.2)^{-1}$, where a is in nm and E_g in eV (Jones 2012c). A version of optEC$_{(s)}$ that accounts for size effects exists, and is called optEC$_{(s)}$(a).

Dust evolution: The processing that a-C(:H) materials undergo in the ISM leads to their evolution: they can lose hydrogen through UV irradiation (photo-darkening) and thermal processes (annealing), or they can be hydrogenated by incorporating impacting H atoms, depending on the relative efficiency of the two processes in the local environment (Mennella et al. 2001; Alata et al. 2014; Jones et al. 2014). Also, hydrocarbons are easily eroded (Serra Díaz-Cano & Jones 2008; Bocchio et al. 2014; silicates are more resilient), but they can also be (re-)accreted from gas phase C and H atoms. The structure and composition of grains can therefore vary from region to region: a strength of the optEC$_{(s)}$(a) model is that it naturally accounts for different carbon chemical compositions and size effects.

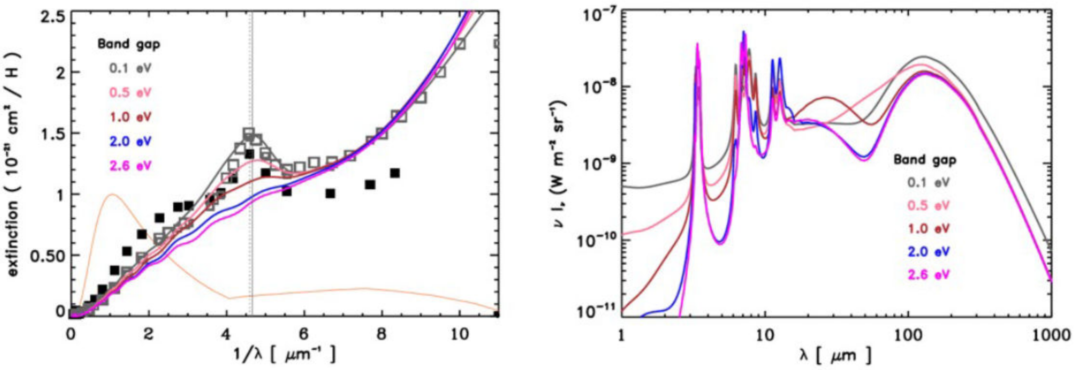

Fig. 2.3. Variation of dust extinction curve and SED, using the Jones et al. Jones et al. (2013) dust model, for different types of a-C(:H). In all models the band gap of the aliphatic carbon is 2.5 eV, while that of the aromatic component varies. Only the models with an a-C band gap of ~ 0.1 eV are physically plausible; the other ones are for illustrational purposes only. From Jones et al. (2013).

E_g [eV]	$X_{\rm H}$	Color
-0.1	0.00	black
0.0	0.00	dark gray
0.1	0.02	mid gray
0.25	0.05	light gray
0.5	0.11	pink
0.75	0.17	red
1.0	0.23	brown
1.25	0.29	orange
1.5	0.35	yellow
1.75	0.41	green
2.0	0.47	blue
2.25	0.52	cobalt
2.5	0.58	violet
2.67	0.62	purple

Table 2.1. The color code for the Tauc band gap E_g and the hydrogen abundance by number $X_{\rm H}$ in the plots, from Jones (2012a,b,c).

2.3.2 Dust models using optEC$_{\rm (s)}$

To this purpose, we explore the effects of two different phenomena – aromatization by photoprocessing and accretion of carbonaceous materials from the gas phase – using two different dust models.

The Jones et al. (J13) dust model

This model has already been introduced in Ch. 1, Sect. 1.3.3, so we will just remind its main characteristics. In this model the grains are spherical and divided into two populations (Fig. 2.4):

- Silicate grains (amorphous forsterite-type material) with iron inclusions and an outer a-C mantle. These have a lognormal size distribution, centred in mass around 160 nm.

- a-C(:H) grains, with an a-C:H core/a-C mantle structure if their radii are > 20 nm, and are uniformly made of a-C if smaller. The size distribution is the sum of a lognormal centred in mass around 140 nm and a power law that extends down to 0.4 nm.

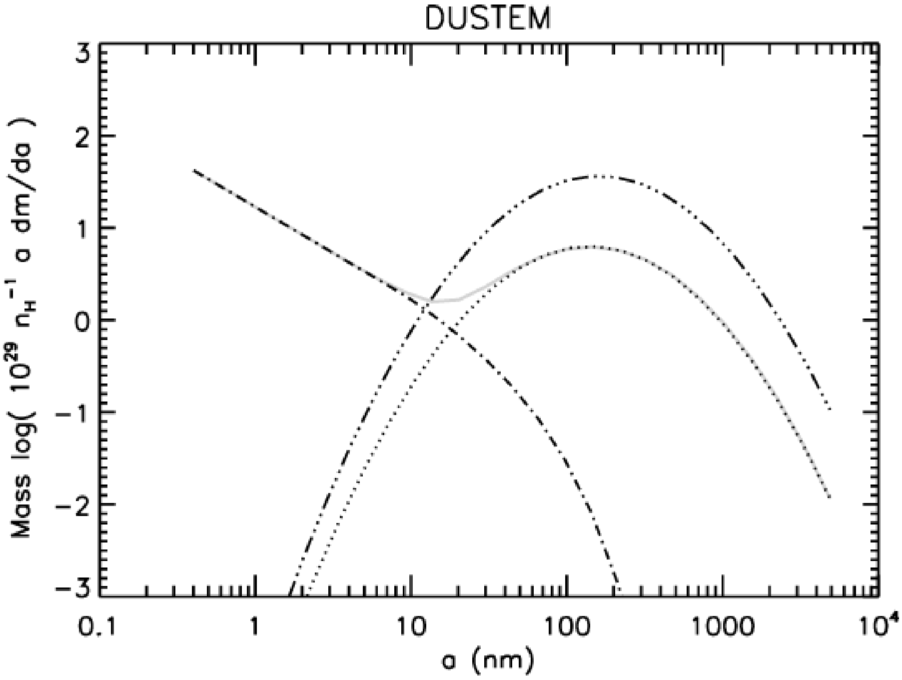

Fig. 2.4. Size distribution for the grain populations in Jones et al. (2013). The dotted and slash-dotted lines are the two a-C(:H) population components; the solid grey line shows the combined distribution. The slash-triple-dotted line is the mantled silicate grain population. From Jones et al. (2013).

The model contains no PAHs: the emission features usually attributed to PAHs come from the three-dimensional, sub-nm-size a-C grains. In this model, E_g is 2.5 eV for a-C:H and 0.1 eV for a-C; the mantles on the silicate grains are 5 nm thick. An important feature of this model is that emission in the far infrared and submillimeter is dominated by the mantled silicates; only at wavelengths $\gtrsim 1$ mm the emission from big carbon grains becomes comparable (Jones et al. 2013).

In the following we explore how the predicted SED changes when we vary the E_g of a-C (to simulate varying amount of photoprocessing) and the thickness of mantles on silicates (to simulate varying degrees of accretion).

The hybrid dust model

The J13 model is both novel and rather complex, which adds difficulty to the study of dust evolution: it is hard to disentangle the effects of a-C(:H) evolution from the effects of other characteristics, such as the new chemical composition of silicates and the presence of core-mantle grains. The dependence of a-C(:H) properties on size is particularly important: size effects become important around 3-5 nm for $E_g \sim 0.1$ eV, which is just the thickness and band gap of the a-C mantles on silicates. In the J13 model the effects of accretion and band gap variation cannot be studied separately.

For these reasons we decided to have a control model which makes use of optEC$_{(s)}$(a) while remaining as close as possible to a preexisting model. What we call the *hybrid model* is the same as the C11 model described in Ch. 1, Sect. 1.3.3, with the exception that the Zubko et al. (1996) amorphous carbon grains are replaced by core-mantle optEC$_{(s)}$(a) grains like those of the J13 model. The astrosilicate grains and the PAHs, as well as the size distribution and abundance for each grain type, are unchanged. In the hybrid model, like in C11, the emission from carbon grains is at least as strong as that from silicates, and stronger at "short" ($\lesssim 100\,\mu$m) wavelengths.

2.4 Dust evolution

2.4.1 Mantle thickness and bandgap effects

The modifications to the J13 and hybrid models to simulate dust evolution were as follows:

- The E_g of the a-C material was varied between 0.1 and 0.3 eV, to simulate the effects of different aromatization/hydrogenation efficiencies. We did not change the E_g of the a-C:H material – 2.5 eV – since it has very little effect.

- For the hybrid model, we changed the thickness of the a-C mantle of carbon BGs, to simulate the erosion and accretion of aromatic carbon. Since this turned out to have little effect on dust emission (see below), we decided not to do the same for the J13 model, to keep the numbers of variables at a minimum.

- For the J13 model, we varied the thickness of the carbon mantle on silicates between zero (naked silicates) and 10 nm, to simulate the erosion and accretion of aromatic carbon. This required to carefully calculate the effects of removing and adding carbon on the total mass of the silicate grains.

The results of the simulated dust evolution are shown in Fig. 2.5. We start with the hybrid model, which is easier to interpret since it has no carbonaceous mantles thinner than 10 nm and its big grain emission presents no cluster size effects.

Results for the hybrid model (Fig. 2.5, right column) Variations of observables with the thickness of a-C mantles on carbon grains (spanning colors from violet to red) is modest, so we concentrate on the main parameter : E_g. The observed $T - \tau_0$ anticorrelation is reproduced by variations of E_g: higher E_g values correspond to lower submillimeter opacity and therefore to higher temperatures. The ISRF absorption – and therefore radiance – is essentially constant, again as observed. However, the β_{obs} of the model follows that of the optEC$_{(s)}$ materials in that it increases with E_g, thus producing a $T - \beta$ correlation that is opposite to the one observed. Another issue is the very low value for β (centered on 1.35), due on one hand to the low β of the a-C(:H) and on the other hand to the presence of two dust population – carbon and silicates – with different temperatures which tends to lower the fitted value of β and increase that of T (*e.g.*, Shetty et al. 2009b). This is also likely the origin of the relatively high T, centered around 21-22 K as opposed to the ~ 20 K found by Planck Collaboration XI (2014).

Results for the J13 model (Fig. 2.5, left column) In the case of J13, one can easily see that adding carbon mantles (symbols) on the silicate grains increases the dust temperature due to increased ISRF absorption. Other results, however, require more complex explanations. The submillimeter opacity increases with the mantle thickness, meaning that the model predicts the opposite $T - \tau_0$ relation of the one observed. For the highest E_g, the increase of τ_0 with the mantle thickness is due to the higher mass of dust; for the lowest E_g the effects becomes more marked, since aromatic clusters get large enough to increase the opacity of a-C. We can see that β_{obs} in the J13 model is highly dependent of band gap, even in the case of bare silicates. This is a consequence of carbon emission shifting to longer wavelengths for lower E_g (*i.e.* colder carbon grains): the SED increases in the carbon-dominated millimeter range and remains the same in the silicate-dominated submillimeter and far infrared, flattening the SED. The effect is more marked for thick-mantled grains, where the carbon component in “silicates” is important enough to influence the spectral index, and aromatic clusters have space to grow. The overall effect is to create a shallow anticorrelation between β and T, which is consistent with the observations. Finally, we observe that

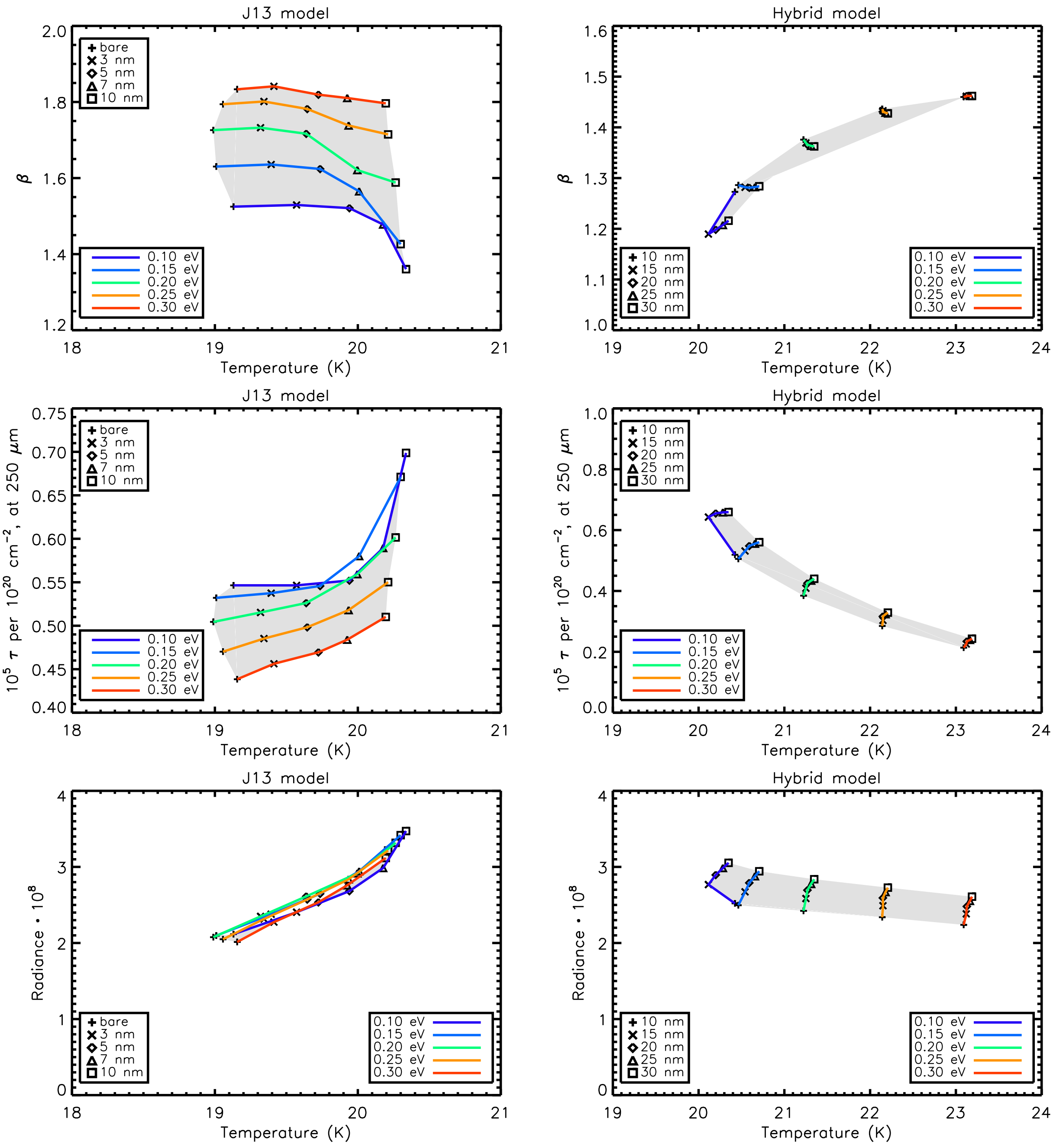

Fig. 2.5. Simulated dust observations for the modified J13 (left column) and the hybrid models (right column), plus dust evolution (see text). Top row: β as a function of T. Middle row: τ_0 as a function of T. Bottom row: dust radiance $\mathcal{R}$ as a function of T. The combination of bang gap variability and a-C accretion clearly cannot reproduce the trends revealed by *Planck* (Fig. 2.1).

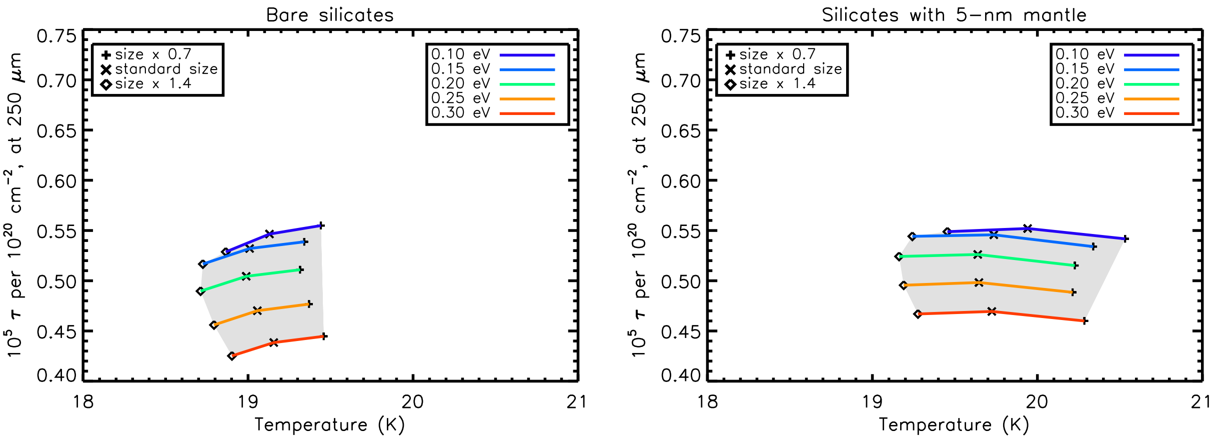

Fig. 2.6. Simulated T and τ_0 for modified Jones models with altered size distribution (see text). Left: bare silicate grains and a population of large a-C:H/a-C grains; right: the same plus 5-nm a-C mantles on silicates. Changing the size distribution also cannot reproduce the tendencies shown in Fig. 2.1.

radiance is strongly correlated with mantle thickness and weakly with E_g, meaning that it depends on the optical properties in absorption. This creates a strong correlation between temperature and radiance which is not observed.

All these results can be interpreted as the interplay of a few simple behaviours:

- Carbonaceous materials absorb the ISRF better than silicates;
- The more aromatic carbons have lower β and higher sub-mm opacity;
- Aromatic carbon assumes aliphatic-like properties when limited in size ($\lesssim$ 5 nm).

2.4.2 Size effects

We already know from the variation of the extinction curve that the size distribution of dust is likely to vary (Ch. 1, Sect. 1.3.1), so an analysis of dust evolution would not be complete without studying the effects of variations in the size distribution. For this reason we explored the $T - \tau_0$ relation for the J13 in the case of different average grain sizes: in Fig. 2.6 we see the T and τ_0 of J13 models where the centers of both lognormal size distributions (silicates and carbon) have been multiplied by 0.7 and 1.4 respectively. As before, separating the effects of size and carbon optical properties in J13 is very difficult: if we decrease (increase) the average silicate grain size while keeping the same a-C coat thickness, we increase (decrease) the carbon-to-silicate ratio and the grain absorption, thus increasing (decreasing) the temperature beyond the effect of mere size. At the same time, maintaining a constant carbon-to-silicate ratio would mean to change the mantle thickness on silicates, altering the optical properties of a-C. In the end we decided to compare the size effects both in the case of mantled silicates and in an alternative J13 model with no mantles. As we see in Fig. 2.6, grain size has no relevant effect on τ_0 and a very mild effect on T. The effect on temperature is more marked when a-C mantles are present, as expected. In neither case the observed $T - \tau_0$ relation is correctly reproduced.

2.5 Conclusions

The effects of photo processing, gas-phase accretion and variations in size distribution in the diffuse ISM cannot consistently reproduce all of the observed trends in the frame of the J13 and hybrid models. Furthermore, results are extremely model-dependent: the two models used give complementary results, with J13 only reproducing the $\beta_{\rm obs}$ and $T_{\rm obs}$ ranges and the $T-\beta$ anticorrelation, and the hybrid model only reproducing the $T-\tau_0$ and $T-\mathcal{R}$ relation. These results were published in Fanciullo et al. (2013), and were the subject of a poster – reproduced in Appendix B – presented during the *The Life Cycle of Dust in the Universe* conference in Taiwan (2013).

The high model-dependence of our results shows that one cannot study the effects of a single phenomenon – such as accretion or photoprocessing – without specifying the whole dust model where one intends to apply it. For this reason we decided, in the rest of the thesis, to follow a new direction of work: instead of trying physical processes directly, we use the observations to quantify the change in dust optical properties, for future use as a guideline to obtaining a better idea of the possibly relevant processes. Our results in this enterprise are in Ch. 3.

We mention a later article, Ysard et al. (2015), which does a similar but more complete analysis. It uses an updated version of the J13 model[3] and varies a much larger set of parameters over a physically-realsitic range: a-C mantle thickness over both carbon and silicate grains, chemical composition of the nano-size inclusions, relative abundance of the different grain populations, size distribution and ISRF intensity. Ysard et al. (2015) showed that it is possible to reproduce most of the *Planck* observations presented in Planck Collaboration XI (2014), but the set of parameters needed is much larger and involves nearly all of the aspects of dust modelling.

[3]The changes in the model, detailed in Köhler et al. (2014), include the chemical composition of amorphous silicates – now a mixture of 50% olivine-like and 50% pyroxene-like materials – and that of inclusions, which are now a mixture of iron and FeS. These changes affect mostly the silicate extinction bands at 10 and 18 μm, so the results in this thesis are not affected by our using the original version of the model.

Part II

Dust evolution in the diffuse ISM

Chapter 3

Can models reproduce the variations of the dust SED in the diffuse ISM?

Contents

3.1 Context and motivation

In Ch. 1, Sect. 1.3.4 we summarized the current knowledge about dust evolution: while the evolution of grains in dark clouds – aggregation and accretion of mantles from the gas phase – has been studied for several decades now, the variations of the properties of dust in the diffuse ISM have a much shorter story, and the *Planck* submillimeter survey provided perhaps the greatest advances in this field so far. Two *Planck* papers in particular, Planck Collaboration XI (2014) and Planck Collaboration Int. XXIX (2014), made all-sky diffuse-ISM tests of existing dust models and showed the limits of current dust modelling. A brief outline of both was given in Ch. 1, Sect. 1.3.4; the methods and results of Planck Collaboration XI (2014) were detailed in Ch. 2, Sect. 2.2. In the following pages we will give a more detailed description of the physical model fit of Planck Collaboration Int. XXIX (2014) before describing the work done in the second year of thesis.

We have seen in Ch. 1, Sect. 1.3.1 that conversions of emission measurements into extinction are of great astrophysical interest. For this reason, Planck Collaboration XI (2014) combined the *Planck* emission maps to the SDSS QSO extinction survey, with the statistical methods described in Appendix C, and recovered two different conversion ratios from emission parameters to extinction:

$$\begin{aligned} E(B-V)/\tau_0 &= (1.49 \pm 0.03) \times 10^4 \\ E(B-V)/\mathcal{R} &= (5.40 \pm 0.09) \times 10^5 \end{aligned} \tag{3.1}$$

Using the average $\mathcal{R}/N_{\rm H}$ for the diffuse ISRF, Planck Collaboration XI (2014) calculates that the second of Eq. 3.1 is equivalent to E(B-V)/$N_{\rm H}$ $\sim 1.44\,10^{-22}$ mag cm^2, or 0.8-0.85 times the classical value found in the seminal paper by Bohlin et al. (1978). The difference in estimates is understandable in terms of dust evolution when one considers that Bohlin et al. (1978) probed a denser medium than Planck Collaboration XI (2014).

3.1.1 *Planck* Collaboration (Intermediate) XXIX: all-sky physical model fit

ISRF intensity in the DL07 model

As in the previous chapter, the description of my own work will be preceded by a section detailing other results in the *Planck* collaboration, which constitutes the basis for my analysis.

Planck Collaboration Int. XXIX (2014) presented a fit to the dust emission SED aver the whole sky akin to Planck Collaboration XI (2014), but used a physical dust model rather than a modified black body: the DL07 model presented in Ch. 1, Sect. 1.3.3, with the modifications explained in Aniano et al. (2012). A test of DL07 is very important, since it is one of the models most used to estimate dust and gas masses: the mass estimate is usually obtained by fitting dust emission as per Ch. 1, Sect. 1.3.1 (Draine et al. 2007; Aniano et al. 2012). The properties of its grains have already been given in Ch. 1, Sect. 1.3.3, but its representation of the ISRF, which is key to the classification of the Planck Collaboration Int. XXIX (2014) science products, is worth exploring.

Rather than using a single value such as G_0 to designate ISRF intensity (see Ch. 1, Sect. 1.1.2), DL07 takes into account the existence of unusually-bright regions (*e.g.* as near young star associations) and employs a distribution of ISRF intensities parametrized by the dimensionless scale factor U, distributed within a minimum and a maximum value: $U_{\rm min} < U < U_{\rm max}$. The model assumes that a mass fraction $1-\xi$ of the dust[1] (where $0 < \xi < 1$) is within the "typical" ISM, subjected to a radiation field with $U = U_{\rm min}$; the remaining dust is in brighter regions, exposed to ISRF intensities that follow a power-law: $dM/dU \propto U^{-\alpha}$. In other words, the distribution of starlight intensity is

[1]In Draine & Li (2007) and Planck Collaboration Int. XXIX (2014), the parameter which we call ξ is called γ. Since in this thesis we already use the letter γ to design the angle between the magnetic field and the plane of the sky (Ch. 1, Sect. 1.3.2), we decided to change the DL07 nomenclature to avoid confusion.

composed of a delta function at $U = U_{\rm min}$ plus a power law extending between $U_{\rm min}$ and $U_{\rm max}$. Due to the few photometric constraints available, and since model results are not very sensitive to the precise values of α and $U_{\rm max}$, Planck Collaboration Int. XXIX (2014) uses the fixed values $\alpha = 2$ and $U_{\rm max} = 10^7$.

Aside from its distribution in values, the parameter U is used in the same way as G_0 as explained in Ch. 1, Sect. 1.1.2: the ISRF is modeled as $u_\lambda = U \times u_\lambda^{\rm MMP83}$, where $u_\lambda^{\rm MMP83}$ is the ISRF by Mathis et al. (1983). DustEM, which can only use single-intensity ISRF spectra of the form $u_\lambda = G_0 \times u_\lambda^{\rm MMP83}$, is limited to ISRF spectra that would have $\xi = 0$ in the DL07 parametrization. The parameters G_0 and $U_{\rm min}$ are functionally the same; however in this chapter we will use both terms to refer to the ISRF obtained imposing $\xi = 0$ and leaving ξ as a free parameter respectively, as the two values may be different.

All-sky DL07 fit

Unlike Planck Collaboration XI (2014), which concentrated on big grains and thus only fitted the emission for $\lambda > 100\,\mu$m, the DL07 model also fits the PAH emission and therefore needs MIR data. The fit was operated on all the *Planck* maps (350, 550, 850, 1380, 2100 and 3000 μm), plus the 60-μm and 100-μm *IRAS* maps and the 12-μm *WISE* map. Thus are obtained all-sky maps of the fit parameters $\Sigma_{\rm M_d}$ (dust surface density), $q_{\rm PAH}$ (mass fraction of PAHs in the dust), $U_{\rm min}$ and ξ (as described above). Using the model optical properties, one can use $\Sigma_{\rm M_d}$ to make a map of the expected value of the extinction; we call this model parameter $A_{\rm V}^{\rm fit}$ to distinguish it from the actual observed $A_{\rm V}$.

An important consistency check for the model is to compare $A_{\rm V}^{\rm fit}$ and $A_{\rm V}$: if the model were correct, the two should be equal. The observational $A_{\rm V}$ is obtained from the SDSS survey on QSOs as in Planck Collaboration XI (2014) – see Appendix C – with the following differences:

- The tenth SDSS release data is added to the seventh release, bringing the number of usable QSOs to 224 245;
- The intrinsic colour recovery (Eq. C.1) uses $A_{\rm V}^{\rm fit}$ as a column density tracer instead of $N_{\rm H_I}$;
- Since the validity of $A_{\rm V}^{\rm fit}$ as a column density tracer depends on the validity of the DL07 optical properties, the QSOs are binned both by z and $U_{\rm min}$ instead of just by z to find out if this supposedly constant ratio actually depends on this model parameter.

The QSO lines of sight sample regions of low $A_{\rm V}$ with a median value of ~ 0.10, even though the set of SEDs describe the data over a much larger fraction of the sky ($\geq 70\%$) with $A_{\rm V}$ up to unity[2]. This means that they mainly sample the diffuse interstellar medium.

The $A_{\rm V}^{\rm fit}$-$A_{\rm V}$ comparison shown in Fig. 3.1. Not only the ratio of the two is on average 0.52 rather than unity; it also evidently depends on $U_{\rm min}$, with an empirical relation of $A_{\rm V}^{\rm fit}/A_{\rm V} = 0.35 + 0.31 \times U_{\rm min}$. The first of these effects implies that DL07 has not the same optical properties of actual interstellar dust, and that either its V-band extinction is too low or its submillimeter opacity is too high, or both. The second effect shows that zones with different $U_{\rm min}$ have dust with different average optical properties. This implies that $U_{\rm min}$ traces not just starlight but also variations of optical properties, and therefore it is not a reliable tracer of the ISRF intensity.

SED family per unit extinction

We have already seen that the dust SED has to be normalized by a proxy of dust column density; $A_{\rm V}$ is as valid a proxy choice as $N_{\rm H}$. Furthermore, $A_{\rm V}$ normalization is not plagued by the uncertainties

[2] G. Aniano, private communication.

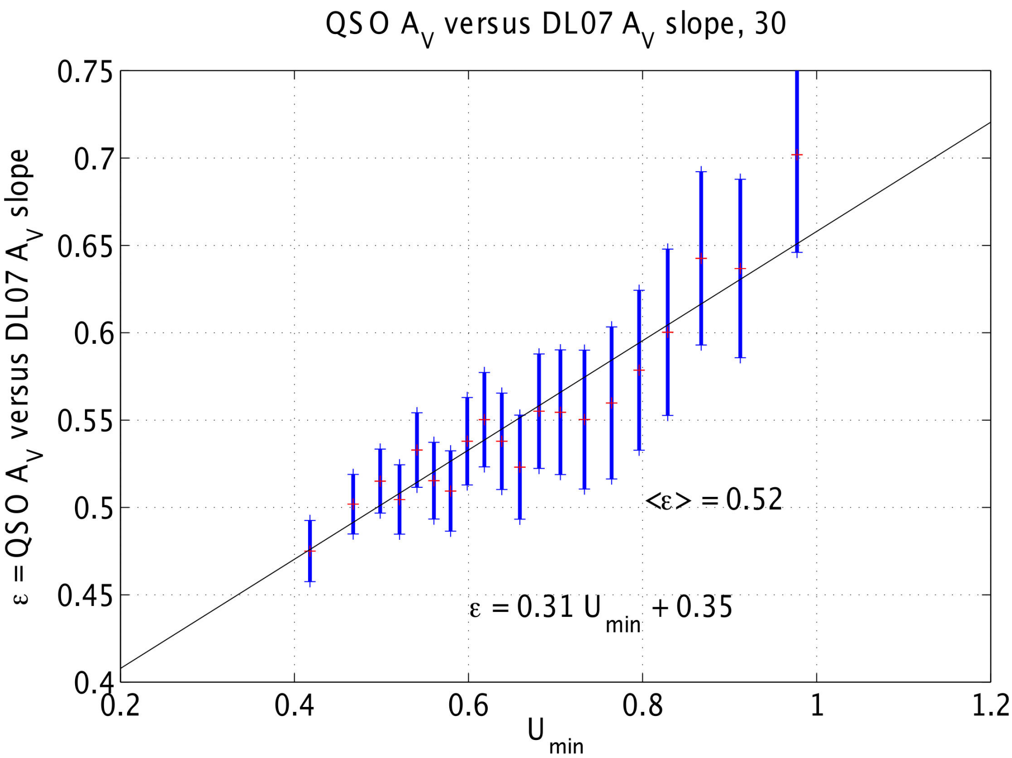

Fig. 3.1. Comparison between model and observations: the ratio $\varepsilon = A_\mathrm{V}/A_\mathrm{V}^\mathrm{fit}$ as a function of U_min. The median value, $\langle\varepsilon\rangle = 0.52$, indicates that DL07 predicts an A_V too high by a factor ~ 2 on average; the variation of ε with U_min indicates that dust at different temperatures has different optical properties. From Planck Collaboration Int. XXIX (2014).

of N_H normalization in the amount of dark gas, in the amount of WIM and in the value of dust-to-gas ratio. An uncertainty remains in the dust optical properties in extinction, which determine the ratio of column density to A_V, but this uncertainty was also present in the N_H normalization. An A_V-normalized SED is comprised purely of self-consistent dust data. There is another advantage to normalization by A_V: Planck Collaboration Int. XXIX (2014) showed that it is important to not only fit the dust extinction and the emission, but to control that they be coherent with each other. A model that fits the extinction curve and the A_V-normalized SED automatically satisfies this coherence condition.

For these reasons it would be useful to have a “typical” normalised SED I_λ/A_V for the diffuse ISM, to be used by future generations of dust models in the same way as the average diffuse ISM extinction curve (Fitzpatrick & Massa 2007) has been a benchmark for dust model calibration. As we saw in the previous sections, however, Planck Collaboration Int. XXIX (2014) shows that the properties of dust are non-uniform and correlated with U_min. Therefore, rather than a single I_λ/A_V averaged over all the sky, it would be practical to have a family of normalized SEDs ordered by U_min: $I_\lambda(U_\mathrm{min})/A_\mathrm{V}$. It may seem impractical to make U_min central in the definition of the SED family, since it is now clear that it is not a good tracer of ISRF intensity. However, U_min still has a meaningful relation with an observable: the characteristic of the dust SED that most influences the value of U_min is the position of its peak (U_min is higher if the SED peaks at shorter wavelengths), making U_min essentially a proxy for dust temperature.

One of the products of Planck Collaboration Int. XXIX (2014) is a family of 20 SEDs, calculated over 20 U_min bins each containing the same number of QSOs. Since the individual A_V measurements for QSOs are very noisy, it was not practical to calculate each value of I_λ/A_V and then average.

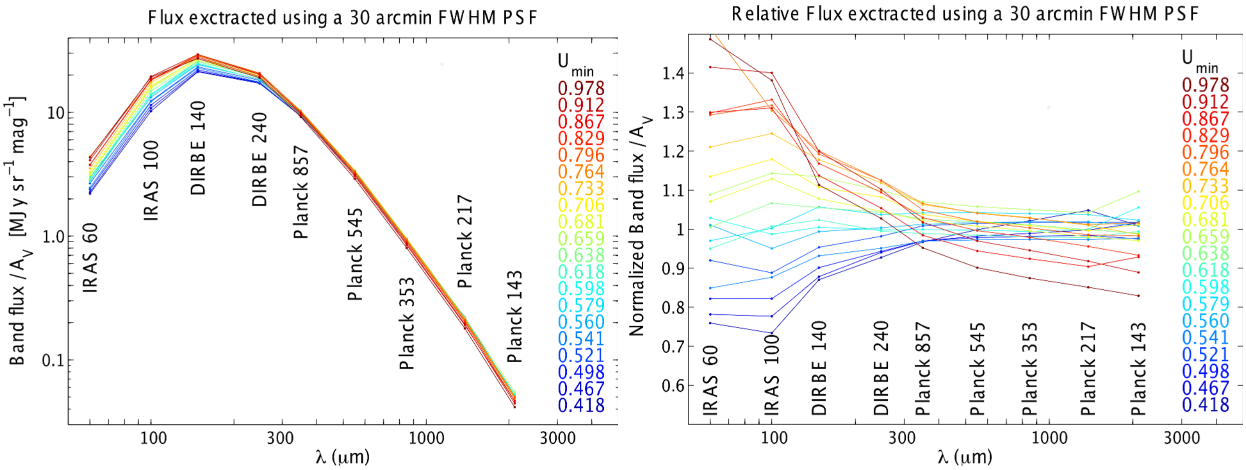

Fig. 3.2. The family of 20 A_{V}-normalized SEDs from Planck Collaboration Int. XXIX (2014). The SEDs on the right are further normalized by the average SED. The data at 140 and 240 μm from DIRBE are shown for completeness but not included with the other data in Planck Collaboration Int. XXIX (2014), since they are too noisy to be of use. From Planck Collaboration Int. XXIX (2014).

Instead, Planck Collaboration Int. XXIX (2014) obtained I_λ/A_{V} as the slope of a linear regression fit of I_λ as a function of A_{V}, for each U_{min} bin. Obtaining I_λ/A_{V} as result of a regression also has the advantage that it is independent of the intensity zero point in all bands. The SEDs are shown in Fig. 3.2. They comprise the two longest-wavelength *IRAS* bands and all the *Planck* bands except the longest-wavelength one (which was too noisy); the overall wavelengths coverage is therefore from 60 μm to 2.1 mm. As in the case of the $A_{\mathrm{V}}^{\mathrm{fit}}/A_{\mathrm{V}}$ ratio, the uncertainty on QSO extinction is too high to use them singularly and a statistical method has to be employed. For each band and U_{min} the value of I_λ/A_{V} is actually obtained as the slope of the I_λ/A_{V} relation. The large number of QSOs – over 11 000 for each U_{min} – is essential in overcoming the large uncertainty on A_{V} measurements.

3.1.2 Purpose of the present work

During the PhD we extended the analysis of the diffuse ISM by Planck Collaboration XI (2014) and Planck Collaboration Int. XXIX (2014) to other physical dust models, publishing the results in the paper Fanciullo et al. (2015). In the course of the work, we developed a new method of estimating the ISRF intensity using the dust radiance and A_{V}. The interest of this work is manifold:

- The comparison of different dust models will help understand which of the findings described in this section are model-dependent and which ones are not;
- Related to the above, the comparison of different models will help find out if one model comes closer to explaining the observations consistently;
- Unlike the widely-used ISRF estimate from the dust SED fit, the new estimator is independent of the optical properties in the far infrared and submillimeter, allowing for the first time to estimate the variations in ISRF intensity and in submillimeter opacity separately.

This work's results will be useful to the astrophysical community in the creation and discussion of new physical dust models, which will have to include the physical justification of the observed inhomogeneities in dust properties.

3.2 Data

The data we use for our analysis is a subset of the A_V-normalized SED family from Planck Collaboration Int. XXIX (2014) introduced in the previous section. We are interested in the properties of the big grains in thermal equilibrium, mainly because we have not enough data to reasonably constrain the stochastically-heated grains: we would need a measure of the extinction in the UV to determine the total mass of small particles, and a full mid- and near-infrared emission spectrum is needed to constrain the small particle temperature and size distribution. Therefore, we limit ourselves to the 100 μm *IRAS* band and the 350, 550, and 850 μm *Planck* bands. Longer wavelengths do not really change the results of our analysis, while the 60 μm band is dominated by the stochastically-heated grains. Dust models agree in attributing the V band extinction mainly to big grains, so the subset of I_λ/A_V on which we work depends for the most part on the properties of big dust grains.

The $U_{\rm min}$ of the SEDs spans a range of 0.42 to 0.98, with an average of 0.66 and a standard deviation of 0.14. Fig. 3.3 shows the value I_λ/A_V for the bands we use. To make the picture clearer, only a subset of five SEDs is shown out of the 20 we employ: the median SED ($U_{\rm min} = 0.66$), the two extreme SEDs ($U_{\rm min} = 0.98$ and $U_{\rm min} = 0.42$), and the SEDs closest to being $1\,\sigma$ above and below the median ($U_{\rm min} = 0.80$ and 0.52 respectively). The figure shows that the A_V-normalised SEDs are very similar over the*Planck* wavelength range, and most of the variations are in the *IRAS* 100 μm band. Tab. 3.1 lists the characteristics of the SEDs: the $U_{\rm min}$ and the parameters of a modified blackbody fit to them. A striking feature is that $\mathcal{R}/A_V$ increases with temperature, in apparent contrast with the results of Planck Collaboration XI (2014), where $\mathcal{R}/N_H$ and T were found to be independent of each other (Ch. 2, Fig. 2.1). The reason for this difference is still under investigation, but it is likely that the fact of normalizing by A_V rather than N_H plays a role. Also, the two papers do not study exactly the same environments: Planck Collaboration XI (2014) is limited to $N_H < 2.5 \cdot 10^{20}\,{\rm cm}^{-2}$ ($A_V \sim 0.1$), while Planck Collaboration Int. XXIX (2014) goes as far as $A_V \sim 1$.

3.3 Methodology

We analysed the observations in two different steps. During the first step we fit the SED to obtain model dust parameters such as G_0 (tracer of ISRF intensity) and A_V (indirect tracer of dust column density), as well as observables such as the radiance $\mathcal{R}$. During the second step, we estimate the ISRF intensity from the observed A_V and dust radiance $\mathcal{R}$, and then use it to predict the model dependent SED.

3.3.1 SED fit

The fitting procedure

The 20 SEDs of Planck Collaboration Int. XXIX (2014) have both stochastic and systematic uncertainties. What is important in stochastic uncertainties is their relative value from one band to another, which defines the statistical weight to be applied to each band in the fitting routine. The stochastic errors in each band of I_λ/A_V are negligible, since each SED is an average over more than 11 000 observations. The same is not true of systematic uncertainties, which affect all observations in the same way and therefore are not affected by averaging. Systematic uncertainties in the dust SED come mainly from the photometric calibration: the calibration uncertainty is important at 100 μm (1σ error bar = 13.6%) and at 350 and 550 μm (1σ = 10%); we decided to neglect it at longer wavelengths where it is much smaller ($\lesssim$ 1%) (Miville-Deschênes & Lagache 2005; Planck Collaboration VIII 2014). We estimated the effect of this uncertainty via Monte Carlo simulations.

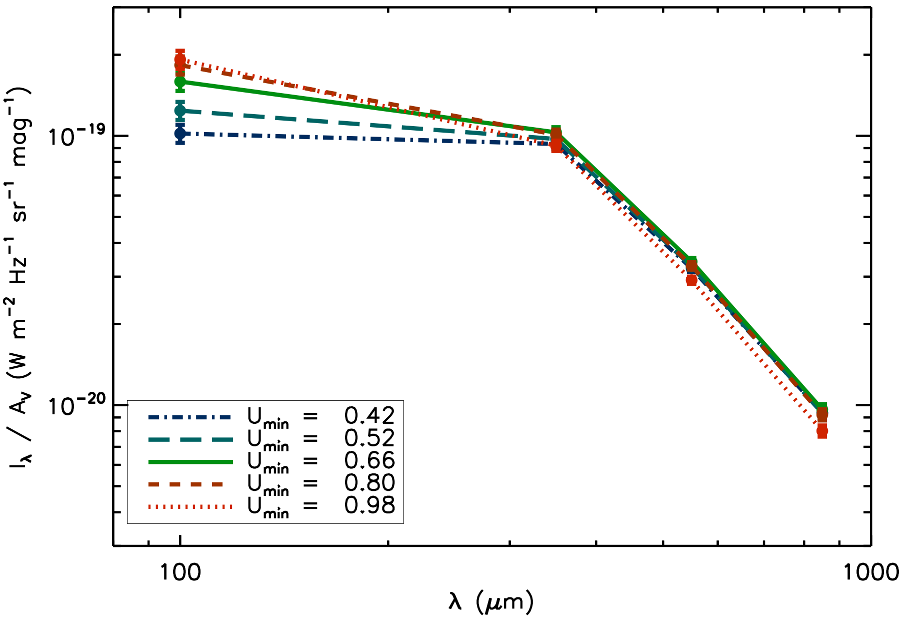

Fig. 3.3. Set of data, from the Planck Collaboration Int. XXIX (2014) A_V-normalized SEDs, that we use in this chapter. Only the bands centered at 100, 350, 550 and 850 μm are used. Only 5 SEDs are show here for clarity (see text), but all 20 SEDs have been used.

$U_{\rm min}$	T (K)	β	$10^5 \cdot \tau_0/A_{\rm V}$	$10^7 \cdot \mathcal{R}/A_{\rm V}$
0.418	**18.68**	**1.607**	**1.888**	**4.770**
0.467	18.72	1.645	1.820	4.958
0.498	18.94	1.641	1.772	5.127
0.521	**19.15**	**1.634**	**1.807**	**5.486**
0.541	19.25	1.631	1.719	5.352
0.560	19.44	1.620	1.772	5.718
0.579	19.49	1.632	1.798	6.014
0.598	19.62	1.623	1.706	5.836
0.618	19.77	1.620	1.663	5.900
0.638	19.88	1.620	1.700	6.226
0.659	**20.00**	**1.616**	**1.749**	**6.590**
0.681	20.11	1.621	1.647	6.446
0.706	20.28	1.614	1.648	6.670
0.733	20.36	1.620	1.669	6.985
0.764	20.65	1.607	1.635	7.239
0.796	**20.75**	**1.608**	**1.584**	**7.229**
0.829	20.87	1.612	1.530	7.251
0.867	20.94	1.624	1.433	7.080
0.912	21.08	1.629	1.455	7.517
0.978	**21.28**	**1.634**	**1.325**	**7.308**

Table 3.1. $U_{\rm min}$ and modified black body parameters for the Planck Collaboration Int. XXIX (2014) SEDs.

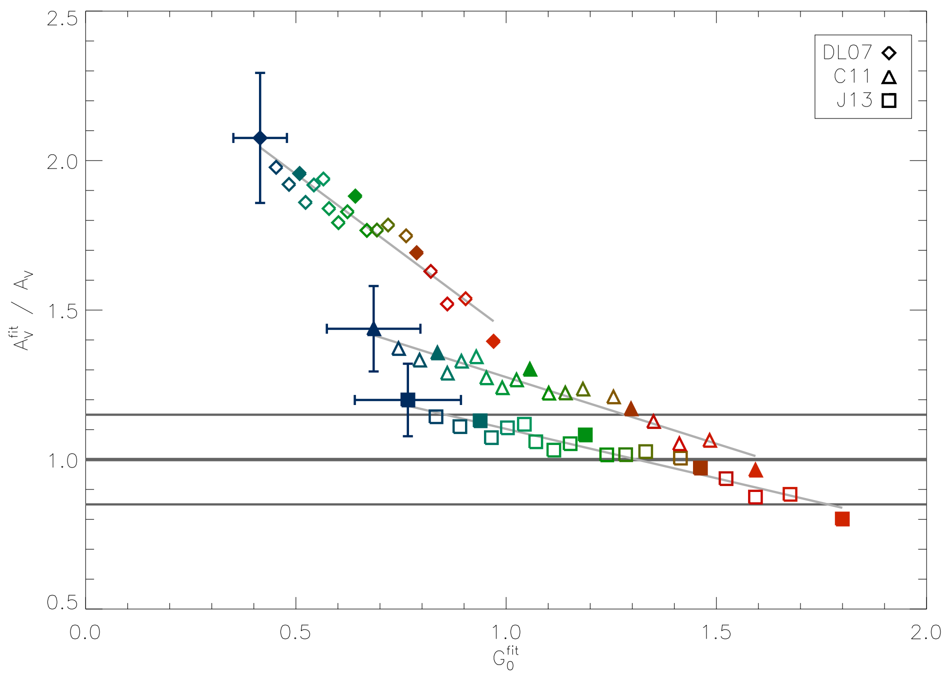

Fig. 3.4. G_0^{fit} and $A_{\mathrm{V}}^{\mathrm{fit}}/A_{\mathrm{V}}$ for the Planck Collaboration Int. XXIX (2014) SEDs, obtained by fitting the DL07, C11 and J13 models. The filled symbols correspond to the SEDs that were shown in Fig. 3.3. To help distinguish the models, linear fits to each of them are represented as thin oblique lines. The thick horizontal grey line corresponds to $A_{\mathrm{V}}^{\mathrm{fit}} = A_{\mathrm{V}}$, while the thinner horizontal grey lines indicate the 15% uncertainty on A_{V}.

Specifically, for each observed SED, we realized 1000 simulations of random Gaussian-distributed errors for the 100, 350, and 550 μm bands, with the photometric error at 350 and 550 μm set equal since both channels are calibrated on planets (the uncertainties are dominated by the planet model used, not by noise). We performed a fit on all simulations, obtaining 1000 values of each fit parameter for each SED: the mean of these was taken as the fiducial value of the fit parameter and the standard deviation as the uncertainty. The systematic uncertainty in A_{V} is estimated by Planck Collaboration Int. XXIX (2014) to be $\sim 15\%$.

To ensure that the fitting procedure is consistent across all models we fit the 20 Planck Collaboration Int. XXIX (2014) SEDs not only with with C11 and J13, but also with DL07 with the constraint that $\xi = 0$: as we have explained in Sect. 3.1.1, in this conditions the fitting procedure of DL07 should become equivalent to that of DustEM.

The dust extinction and emission are computed by interpolating an existing library in the case of DL07 (Aniano et al. 2012) and using DustEM in the case of C11 and J13. The observational SEDs were fitted using a χ^2-minimising procedure. From the fit of the SEDs we obtain the ISRF intensity G_0^{fit}. The same fit, since the SEDs are normalised by the QSO-derived A_{V}, returns the ratio of the model extinction to the observed extinction, $A_{\mathrm{V}}^{\mathrm{fit}}/A_{\mathrm{V}}$. The fit results are shown in Fig. 3.4; each symbol represents a pair of values (G_0^{fit}, $A_{\mathrm{V}}^{\mathrm{fit}}/A_{\mathrm{V}}$) for a different model and SED. A perfect model would find a value of $A_{\mathrm{V}}^{\mathrm{fit}}/A_{\mathrm{V}} = 1$ (thick horizontal grey line). The thinner horizontal grey lines show the 15% systematic uncertainty in A_{V} mentioned in Section 3.2. This uncertainty is identical for all SEDs, and so it affects the significance of the average $A_{\mathrm{V}}^{\mathrm{fit}}/A_{\mathrm{V}}$ of the models, but does not affect either the dependence of $A_{\mathrm{V}}^{\mathrm{fit}}/A_{\mathrm{V}}$ on G_0 or the differences between models. The error bars on (G_0^{fit}, $A_{\mathrm{V}}^{\mathrm{fit}}/A_{\mathrm{V}}$) are obtained from Monte-Carlo simulations, as explained in Sect. 3.2. The errors on

	DL07		C11		J13	
$U_{\rm min}$	G_0	$A_{\rm V}^{\rm fit}/A_{\rm V}$	G_0	$A_{\rm V}^{\rm fit}/A_{\rm V}$	G_0	$A_{\rm V}^{\rm fit}/A_{\rm V}$
0.418	**0.415**	**2.076**	**0.685**	**1.438**	**0.766**	**1.199**
0.467	0.453	1.978	0.744	1.371	0.833	1.143
0.498	0.484	1.920	0.794	1.332	0.889	1.110
0.521	**0.509**	**1.957**	**0.837**	**1.357**	**0.938**	**1.130**
0.541	0.523	1.860	0.860	1.289	0.965	1.073
0.560	0.543	1.918	0.894	1.329	1.003	1.106
0.579	0.565	1.938	0.929	1.344	1.043	1.118
0.598	0.579	1.840	0.953	1.273	1.070	1.059
0.618	0.601	1.792	0.991	1.240	1.113	1.031
0.638	0.623	1.829	1.024	1.266	1.152	1.053
0.659	**0.641**	**1.881**	**1.056**	**1.302**	**1.188**	**1.082**
0.681	0.669	1.767	1.101	1.222	1.239	1.016
0.706	0.693	1.768	1.141	1.223	1.284	1.016
0.733	0.719	1.784	1.182	1.236	1.332	1.027
0.764	0.762	1.748	1.255	1.210	1.415	1.004
0.796	**0.787**	**1.692**	**1.297**	**1.170**	**1.462**	**0.975**
0.829	0.821	1.629	1.351	1.127	1.523	0.936
0.867	0.860	1.520	1.412	1.053	1.593	0.874
0.912	0.904	1.538	1.484	1.064	1.675	0.884
0.978	**0.970**	**1.396**	**1.593**	**0.965**	**1.800**	**0.801**

Table 3.2. Results of physical model fits to Planck Collaboration Int. XXIX (2014) SEDs.

the $G_0^{\rm fit}$ and on $A_{\rm V}^{\rm fit}/A_{\rm V}$ are strongly anti-correlated, with an average Pearson correlation coefficient of -0.77 (DL07) to -0.84 (C11 and J13). Since these uncertainties are systematic, the plots may be shifted vertically or horizontally, but their shape remains essentially the same.

Fit results: implications for optical properties

The values of $G_0^{\rm fit}$ and $A_{\rm V}^{\rm fit}/A_{\rm V}$ that result from the fits are listed in Tab. 3.2. It is important to point out that all the models fit the shape of the SED very closely; it is the $I_\lambda/A_{\rm V}$ ratio that they generally fail to reproduce. We can also see from Tab. 3.2 that the values of $G_0^{\rm fit}$ for the DL07 model fit are very close to $U_{\rm min}$: this means that, in the context of the diffuse ISM and for $\lambda \geq 100\,\mu$m, the DL07 ISRF model is not a significant improvement over a single-intensity ISRF.

The J13 model fits the data well, with an average $A_{\rm V}^{\rm fit}$ which coincides with the expected value. The C11 model overestimates $A_{\rm V}^{\rm fit}$ by $\sim 30\%$. The DL07 model shows the largest discrepancy, with an $A_{\rm V}^{\rm fit}$ that is overestimated by a factor ~ 1.8, as already pointed out by Planck Collaboration Int. XXIX (2014). All models, however, show a negative correlation between G_0 and $A_{\rm V}^{\rm fit}/A_{\rm V}$ whereas $A_{\rm V}^{\rm fit}/A_{\rm V}$ should be unity. It should be noted that the models do not fail to fit the $A_{\rm V}$-normalized SEDs. Each model reproduces dust emission correctly; to do so, however, they need to set their parameters to values that are incompatible with the observations in extinction. These trends for $A_{\rm V}$ and G_0 in Fig. 3.4 resemble the well-known T-τ_0 anti-correlation caused by noise (Shetty et al. 2009a,b), but this is not the case here: since each SED is an average over more than 11 000 spectra, the statistical uncertainty for each SED is negligible.

We will now show that, under a set of physically realistic hypotheses, the negative correlation between G_0 and $A_{\rm V}^{\rm fit}/A_{\rm V}$ can be imputed to a change in the relative values of τ_0 (or, more generally, the typical opacity in the submillimeter $\tau_{\rm sub}$) and $A_{\rm V}$. The power absorbed by dust is

$$\begin{aligned}P_{\rm in} &= \int_\lambda I_\lambda \, \tau_\lambda \, (1 - Al_\lambda) \, d\lambda \\ &= G_0 \cdot A_{\rm V} \int_\lambda \overline{I_\lambda} \, \overline{\tau_\lambda} \, (1 - Al_\lambda) \, d\lambda \\ &= G_0 \cdot A_{\rm V} \cdot \langle 1 - Al \rangle\end{aligned} \tag{3.2}$$

where $I_\lambda = G_0 \cdot \overline{I_\lambda}$ is the ISRF, $\tau_\lambda = A_{\rm V} \cdot \overline{\tau_\lambda}$ is the wavelength-dependent dust optical depth and Al_λ is the wavelength-dependent dust albedo (Ch. 1, Sect. 1.2.3). This parametrization puts in evidence how the absorbed power depends on the ISRF intensity, the dust column density (traced by $A_{\rm V}$) and the details of the absorption, $\langle 1 - Al \rangle$ being the wavelength-integrated albedo weighted on the shapes (but not the intensities) of the ISRF and the dust extinction curve. For grains in thermal equilibrium, we know that $P_{\rm in} = \mathcal{R}$ at all times. Let us make the following assumptions:

- The far infrared spectral index β is constant. As we see in Tab. 3.1, its variations are indeed small compared to the other modifed black body parameters;
- The black body temperature T, despite not being the physical temperature of any of the dust populations, is however related to them; *i.e.* , an increase in the physical temperature of grains implies an increase in T and vice versa;
- The albedo of the model is correct, or at least the corrections to the model's $\langle 1 - Al \rangle$ are much smaller than those in $A_{\rm V}^{\rm fit}$. This is not unreasonable since $\langle 1 - Al \rangle$ is determined by optical properties alone, while $A_{\rm V}$ depends on both optical properties and dust mass, so its determination has more potentiel weak points. Nonetheless, this is the weakest of our assumptions, and in Sect. 3.4 we will see what happens when we drop it.

The constancy of β allows to rewrite the radiance formula, Eq. 2.2, as $\mathcal{R} \propto \tau_0 \cdot T^{4+\beta}$. This, combined with Eq. 3.2, results in:

$$\tau_0 \cdot T^{4+\beta} \propto G_0 \cdot A_{\rm V} \cdot \langle 1 - Al \rangle \tag{3.3}$$

As we said, the model correctly reproduces the radiance, so the model-derived values of the left and right side of Eq. 3.3 are correct. From the hypothesis of correctness of $\langle 1 - Al \rangle$ it follows that the value of $G_0 \cdot A_{\rm V}$ from the model, $G_0^{\rm fit} \cdot A_{\rm V}^{\rm fit}$, is also correct. It follows that if an SED fit provides the wrong $A_{\rm V}^{\rm fit}$ the value $G_0^{\rm fit}$ is also biased: if we define[3] $\digamma = A_{\rm V}^{\rm fit} / A_{\rm V}$, a less biased estimate for the ISRF intensity G_0 is $\digamma \cdot G_0^{\rm fit}$.

We know that models correctly fits the SED shape, meaning they provide the correct value for T; since they provide the correct radiance $\mathcal{R} \propto \tau_0 \cdot T^{4+\beta}$, they also provide the correct τ_0. What is wrong in the models is the conversion from τ_0 to $A_{\rm V}$. To correct the model, we need to change the ratio of the submillimeter to optical cross-sections by the factor $\digamma$. By increasing both the radiation field intensity and the dust emissivity per unit extinction by the same factor $\digamma$, the SED (temperature, optical depth) is conserved, with a lower, correct, $A_{\rm V}$.

To resume, the fit to the Planck Collaboration Int. XXIX (2014) SEDs taught us that:

- Models show similar performances in fitting I_λ, but very different performances in finding the average $I_\lambda / A_{\rm V}$, with J13 giving a perfect result and DL07 being off by a factor 2;
- Nonetheless, all of the models have problems in reproducing the variations of $I_\lambda / A_{\rm V}$ with temperature, as shown by the non-unity values of $\digamma = A_{\rm V}^{\rm fit} / A_{\rm V}$;

[3]With respect to the nomenclature of Planck Collaboration Int. XXIX (2014), $\digamma$ corresponds to the inverse of the ratio ε which is also seen in Fig. 3.1

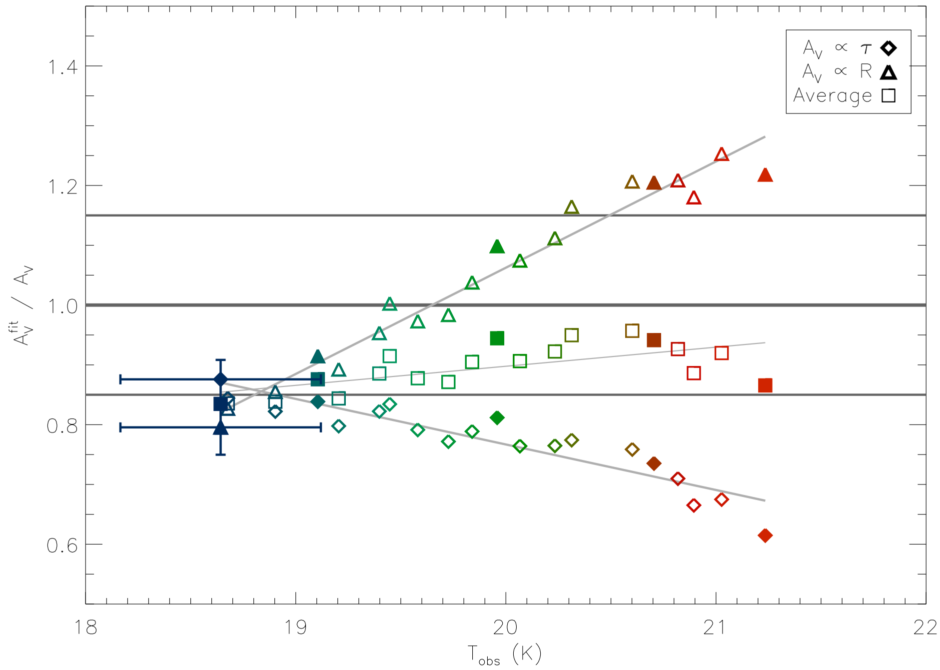

Fig. 3.5. Scatter plot of A_V^{fit}/A_V and fitted dust temperature for the modified black-body fit. Two alternative estimates of A_V are shown (see text), plus an average value. The horizontal grey lines show $A_V^{fit}/A_V = 1$ and the 15% uncertainty in the A_V normalisation (Sect. 3.2). All points have similar relative uncertainty; the bars for the lowest U_{min} are shown. The uncertainties are systematic, so they affect each point in the same way; errors on the two axes are strongly anti-correlated. The $U_{\rm min}$ colour scheme is the same as Fig. 3.4; the filled symbols correspond to the SEDs shown in Fig. 3.3.

- The fact that all models reproduce the SED correctly means that biases in the value of A_V^{fit} are coupled with biases in G_0^{fit};
- To modify a biased model and correctly reproduce the variations in I_λ/A_V, one needs to increase the ratio $C_{\rm submm}/C_V$ by a factor $\mathcal{F}$, and to increase G_0^{fit} by the same factor (or $G_0^{fit} \cdot \langle 1 - Al \rangle$ in the case where we allow for variations in Al).

A trivial consequence of the last point is that, since A_V^{fit}/A_V – and the correction factor $\mathcal{F}$ – changes with SED temperature, dust at different temperatures in the diffuse ISM will have (on average) different optical properties. We see this in the same amount for all models, so we are confident that this is an actual property of interstellar dust rather than a model issue with the modeling.

Black body model fit

For comparison, we also fitted the data with a modified black-body. The results of this new fit are qualitatively similar to those obtained in the previous sections, in that the conversion from emission to extinction shows a marked temperature-dependent bias. Fig. 3.5 shows two different estimates of A_V as a function of T, obtained by applying the Planck Collaboration XI (2014) emission-to-extinction conversions (Eq. 3.1) to the modified black body fit τ_0 and $\mathcal{R}$ and the average R_V for the diffuse ISM, 3.1.

The two estimates of A_V differ both by their average value and their trend with temperature: the A_V obtained from τ_0 is about 20% too low on average, and $\mathcal{F} = A_V^{fit}/A_V$ decreases with temperature

$U_{\rm min}$	$G_0^{\mathcal{R}}$ (DL07)	$G_0^{\mathcal{R}}$ (C11)	$G_0^{\mathcal{R}}$ (J13)
0.418	**0.861**	**0.982**	**0.924**
0.467	0.896	1.021	0.961
0.498	0.927	1.056	0.994
0.521	**0.992**	**1.130**	**1.065**
0.541	0.968	1.103	1.038
0.560	1.035	1.179	1.110
0.579	1.090	1.240	1.168
0.598	1.057	1.203	1.133
0.618	1.069	1.216	1.146
0.638	1.129	1.284	1.210
0.659	**1.196**	**1.359**	**1.282**
0.681	1.169	1.329	1.253
0.706	1.211	1.376	1.298
0.733	1.269	1.441	1.360
0.764	1.315	1.493	1.410
0.796	**1.313**	**1.491**	**1.408**
0.829	1.318	1.496	1.412
0.867	1.286	1.460	1.378
0.912	1.367	1.551	1.464
0.978	**1.328**	**1.508**	**1.423**

Table 3.3. $G_0^{\mathcal{R}}$ for the Planck Collaboration Int. XXIX (2014) SEDs.

like the physical models (Fig. 3.4); the $A_{\rm V}$ obtained from $\mathcal{R}$ has a good average value, but F increases with temperature. We also show the geometric average of the two, which matches the expected value better, despite having no physical justification. Interestingly, the two estimates implicitly make opposite assumptions: the $A_{\rm V}$ obtained from τ_0 assumes that the dust optical properties are fixed, or at least $\tau_0/A_{\rm V}$ is fixed; while the $A_{\rm V}$ from $\mathcal{R}$ assumes a fixed G_0, or at least a fixed absorbed power per grain. This means that the warmer dust has lower opacity than expected from models with fixed dust properties, but higher opacity than expected from models where variable optical properties account for all observed variations. This strongly suggests that the variations observed in $I_\lambda/A_{\rm V}$ are partly due to $\tau_{\rm sub}$; this is what we are going to quantify in Sec. 3.3.2.

3.3.2 G_0 estimation and artificial SED reproduction

G_0 recovery and SED reproduction: methodology

Dust emission fitting assumes that the model optical properties are correct both in emission and extinction, which is why it yields biased results when optical properties are not correct. During the PhD we developed an alternative way of testing dust models, which requires to know both emission and extinction but involves fewer assumptions on optical properties: using $A_{\rm V}$ and $\mathcal{R}$, which both depend on extinction properties alone, one can obtain a G_0 estimate which we call $G_0^{\mathcal{R}}$. This estimate, being independent of emission properties, can be expected to be more robust and less biased than $G_0^{\rm fit}$, which depends on both emission and extinction properties.

We compute $\mathcal{R}$ in the same way for the observations and the models. We take the $A_{\rm V}$-normalised fluxes in the *IRAS* and *Planck* bands (in the case of the model we compute them from the output SED), we fit a modified black-body to the normalised SED (for $\lambda \geq 100\,\mu$m), and we substitute the resulting parameters in Eq. 2.2. The result, $\mathcal{R}^{\rm model}/A_{\rm V}^{\rm model}$, is a linear function of G_0, and can be inverted to find an estimate of G_0 from the radiance of an $A_{\rm V}$-normalised SED. The curve thus

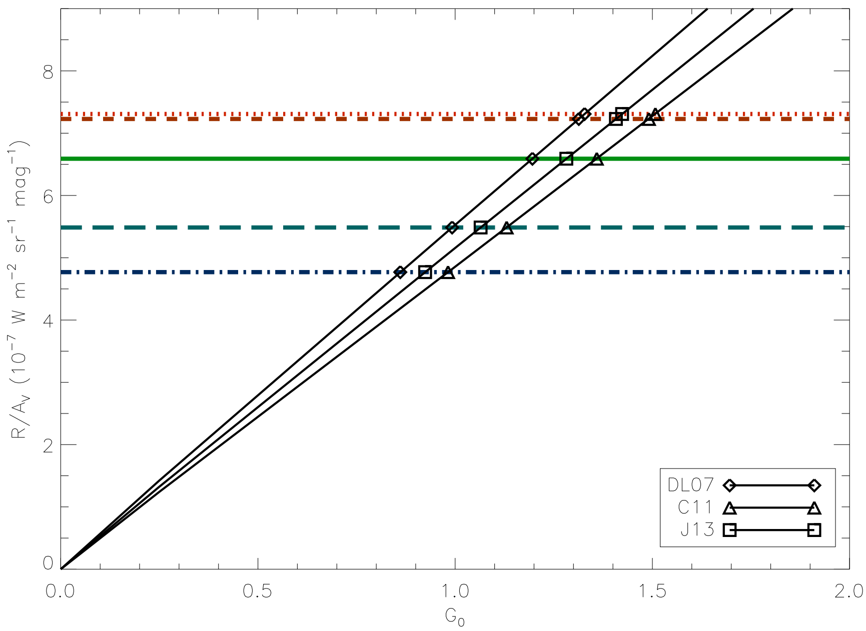

Fig. 3.6. Graphical representation of the recovery of $G_0^{\mathcal{R}}$. The lines from the origin are $\mathcal{R}^{\rm model}(G_0)/A_{\rm V}^{\rm model}$ for the three models. The horizontal lines correspond to $\mathcal{R}/A_{\rm V}$ for the five SEDs shown in Fig. 3.3. The values of $G_0^{\mathcal{R}}$ for each model and SED correspond to the abscissa of the intersection between the model line and the observation line.

obtained, $\mathcal{R}^{\rm model}(G_0)/A_{\rm V}^{\rm model}$, is shown in Fig. 3.6 for the three models. Since $\mathcal{R}$ only depends on absorption, the estimation of ISRF intensity given by this method, $G_0^{\mathcal{R}}$, is not affected by variations in submillimeter opacity. Our expectation that $G_0^{\mathcal{R}}$ be much less biased than $G_0^{\rm fit}$ is supported by the fact that G_0 estimates become much less model dependent when they are based on optical properties in extinction, and not only in emission: as can be seen in Tab. 3.3, $G_0^{\mathcal{R}}$ varies by $\sim 15\%$ between models, as opposed to the factor ~ 2 in $G_0^{\rm fit}$ (see Tab. 3.2)[4].

The values for $G_0^{\mathcal{R}}$, shown in Tab. 3.3 and in Fig. 3.6, vary by a factor 1.6 between the two extreme SEDs and by 1.3 if we only consider the SEDs within 1σ of the average – which would represent the "typical variance" of G_0 rather than the full range. By way of comparison, in Fig. 3.4, where the dust optical properties in the model are fixed and the ISRF is the only source of difference between SEDs, $G_0^{\rm fit}$ varies by a factor 2.3 between extremes and 1.6 within the "$\pm 1\sigma$" range.

SED reproduction: results

Using $G_0^{\mathcal{R}}$ as an ISRF estimate one can compute model SEDs and compare them to the observations. The shape of the SED thus obtained is not a good reproduction of the observed one, because the method is calibrated to reproduce the radiance per unit extinction $\mathcal{R}/A_{\rm V}$. The difference between the predicted and the observed SED comes from the variation in dust optical properties. We use $G_0^{\mathcal{R}}$ as a fixed parameter in the computation of the SEDs of the three dust models. The results are shown in Fig. 3.7. To highlight spectral shape variations, the SEDs have been normalised by the median observed SED and then further divided by their $\mathcal{R}/A_{\rm V}$. The J13 model reproduces the

[4]While $G_0^{\mathcal{R}}$ varies little across models (which are all made to reproduce the average extinction curve), it shows consistent variations for changes in size distribution, which affect scattering and therefore albedo. The effects of size distribution on $G_0^{\mathcal{R}}$ are to be studied, but preliminary calculations show that for realistic size distributions $G_0^{\mathcal{R}}$ variations are comparable or smaller than those of $G_0^{\rm fit}$ across models.

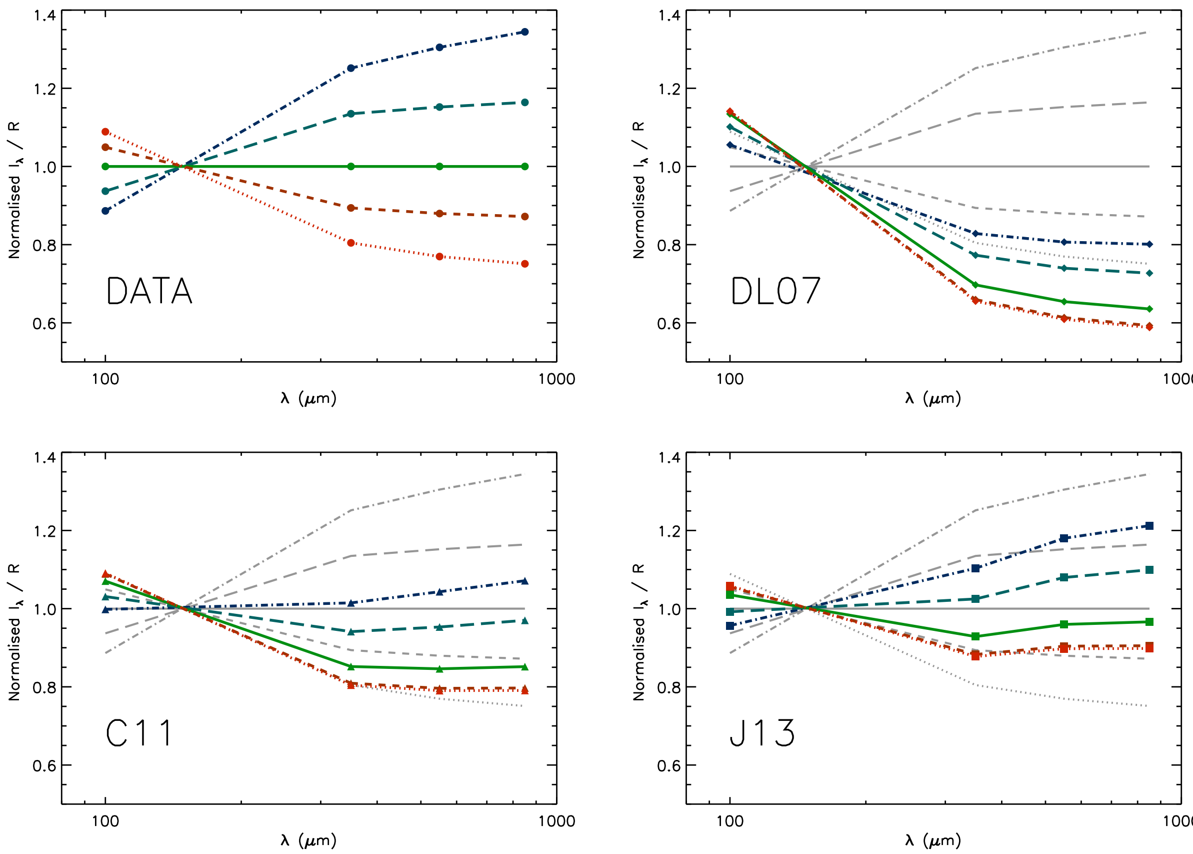

Fig. 3.7. Comparison of the observed Planck Collaboration Int. XXIX (2014) SEDs (top left) to the synthetic observation from the DL07, C11 and J13 models, obtained as described in Sect. 3.3.2. Due to the normalization used (see text), the colder SEDs increase with wavelength, the warmer ones decrease. The same five SEDs as Fig. 3.3 are shown, for clarity of illustration, using the same colour and line style scheme. The observations are plotted in grey behind the models to aid comparison

.

median SED almost perfectly. Predictions based on the C11 model systematically present an excess emission at short wavelengths and low emission at long wavelengths. This situation is even more drastic in the DL07 model. Furthermore, for all models, the normalised SEDs in Fig. 3.7 cover a smaller range than the data: the warm (high U_{min}) SEDs and the cold (low U_{min}) ones are closer in temperature for the model than they are for the observations.

The differences shown in Fig. 3.7 between the J13, C11 and DL07 dust models can be attributed mainly to their optical properties in emission (far infrared and submillimeter), as opposed to their optical properties in extinction: as seen in Fig. 3.6, the models have very similar optical properties in extinction. We find that the J13 model (Jones et al. 2013) is a better model for the diffuse ISM emission than that presented in Compiègne et al. (2011), and both of them are better than the Draine & Li (2007) model. The J13 model uses optical properties for silicates and amorphous carbon based on lab measurements. The Compiègne et al. (2011) and Draine & Li (2007) models use silicates with far infrared and submillimeter optical properties extrapolated from mid-infrared astronomical observations, as explained in Ch. 1, Sect. 1.3.3. Furthermore, Draine & Li (2007) is unique among the models in that its carbon dust is assumed to be graphite. Apparently, the astrosilicate-graphite combination is not emissive enough in the far infrared and submillimeter.

3.4 Optical properties variation

Variable submillimeter opacity

The models shown in Fig. 3.7 assume constant optical properties and are tuned to reproduce the correct $\mathcal{R}/A_\mathrm{V}$ for each SED, meaning that spectral shape variations in the modelled SEDs are solely driven by the ISRF. It is clear that the full range of spectral shapes exhibited by the observations (Fig. 3.7, top left) cannot be reproduced by ISRF variations alone. As mentioned in Section 3.3.2, if the dust optical properties are fixed the variations of $G_0^{\mathcal{R}}$ are only about half of what is needed to reproduce the data. We need dust with variable optical properties to reproduce the observations.

To correctly reproduce I_λ/A_V, one must apply a temperature-dependent correction to the ratio τ_0/A_V (more generally $\tau_\mathrm{sub}/A_\mathrm{V}$), or $C_\mathrm{sub}/C_\mathrm{V}$ (see Sect. 3.3.1). The value of this correction, $\mathcal{F} = A_\mathrm{V}^\mathrm{fit}/A_\mathrm{V}$, increases by $40-50\%$ between the warmest and coldest SEDs, independent of the model (as seen in Fig. 3.4); therefore, in the diffuse ISM, $\tau_\mathrm{sub}/A_\mathrm{V}$ varies by a factor $40-50\%$ between temperature extremes. When we consider only the SEDs within 1σ of the average, we obtain an estimate of the "typical" variation: $\sim 20\%$.

Now that in Sect. 3.3.2 we have devised another technique for comparing models and observation, we can test the validity of this estimate in Sect. 3.3.1. We modify the optical properties of the models used, in order to change the value of $\tau_\mathrm{sub}/A_\mathrm{V}$ by the desired amount, and we repeat the analysis of Sect. 3.3.2 on the modified models: the purpose is to see if the SED shape for the modified model reproduces the observations correctly. Since the analysis in Sect. 3.3.2 reproduces by construction the correct $\mathcal{R}/A_\mathrm{V}$, and this is a quantity that only depends on extinction, the simplest modification we can devise changes the submillimeter opacity leaving the extinction unchanged. With respect to the SED fitting procedure described in Sect. 3.3.1, this scenario corresponds to the case where $\mathcal{F}$ describes the correction to the fitted dust column density.

We modified the C11 and J13 models by multiplying the far infrared and submillimeter opacity of silicates and carbon by the same factor, independent of grain size, as shown in Fig. 3.8. This modification is a purely phenomenological artifice, not based on any physical properties of the materials. It is not intended as a physically-justified description of dust; rather, its purpose is to estimate the variations in submillimeter opacity that a physical model should attempt to reproduce.

We find that, to reproduce all the SEDs within 1σ of the average with the C11 model, we have to vary the vary its far infrared-submillimeter opacity between 1.1 and 1.3 times its standard value (between 1.0 and 1.4 to reproduce the full range of observations). The results are similar for the J13 model with scaling factors 0.9 and 1.1 for the $\pm 1\sigma$ range of SEDs (0.8 and 1.2 for the full range). Thus, in the case of fixed optical properties in extinction, the variations of far infrared-submillimeter opacity are $\sim 20\%$ ($40-50\%$) for the typical (full) range of diffuse ISM. These numerical values correspond well to the variations of the corrective factor $\mathcal{F}$ defined in Sect. 3.3.1.

Variable extinction cross-section, fixed albedo

We considered the case with fixed C_V and variable C_sub, but as we showed in Sect. 3.3.1, our constraints are on $C_\mathrm{sub}/C_\mathrm{V}$, not C_sub. Thus, in principle, modified dust models could also be adapted to fit the SED shape by keeping the submillimeter opacity fixed and varying the optical properties in extinction, as long as the dust albedo and the shape of the extinction curve are constant. In this scenario, all the variation in $C_\mathrm{sub}/C_\mathrm{V}$ comes from C_V alone, and $G_0^{\mathcal{R}}$ is biased since it is based on the assumption that C_V is constant across dust temperatures. To be exact, since the bias is equal to the variation in C_V, in this case $G_0^{\mathcal{R}}$ is exactly as biased as G_0^fit. Within Sect. 3.3.1, this would correspond to a scenario where there is no bias in the fit-derived dust mass, and the bias in $A_\mathrm{V}^\mathrm{fit}$ is uniquely due to the variability in C_V.

Of course, it is possible to fit the I_λ/A_V with models that have a modified submillimeter opacity

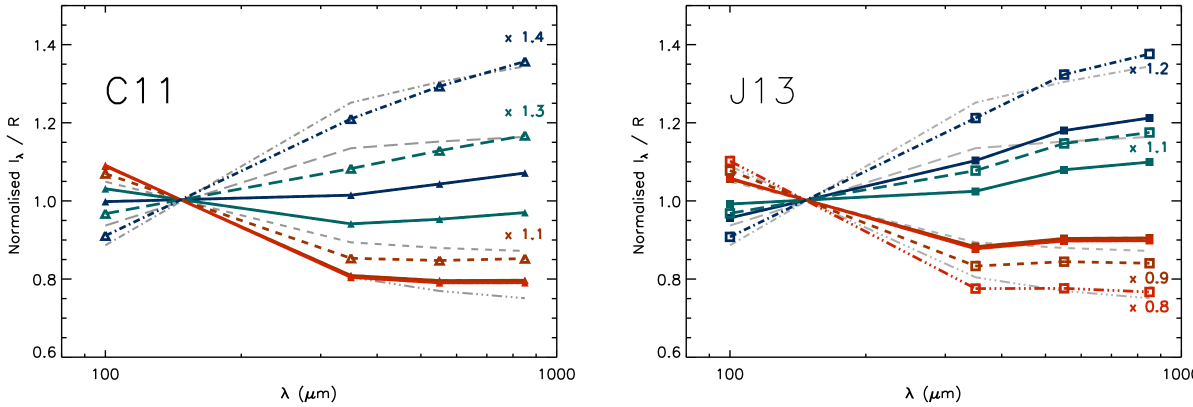

Fig. 3.8. Effect of variable $C_{\rm sub}$ on the synthetic observation from the C11 and J13 models, obtained as described in Sect. 3.3.2. The same five SEDs as Fig. 3.3 are shown, except the median SED, using the same colour and line style scheme. The normalisation is the same as Fig. 3.7. The observations are plotted in grey behind the models; the standard dust models are the solid lines with filled polygonal symbols and the modified dust models are the dashed lines with empty symbols. Numbers show the multiplicative factor applied to $C_{\rm sub}$.

and a modified extinction cross-section, as long as the overall change in $C_{\rm sub}/C_{\rm V}$ is the correct amount (20% variations in the "typical" diffuse ISM, up to $40-50$% between extremes). In this kind of scenario $G_0^{\mathcal{R}}$ is still biased, but less than $G_0^{\rm fit}$. Another lesson learned in comparing the above scenarios is that understanding the nature of the variations in the dust optical properties is essential to estimate the dust mass.

Variable extinction curve, albedo and G_0

If the dust optical properties in extinction are not fixed, it is very likely that the shape of the extinction curve and the albedo will present local variations as well. This further complicates the interpretation of our analysis, but the uncertainties introduced on the dust parameters can be estimated at least qualitatively. If we were to change the model albedo, the value of $\mathcal{R}/A_{\rm V}$ would no longer correspond to the observations unless we changed the ISRF intensity as well. A model thus modified would also give a different $G_0^{\mathcal{R}}$ value. Alternatively, it could be the hardness of the ISRF field that changes, rather than its intensity.

The description of the ISRF with the single parameter G_0 has of course never been more than a first-order approximation. The discussion above puts this assertion in perspective: the value of parameter $G_0^{\mathcal{R}}$ is actually dependent on the difference between the model albedo and the real one, as well as on the difference between the Mathis et al. (1983) spectrum and the actual radiation field. A more accurate statement would be that $G_0^{\mathcal{R}}$ is not a measure of G_0, but rather of $G_0 \cdot \langle 1 - Al \rangle$, meaning that the separation of radiation field and dust properties is only partial. Even in this case, the estimate $G_0^{\mathcal{R}}$ still has an advantage over $G_0^{\rm fit}$, which also assumes a fixed albedo. Also, it seems likely that variations in albedo have a limited range, imposed by the known chemical composition of grains and constrained by observations.

Effects of grain size distribution

The claim that variations of dust T across SEDs are too high to be accounted by ISRF alone may remind the reader that, everything else being equal, smaller dust grains are warmer (Ch. 1, Sect. 1.2.3). Furthermore, the size distribution of dust grains has a strong effect on extinction,

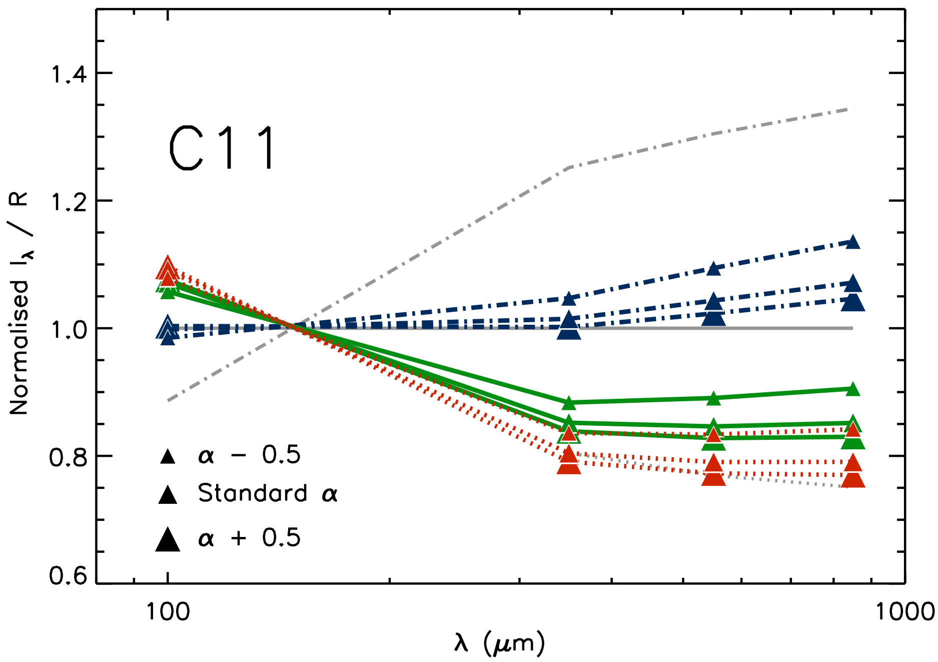

Fig. 3.9. Effect of the grain size distribution on $I_\lambda/\mathcal{R}$, as predicted by the C11 model. The SEDs shown are the coldest (blue dot-dashed line), the median (green solid line) and the warmest (red dotted line); normalisation is the same as per Fig. 3.7. The corresponding observations are plotted in grey behind the models. Larger symbols indicate larger average grain size, and smaller symbols indicate smaller average grain size (see text for details).

but not on the submillimeter opacity, which only depends on the total volume of the grains in the Rayleigh regime. It seems intuitive, therefore, that the grain size distribution must play an important role in the variation of $C_{\rm sub}/C_{\rm V}$. This scenario, however, is based on a subtly misleading assumption: while smaller grains are warmer *for a given ISRF intensity*, our estimate for the ISRF for each SED is not fixed: it is derived from the observed $I_\lambda/A_{\rm V}$ and it depends on the dust properties in extinction.

The meaning of this statement can be visualized with a simple model calculation. A coherent physical model of variations in dust size distribution is beyond the scope of this thesis; however, we can gain interesting qualitative insights from letting the size distribution vary in the C11 model[5].

In C11, grains larger than $\sim$ 10 nm are distributed according to a power law $n(a) \propto a^\alpha$, plus an exponential cutoff above $\sim$ 150 nm. The parameter that mainly controls the size distribution is the exponent of the power law, α, which is -2.8 for carbonaceous grains and -3.4 for silicate grains. We repeat the SED-fitting procedure described earlier varying α by -0.5 and $+0.5$ around its standard value: this changes $R_{\rm V}$ by -0.7 and $+1.0$, respectively; by comparison, (Fitzpatrick & Massa 2007) give ~ 0.3 as the typical 1-σ dispersion of $R_{\rm V}$ in the diffuse ISM.

We repeated the analysis of Sect. 3.3.2 on the modified model: the results are shown in Fig. 3.9. Varying the size distribution has a small impact on the dust SED, and the range of temperatures reproduced is smaller than that observed despite the large, possibly overestimated, span in α. This

[5]While this model does not fit the average $I_\lambda/A_{\rm V}$ as well as J13, it is still close enough to be useful for a differential analysis. Its homogeneous grains and constant optical properties allow us to modify the grain size distribution independent of optical properties. The study in Ysard et al. (2015), which uses the J13 model and more advanced modelling, includes the complex interplay of grain size and optical properties.

is a consequence of deriving the ISRF intensity from the observed radiance per unit extinction $\mathcal{R}/A_\mathrm{V}$: changing the size distribution modifies our estimate $G_0^\mathcal{R}$, so that models with smaller grains necessitate a weaker radiation field to satisfy those constraints. The decrease in $G_0^\mathcal{R}$ thus offsets the temperature increase due to size effects; in the particular case of the C11 model, it is even enough to make smaller grains slightly colder.

The details of the result presented in this section are likely to depend on the dust model and parametrization used. Still, varying the grain size distribution without its corresponding change in the dust optical properties is not likely to explain the observed variations of I_λ/A_V.

3.5 Summary

Fitting an SED with the dust models we used – DL07, C11 and J13 – returns biased values for the dust parameters $A_\mathrm{V}^\mathrm{fit}$ and G_0^fit. The bias can be divided in two parts:

- An error in the average values, which is model dependent and can be imputed to the optical properties of the dust model. DL07, with materials have the lowest submillimeter opacity among the models used, gives an $A_\mathrm{V}^\mathrm{fit}$ which is $\times 1.9$ the measured A_V. On the contrary, J13, which has the highest submillimeter opacity, is the only models to correctly reproduce the average A_V.
- A temperature dependent trend where models attribute higher $A_\mathrm{V}^\mathrm{fit}$ to colder dust. This is common to all models and is due to the fact that the models use fixed optical constants.

It can be shown that, to reproduce the correct A_V, the $\tau_\mathrm{sub}/A_\mathrm{V}$ for dust in different zones must show variations of the order of 20% (as high as 50% in extreme cases).

Since G_0^fit is biased we introduced an alternative G_0 estimator: $G_0^\mathcal{R}$, which can be calculated from the dust $\mathcal{R}/A_\mathrm{V}$. This estimator is independent of the dust far infrared and submillimeter properties, which makes it generally less biased than G_0^fit: $G_0^\mathcal{R}$ and G_0^fit are equivalent in the extreme case where the dust optical properties are fixed in emission, and only change in extinction. While still model dependent, $G_0^\mathcal{R}$ is shows less variation than G_0^fit across models.

If one uses $G_0^\mathcal{R}$ as a parameter in the dust model, the output SEDs have the correct A_V by construction, but the wrong SED shape. To correctly reproduce the observed spectra, the dust $\tau_\mathrm{sub}/A_\mathrm{V}$ must have variations of 20% (as high as 50% in extreme cases) across different zones, consistently with the analysis above.

Part III

Dust evolution and polarization

Chapter 4

Study of the variations of optical-to-submm polarization ratios: alignment or evolution effects?

Contents

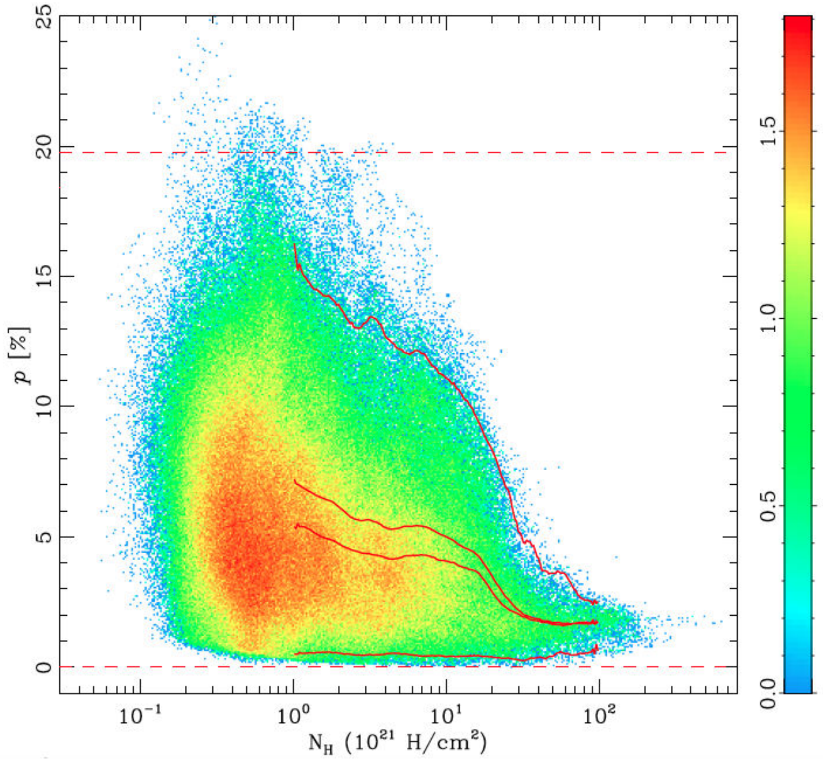

Fig. 4.1. Distribution of $P_{\rm sub}/I$ as a function of $N_{\rm H}$ over the whole sky, as obtained from the *Planck* data. The dashed red lines represent polarizations of 0% and 19.8% (the maximum value of $P_{\rm sub}/I$ as found by Planck Collaboration Int. XIX 2015). From Planck Collaboration Int. XIX (2015).

4.1 Context and motivation

Observations of polarization in extinction have provided us with a great wealth of information on dust and on the Galactic magnetic field, as seen in Ch. 1, Sect. 1.3.2. Now, thanks to *Planck*, we have all-sky maps of polarized dust emission: what new insight does this offer? What more can we learn by comparing polarized extinction and emission, as we compared unpolarized emission and extinction in Ch. 3?

The *Planck* collaboration produced, among other things, a full-sky map of polarized dust emission: a map of the polarization fraction $P_{\rm sub}/I$ at 353 GHz, at a resolution of 1°, has been published in Planck Collaboration Int. XIX (2015). Reaching values as high at 20% at the lowest column densities, the maximum $P_{\rm sub}/I$ slowly decreases up to $N_{\rm H} \sim 10^{22}$ (equivalent to $A_{\rm V} \sim 5$), while at higher $N_{\rm H}$ the drop accelerates (Fig. 4.1). As we have seen, the dust polarization fraction depends on the interplay of three things: the orientation of the magnetic field, the alignment efficiency of grains and the optical properties of dust, therefore its evolution (Ch. 1, Sect. 1.3.2). What do we understand of the role played by each factor?

Polarization efficiency: the role of the magnetic field

Once again, before describing my own work I devote one section to explaining the context of the research, using the results of a different *Planck* paper.

A study of the relation between magnetic field orientation and polarization fraction has been published in Planck Collaboration Int. XX (2015): in this paper it is shown that the slow part of the decrease in $N_{\rm H}$ is compatible with a pure magnetic field origin, at least up to $N_{\rm H} \sim 2 \cdot 10^{22}$

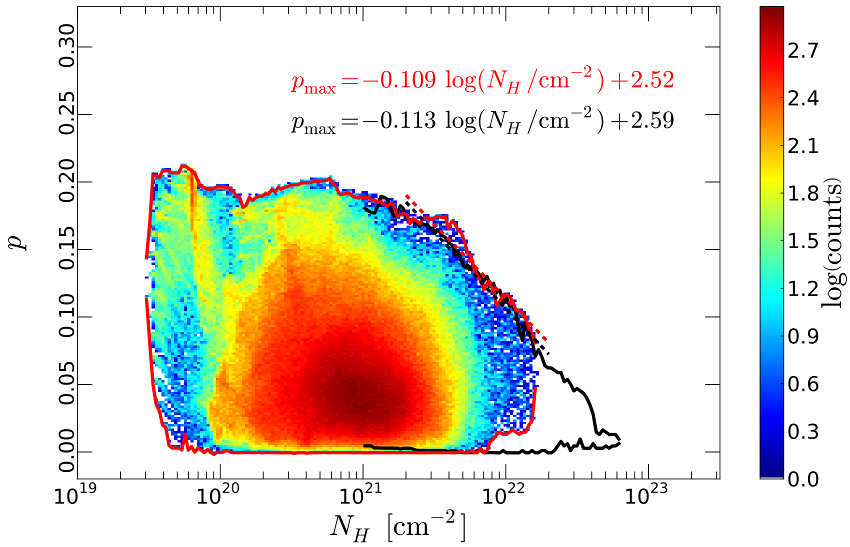

Fig. 4.2. Comparison of P_{sub}/I and N_{H} from MHD simulations and as observed by *Planck*. Simulations are in color scale and their envelope is shown as a solid red line; the solid black line shows the envelope for observations with $N_{\mathrm{H}} > 10^{21}$ H cm^{-2} (for lower columns densities, the zero point of *Planck* maps and the background/foreground contamination are expected to play significant roles). Linear fits of the upper envelope in the range $2\,10^{21} < N_{\mathrm{H}} < 2\,10^{22}$ are shown for both simulations (red, dashed line) and observations (black, dashed line). From Planck Collaboration Int. XX (2015).

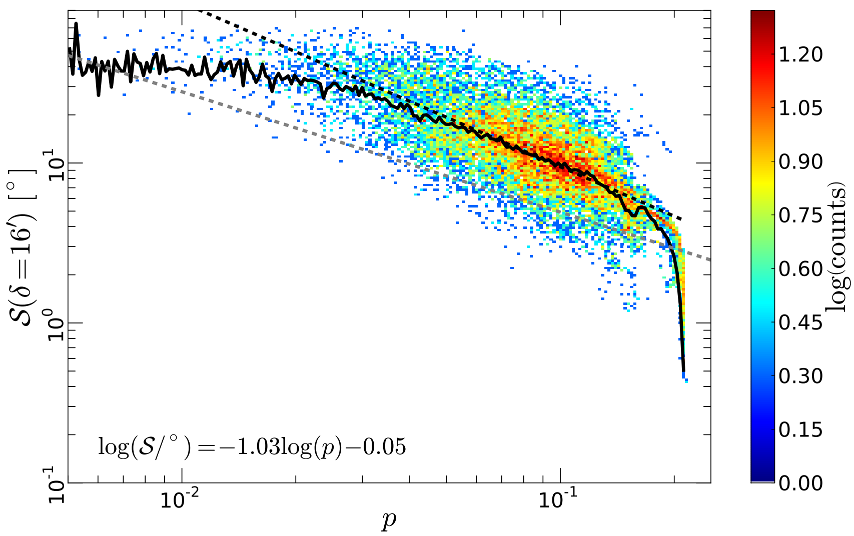

Fig. 4.3. Results for P_{sub}/I and the angle dispersion S from MHD simulations. The solid black line represents the mean value of S. The dashed black line is a linear fit to the simulations; the grey dashed line is the same fit, but on the *Planck* observational data. From Planck Collaboration Int. XX (2015).

cm^{-2}. This is visible in Fig. 4.2, which shows the global results of MHD simulations (in color, with the envelope in red) compared to the envelope for the *Planck* observations (in black). In the range of $N_{\rm H}$ where both simulations and observation are available, 10^{21} cm^{-2} $- 2 \cdot 10^{22}$ cm^{-2}, they show a remarkable agreement. The magnetic field orientation can influence the observed polarization in two different ways, as shown in 1, Sect. 1.3.2: a factor $\cos^2\gamma$ due to the angle γ between the ordered component of the magnetic field and the plane of the sky, and a factor F describing the line-of-sight and beam depolarization due to the disordered component of the field. The *Planck* collaboration has no independent all-sky measurement of the angle γ; however, Planck Collaboration Int. XX (2015) provides an estimate of the disorder in the field.

The polarization angle ψ gives the direction of the magnetic field projected on the plane of the sky: the *angle dispersion function* S is the quadratic average of the variations of ψ. For a given pixel x, we define:

$$S(x,\delta) = \sqrt{\frac{1}{N}\sum_{i=1}^{N}(\Delta\psi_{xi})^2} \tag{4.1}$$

where the sum is on the N pixels comprised in an annulus between the angular distances δ and $\delta + \Delta\delta$ from x, and $\Delta\psi_{xi}$ is the difference in ψ between the pixels x and i. The formula for $\Delta\psi_{xi}$ uses the Stokes parameters is $\Delta\psi_{xi} = \arctan(Q_iU_x - Q_xU_i, Q_iQ_x + U_iU_x)$. In regions with a well-ordered magnetic field one will have $S \sim 0°$, while in regions dominated by noise S converges to $\pi/\sqrt{12} \sim 52°$; S also increases with δ, as the coherence is lost when getting too far from the central point Planck Collaboration Int. XXXII (2014). has also demonstrated that S incorporates some projection effects related to the angle γ of the turbulent magnetic field with the plane of the sky.

The same MHD simulations that reproduce the $P_{\rm sub}/I$ vs. $N_{\rm H}$ relation of Fig. 4.2 present the correlation between S and $P_{\rm sub}/I$ shown in Fig. 4.3. A linear fit to the simulations, shown as a dashed black line, is a factor $\sim 2-3$ higher than the same fit operated on the *Planck* observations, shown as a dashed gray line: observations show less turbulence, as traced by S, than what is necessary in MHD simulations to explain the $P_{\rm sub}/I$ vs. $N_{\rm H}$ anticorrelation. It is therefore reasonable to search for complementary mechanisms responsible for the lower observed $P_{\rm sub}/I$ at a given S, such as grain alignment and dust evolution.

Polarization efficiency: the role of grain alignment

The advent of the RATs theory of grain alignment (Ch. 1, Sect. 1.3.2) has motivated many studies on the modulation of the polarization fraction by the grain alignment. One of its distinguishing characteristic is that it connects alignment efficiency with ISRF intensity. Whittet et al. (2008) show how the relation between $A_{\rm V}$ and the infrared p/τ in molecular clouds can be explained by a model that account only for (RATs-driven) alignment, with no contribution from magnetic fields or dust evolution. Another study by Andersson & Potter (2007) tests the prediction of RATs theory that the size threshold for dust alignment increases in molecular clouds, as the impinging ISRF is damped. They use the wavelength of maximum polarization in extinction $\lambda_{\rm max}$ as a tracer of alignment (Ch. 1, Sect. 1.3.2), since it is proportional to the typical size of aligned grains and therefore it is sensitive to the alignment size threshold. An increase in $\lambda_{\rm max}$ may also signify grain growth, but no correlation was found with the unpolarized grain size tracer $R_{\rm V}$. But we should remember that $\lambda_{\rm max}$ also depends on the optical properties of aligned grains.

Polarization efficiency: the role of dust evolution

In principle it is expected that grain growth through coagulation and mantle accretion will affect the dust opacity, and therefore $P_{\rm sub}$ as well as I. In this perspective, significant progresses have been made in the modeling of the variations of the total intensity (Köhler et al. 2012), but the consistent modeling of total and polarized intensity variations from the diffuse ISM to dense clouds is beyond our current capacities. We intend to start to explore this possibility by comparing polarization in extinction and in emission, tracing changes in dust optical properties not unlike we did in the previous chapter with unpolarized observables. However, compared to the complexity of the matter both from the modeling and data analysis points of view, we are only just beginning.

Problematics

Thanks to the large statistics of the *Planck* data, the scientific community is beginning to better understand the large-scale variations of the polarization fraction. We better understand the role played by the magnetic field (Planck Collaboration Int. XXII 2015), but there is not enough turbulence to invoke it as the sole player (Planck Collaboration Int. XX 2015). The reasons for the large drop in polarization at high N_{H} is probably due to the loss of dust alignment (Jones et al. 2015), but the impact of dust evolution, clearly constrained from studies of the total intensity, can not be ignored. In this chapter, we use data spanning a range of A_{V}s that reach up to the beginning in polarization drop, and we will study how to separate the different factors to gather a better understanding of the observed drop in the polarization fractions.

4.2 Data

Our work combines, for the same line of sights, starlight polarization with dust polarization emission at 353 GHz from *Planck*.

4.2.1 V-band observations

We referred to the published literature to find extinction and polarization data in the visible. Most of our data points are from Andersson & Potter (2007), who, in a polarimetric study of the Coalsack nebula, collected for comparison purpose the data for several other clouds from the literature (Tab. 4.1). In order to minimize systematic effects from different fitting procedures, Andersson & Potter (2007) did not use the fit results to the extinction and polarization curves from the literature, but they used the photometric and polarimetric data to conduct their own fits. The extinction parameters were recalculated after checking and – where necessary – updating the stellar spectral classifications, using additional visual and NIR photometry from the Tycho database (Høg et al. 2000) and the 2MASS survey[1]. Polarization data were fitted with a Serkowski curve with $K = 1.15$ (Ch. 1, Sect. 1.3.2, Eq. 1.20), or leaving K as a free parameter if an F-test justified the additional parameter at the 90% level or more. A few stars were excluded from the analysis because, during the process of reanalysing the data, some of their observational parameters turned out to have unphysical values or to be incoherent with the values in the source paper. A combination of Tycho and 2MASS photometry and *Hipparcos* parallax data was used to select those stars at a distance larger than the one estimated for the cloud.[2]

The star database for Andersson & Potter (2007), retrieved from the *Vizier* online database[3], had unfortunately some missing data; specifically, we did not have the values of the uncertainties in ψ_{V} for the Ophiuchus from Vrba et al. (1993). To integrate the data we retrieved the polarization angles in the $UBGRI$ bands directly from Vrba et al. (1993) (not all bands are available for all

[1] http://www.ipac.caltech.edu/2mass/

[2] The *Hipparcos* database contains trigonometric parallaxes for a limited number of lines of sight, while the more complete Tycho and 2MASS databases contain no explicit distance information. A comparison of distance estimates from *Hipparcos* with reddening extracted from Tycho and 2MASS provides the threshold A_{V} above which stars are likely to be behind the cloud.

[3] http://vizier.u-strasbg.fr

Cloud	l	b	Reference
Chamaeleon	297°	-15°.5	(Whittet 1992; Covino et al. 1997 and refs. therein)
Musca	301°	-8°.0	Arnal et al. (1993)
Ophiuchus	354°	15°.0	(Whittet 1992; Vrba et al. 1993 and refs. therein)
R Coronae Australis (R CrA)	0°	-19°.5	(Whittet 1992 and refs. therein)
Taurus	174°	-14°.0	(Whittet 1992; Whittet et al. 2001b and refs. therein)

Table 4.1. Clouds from Andersson & Potter (2007) used in this chapter, with their approximate position on the sky.

stars); we used the value averaged across bands as our angle and the variance as uncertainty. Those stars where the standard deviation was greater than 7° were excluded, as it usually meant that data in different bands were not compatible.

To increase the statistics, we also took data from Anderson et al. (1996), a study on star polarization which uses polarimetric data from 155 nm to 1 μm. The star sample from this study are chosen to have E(B-V) < 1.5 and they span the Galactic plane, probing lines of sight with diverse chemical composition and morphology. The fit of the polarization curve was of the form $p_{\max}\, e^{-K_{\lambda_{\max}}\, ln^2(\lambda/\lambda_{\max})}$, where $K_{\lambda_{\max}}$ is a linear function of $\lambda_{\max}$ as per Wilking et al. (1982)[4]. In some stars, the polarization angle shows a marked trend with wavelength, which may be an indicator of intrinsic polarization; these stars have been excluded from the sample.

The values of $p_{\rm V}$ for all lines of sight were obtained from $p_{\max}$, $\lambda_{\max}$ and (where the Wilking fit had been used) K. Since the correlations between parameters were not available, uncertainties were considered independent during propagation and the error bars on $p_{\rm V}$ may be somewhat imprecise; however, $p_{\rm V}$ is not as important as $p_{\max}$ in our analysis.

4.2.2 *Planck* maps

We use the full mission 353 GHz (850 μm) maps of the second *Planck* public data release[5]. We did not use any other frequency because of their lower S/N. The data consists of 10 all-sky maps, each devoted to a different quantity: the Stokes parameters I, Q and U, the number of hits, the variances of the Stokes parameters II, QQ and UU, and the covariances IQ, IU and QU. Each map is a HEALPix vector (Górski et al. 2005) in NESTED ordering and Galactic coordinates; they have a pixelization $N_{\rm side} = 2048$ for a total of $12 \cdot 2048^2 = 50\,331\,648$ pixels with $1'.7$ side lengths, so that the beam of the instrument (FWHM $\sim 5'$) is well-sampled. The maps (except hits) are in units of $\rm K_{CMB}$, and are converted to MJy/sr, with a conversion factor of ~ 287 at 353 GHz (Planck Collaboration Int. IX 2014)[6].

To obtain the value of I, Q and U at the position of each star and increase the S/N, we averaged the values for the Stokes parameters on a Gaussian PSF centered on the star coordinates and with a FWHM of 5' (as was done in Planck Collaboration Int. XXI 2015). The smoothing of Q and U is not trivial: according to the HEALPix convention, the local reference frame for polarization is that of the local meridian and parallel. Before averaging Q and U within a beam, the doublet (Q, U) must be rotated locally to bring the value of each pixel to the reference frame of the center of the beam. The situation is similar for the parameters of the covariance matrix. For a presentation

[4] Anderson et al. (1996) write that they use the Wilking et al. (1982) formula for polarization, but they do not mention the parameters they use to obtain $K_{\lambda_{\max}}$. If we assume that they use the parameters measured in Wilking et al. (1982), then $K_\lambda = -0.10 + 1.86\,\lambda_{\max}$

[5] http://irsa.ipac.caltech.edu/data/Planck/release_2/all-sky-maps/

[6] The conversion factor quoted in Planck Collaboration Int. IX (2014) is 287.45, while the value used in our codes was the slightly older value of 287.2262. Since the two values differ by less than 1‰, the effects on our results are negligible.

of the method, see Appendix A.1 of Planck Collaboration Int. XIX (2015). With the value of the submillimeter Q and U for all the lines of sight, we calculated P_{sub} and debiased it with the conventional method: $P_{\text{deb}} = \sqrt{P_{\text{bias}}^2 - \sigma_P^2}$ (*e.g.*, Simmons & Stewart 1985). We did not apply the more recent debiasing method like Plaszczynski et al. (2014) and Montier et al. (2015) because the noise, therefore the bias, is low in the environments we are studying here once the data is smoothed. There was no need to apply CMB and CIB corrections, which are negligible at this wavelength and for this range of column densities.

We also calculated the polarization angle dispersion function S at the position of each star. We smoothed the (I, Q, U) triplet with the *ISMOOTHING.PRO* IDL code to increase S/N, using a Gaussian PSF with 5' FWHM, bringing the maps to a 7' resolution. The maps thus obtained are oversampled (4 pixels per beam), so we also degrade the pixelization of the Q and U maps to $N_{\text{side}} = 1024$ to get closer to the Nyquist criterion, as in Planck Collaboration Int. XIX (2015). The dispersion function S is then computed for the pixel containing the star, at a lag $\delta = 5$'.

We also used other *Planck* dust maps – temperature T, optical depth τ_{850} and radiance $\mathcal{R}$ – used in Planck Collaboration XI (2014), and although they do not play a role in our main results, they were used for several checks and they will have a larger role in the continuation of this work (see Sect. 4.6).

4.2.3 Sightline selection

A central part of our work will be the comparison between P_{sub} and p_{V}. This unfortunately adds, to the issues typical of polarization studies (depolarization), also the main issue of dust emission-vs-extinction studies: background emission.

An extinction measure that uses a star as a source only probes the matter in front of the star itself, a limitation which does not apply to emission – especially in the submillimeter, where the ISM is transparent[7].

In presence of a background to the star, the total intensity I measures systematically more dust than what is observed in the optical to the star. The effect on P_{sub} can be more complex: polarized emission may be overestimated, like I, due to the more dust observed, but it may also be underestimated because there might be more line-of-sight depolarization. The answer ultimately depends on the structure of the magnetized ISM: in the limiting case where the magnetic field is uniform, $P_{\text{sub}} \propto \tau_{\text{sub}}$; in the case where magnetic field orientation changes a lot of times on the line of sight, one expects $P_{\text{sub}} \propto \sqrt{\tau_{\text{sub}}}$, as is observed in some molecular clouds (Jones et al. 1992). Realistic cases will be more complex. For all of the above reasons, we need to carefully select the lines of sight with little to no background.

After completing the star database for the data analysis we operated a further selection on the lines of sight to discard those where the *Planck* data is likely have significant background contamination. For this we use the same kind of selection process as in Planck Collaboration Int. XXI (2015). The first step in the selection process is to exclude the stars that are too close to the Galactic plane, so we discarded all of the Coalsack nebula and all stars with a Galactic latitude of less than 2°.

Another criterion is the consistency of the polarization angles in extinction and in emission, which ought to be orthogonal if they come from the same grains: we excluded those lines of sight where the two angle are not orthogonal, with a tolerance 3σ or 10°, whichever is smaller. The ψ_{V} from Anderson et al. (1996) are given without uncertainties: in those cases, we attribute them an uncertainty of zero. Since *Planck* angle uncertainties are usually larger than V band angle uncertainties, this should not make a large difference.

[7]The analysis in Ch. 3 solves the issue by measuring the extinction on QSOs, which are certain to have no background of Galactic origin.

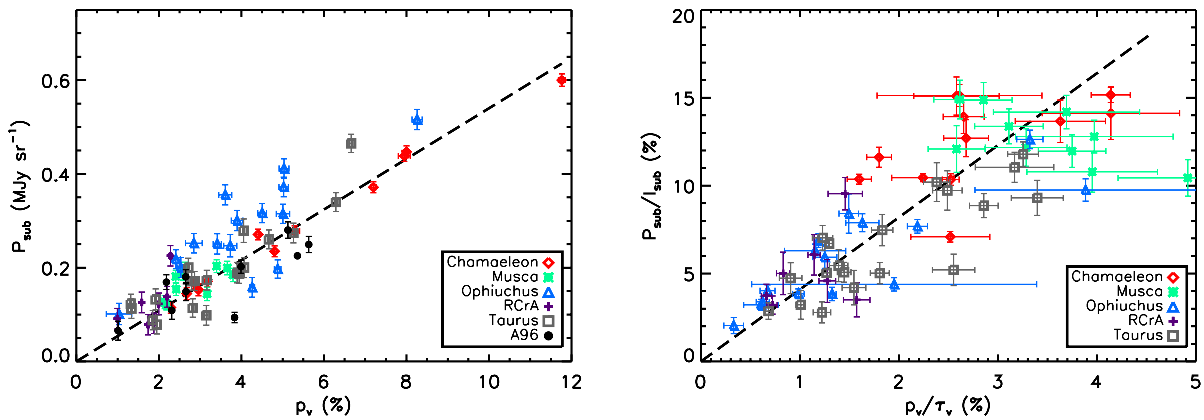

Fig. 4.4. Comparison of polarization in extinction and in emission: P_{sub} vs. p_{V} (left) and P_{sub}/I vs. $p_{\mathrm{V}}/\tau_{\mathrm{V}}$ (right), for the lines of sight in our possess. The solid lines represent the average emission-to-extinction ratios obtained in Planck Collaboration Int. XXI (2015): 5.4 MJy sr^{-1} mag^{-1} for $R_{\mathrm{P/p}}$ and 4.1 for $\frac{P_{\mathrm{sub}}/I}{p_{\mathrm{V}}/\tau_{\mathrm{V}}}$.

Yet another criterion would be the comparison of column density (or reddening E(B-V) to the star) to the one estimated from the dust optical depth at 353 GHz τ_{FIR} using Eq. 3.1. However this last method, very efficient in identifying background contamination in the diffuse ISM, is not very constraining in molecular clouds, where an increase in the dust optical depth at 353 GHz may derive not from the presence of a background to the star, but also from heightened submillimeter emissivity associated with dust evolution. Considering that the submillimeter opacity in molecular clouds may increase up to a factor ~ 3, we chose to exclude clear outliers by removing those stars with a ratio of column densities higher than 3.

While none of the selection procedure we use can exclude all of the contaminated sightlines, the combined use of them – together with the selection already operated by Andersson & Potter (2007) – is likely to be more robust. We give further consideration to the purity of selection in Sect. 4.6.

4.3 Data analysis

4.3.1 Correlations in data

The correlation between polarization observables in extinction and in emission is shown for our selected sample in Fig. 4.4. The correlation is good between the two different bands, both for the polarized intensity and for the polarization fraction, although the latter presents a larger scatter (as in Planck Collaboration Int. XXI 2015) since it also includes the variations in the I/A_{V} ratio. The plots are in good agreement with the results of Planck Collaboration Int. XXI (2015)[8]: an average value for the polarization ratio $R_{\mathrm{P/p}} = P_{\mathrm{sub}}/p_{\mathrm{V}}$ of 5.4 MJy sr^{-1} mag^{-1} and a value of 4.1 for $\frac{P_{\mathrm{sub}}/I}{p_{\mathrm{V}}/\tau_{\mathrm{V}}}$, which are shown as solid black lines in the plot. The general good agreement between these results and those of Planck Collaboration Int. XXI (2015) – which concentrated on the diffuse ISM where the selection is more efficient – suggests that our selection was efficient.

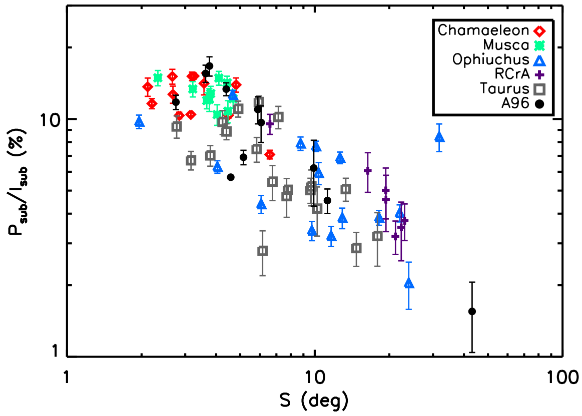

Fig. 4.5. Plot of $P_{\rm sub}/I$ vs the angle dispersion S.

Effect of the magnetic field: the angle structure function S

Fig. 4.5 shows the typical anticorrelation between $P_{\rm sub}/I$ and S, similar to what is observed with the full-sky statistics of *Planck* (Planck Collaboration Int. XIX 2015) or in MHD simulations (Planck Collaboration Int. XX 2015). This correlation is usually interpreted as the effect of the depolarization, on the line of sight and within the beam, due to an irregular ("tangled") magnetic field (*e.g.*, Planck Collaboration Int. XIX 2015). The dust optical properties and the alignment efficiency have no effect, at first order, on the direction of polarization, although variations of alignment on the line of sight may have some influence. In particular, Planck Collaboration Int. XX (2015) shows how a model can reproduce the $P_{\rm sub}/I$ vs. S relation just using the magnetic field tangling, keeping the dust optical properties and alignment fixed. This strongly suggests that what we observe in Fig. 4.5 is the role of magnetic field tangling in the variations of $P_{\rm sub}/I$. The figure, however, also shows that the magnetic field turbulence is not the only process at play: there is not a tight correlation between the polarization fraction and the angle dispersion; rather, the values of $P_{\rm sub}/I$ are dispersed in an envelope which depends on S. This suggests that some other parameters exist that decrease the polarization efficiency aside from S.

Effect of alignment: $\lambda_{\rm max}$

Fig. 4.6 shows, for our data sample, how the polarization fractions in extinction and emission relate to $\lambda_{\rm max}$. This is consistent with $\lambda_{\rm max}$ being a tracer of the grain alignment efficiency, and more precisely of the size threshold above which grains are aligned: lines of sight with larger values of $\lambda_{\rm max}$ would also have a smaller mass of aligned grains (assuming similar size distributions), and therefore a lower polarization fraction on average.

Just like Fig. 4.1 and 4.5, Fig. 4.6 shows envelope-like distributions, demonstrating that the polarization fractions are influenced by depolarizing factors other than alignment efficiency (this is not surpising, given that in the previous section we showed the role played by the magnetic field).

The interplay between the magnetic field and dust alignment can be better understood by remembering the discussion on the RRF in Ch. 1, Sect. 1.3.2, Eq. 1.18 and following: the effect of grain alignment is resumed in the R factor of Eq. 1.19, while magnetic field acts on factors $\cos(\gamma)^2$ (smooth field component) and F (turbulent field component).

[8] An early version of the analysis presented in Planck Collaboration Int. XXI (2015) was the subject of an internship at IAS during my master, in which occasion I obtained the value of $R_{\rm S/V}$ for the clouds of Chamaelon, Musca and Taurus.

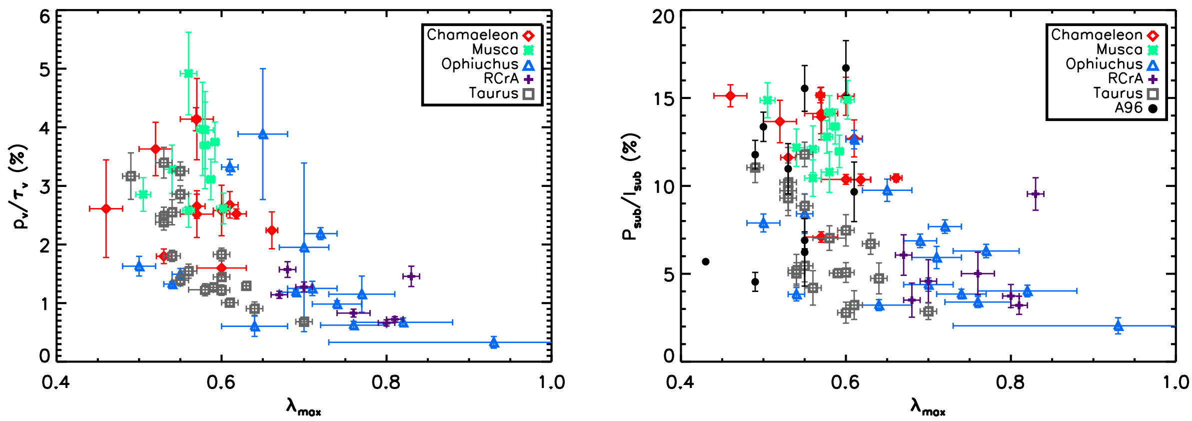

Fig. 4.6. The polarization fractions p_V/τ_V (left) and P_{sub}/I (right) as a function of λ_{max}.

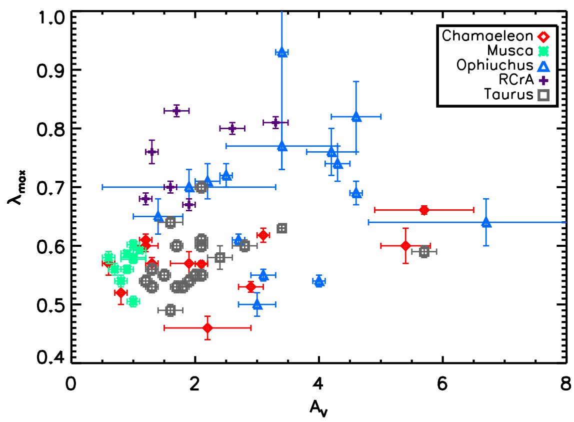

Fig. 4.7. λ_{max} as a function of A_V in our sample.

As we mentioned in 4.1, many studies of the alignment efficiency are made within the context of the RAT theory, according to which the dust alignment efficiency through radiative torques should scale with the radiation field intensity (Lazarian & Hoang 2007). Therefore, we expect tracers of dust alignment, such as λ_{max}, to correlate both with A_V and with the dust temperature or the radiation field intensity G_0. This kind of correlation was explored in Andersson & Potter (2007), where λ_{max} was measured in several dark clouds.

Fig. 4.7 shows that, in our data set (mostly coincident with that of Andersson & Potter (2007)), the correlation of λ_{max} with A_V is only a general trend, with a large scatter. This is not unexpected, as A_V is an imperfect estimate for the true extinction seen by photons flying from stars to the dust grains observed on the line is sight (Andersson & Potter 2007; see also their Figs. 6, 11 and 12). To improve on this estimate, the authors used the 60 μm to 100 μm *IRAS* color as an estimate of dust temperature, and concentrated on the lines of sight where A_V is anti-correlated with I_{60}/I_{100}, making it a more reliable estimate of ISRF attenuation. With this correction, Andersson & Potter (2007) claimed that λ_{max} was linearly correlated with the radiation environment of the grains. Today, however, the *Planck* survey offers more reliable estimators of the ISRF. Here we correlate λ_{max} with two new estimators: the grain temperature T measured with *Planck*, and the estimator for the radiation field intensity we derived in chapter 3, $G_0^{\mathcal{R}} \propto \mathcal{R}/A_V$.

Similarly to (Planck Collaboration Int. XIX 2015), and unlike Andersson & Potter (2007), we

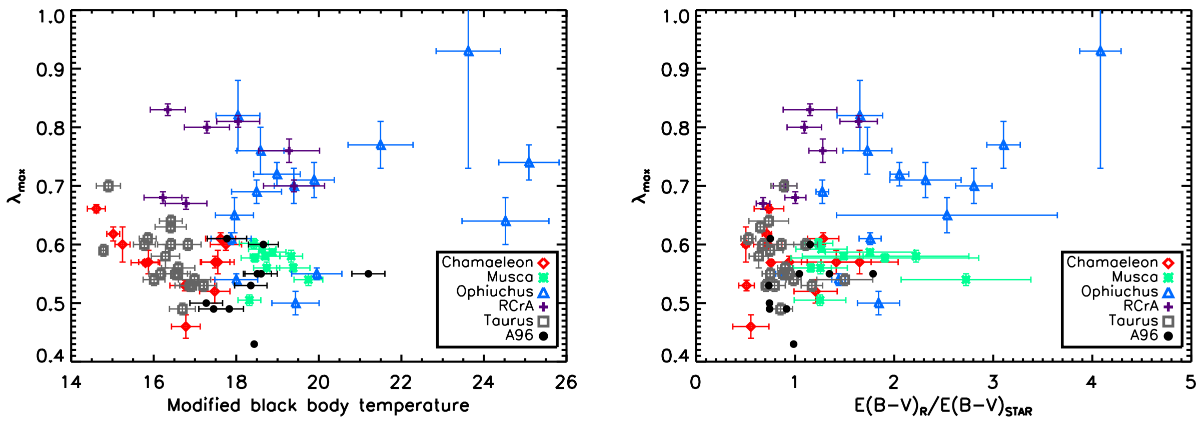

Fig. 4.8. The relation between $\lambda_{\max}$ and dust temperature (left) and between $\lambda_{\max}$ and the ISRF intensity estimator $G_0^{\mathcal{R}}$ (right) are used to searching for a relation between grain alignment and ISRF intensity.

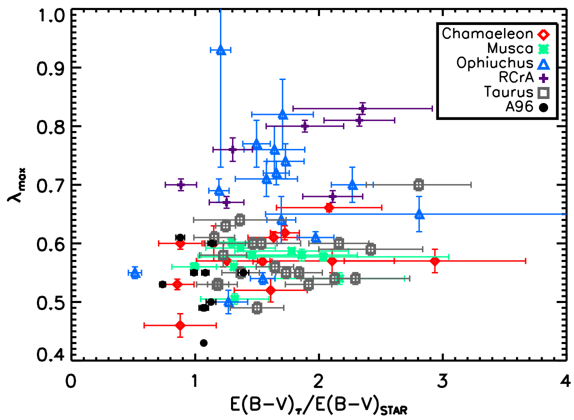

Fig. 4.9. $\lambda_{\max}$ as a function of dust evolution (represented as ratio of smm to V opacity).

do not see any trend in our data set indicating that grains are aligned by radiative torques (Fig. 4.8). We conclude that the process responsible for the variation in $\lambda_{\max}$ does not seem to be affected by the radiation field intensity or by the grain temperature, and only marginally by dust extinction.

Effects of evolution

To test the presence of any relation between polarization and dust evolution, we decided to use the dust evolution tracer established in Chap. 4 and implicit in all the studies of dust evolution in molecular clouds: the ratio $E(B-V)_{\mathrm{S}}/E(B-V)$ of dust opacity in the submillimeter and in the visible. We use Eq. 3.1 to obtain $E(B-V)_{\mathrm{S}}$ from τ_{FIR}; the ratio of the submillimeter E(B-V) to the one measured on the star is a measure of dust evolution. As shown in Fig. 4.9, the data show what might be a slight correlation between $\lambda_{\max}$ and dust evolution, although this is difficult to judge due to the large scatter in data (Pearson correlation coefficient: 0.28, as calculated with the *CORRELATE.PRO* IDL code)[9]. We ran some more statistical tests on $\lambda_{\max}$ and the ratio

[9]We should bear in mind that τ_{FIR} may include emission from behind the star: although several steps have been taken to minimize this (Sect. 4.2.1), there may be residual contamination, which could introduce a bias on the average value of the τ_{FIR}-derived E(B-V). Since contamination is not expected to depend on $\lambda_{\max}$, the aforementioned should

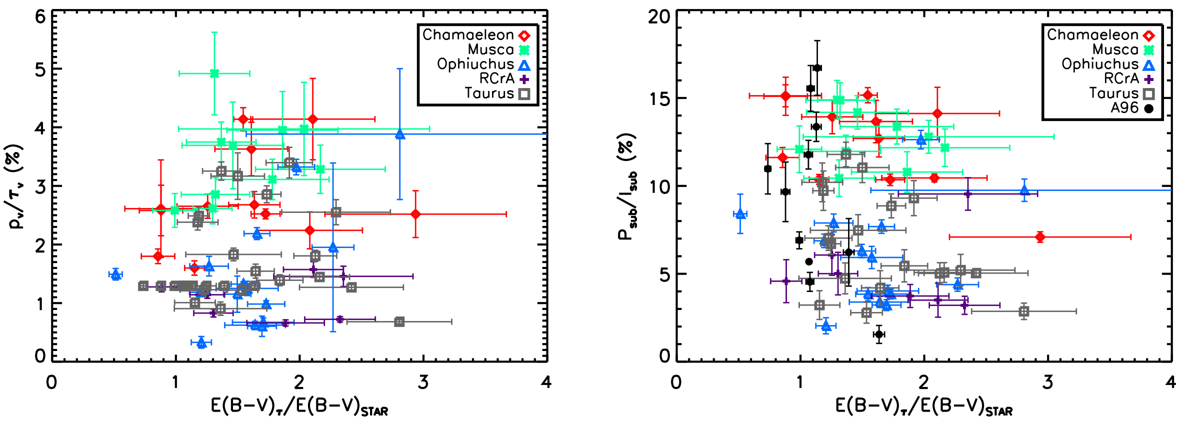

Fig. 4.10. Polarization fraction in extinction (left) and emission (right) as a function of the dust evolution parameter $E(B-V)_{\mathrm{S}}/E(B-V)$.

of submillimeter-to-V opacity (see Appendix D): while a linear fit on binned data shows relevant correlation, a k-test gives negative results. We conclude that the evidence for correlation is too weak to warrant further interest.

In Fig. 4.10 we show the polarization fractions in extinction (left) and emission (right) as a function of a the tracer of dust evolution: $E(B-V)_{\mathrm{S}}/E(B-V)$. No trends emerge, although the large error bars (due to the large uncertainties in the value E(B-V) from stellar sources) mean that no firm conclusions can be drawn on the presence or absence of a physical relation.

Modeling the effects of dust evolution on the polarization observables is a long work. It requires a precise modellng of the grain coagulation and accretion, as well as rigorous radiative transfer to disentangle the measure of dust optical properties from the radiative environment. For this reason, we left them for last and decided to concentrate first on easier fare.

4.3.2 $R_{\mathrm{P/p}}$ as a way of removing the effect of the magnetic field

Since both $p_{\mathrm{V}}/A_{\mathrm{V}}$ and P_{sub}/I show a marked dependence on magnetic field orientation and grain alignment, it would be interesting to have a way of separating the two effects. In Sect. 4.3 we mentioned the polarization ratio $R_{\mathrm{P/p}} = P_{\mathrm{sub}}/p_{\mathrm{V}}$ (MJy sr^{-1}), defined in Planck Collaboration Int. XXI (2015); it is a ratio similar to I/A_{V}, but in polarization. Polarization in the visible and in the submillimeter are affected by magnetic field and alignment in roughly the same way (*e.g.*, Martin 2007). The emission to extinction polarization ratio $R_{\mathrm{P/p}}$, therefore, should trace mainly the aligned dust population, its distribution of sizes, shapes and optical properties. While we do not yet have simulations at the two wavelengths to confirm this, the tight correlation between P_{sub} and p_{V} seen in Planck Collaboration Int. XXI (2015) and in Fig. 4.4 lends credibility to the idea. This is however only true as a first-order approximation: second-order effects may come, for instance, from the fact that polarization properties in the *Planck* bands are related to the absorption cross-section in the submillimeter, and not very sensitive to grain size, while there is an important contribution from scattering and not only absorption in the V band, which is very sensitive to the grain size.

Dependence of $R_{\mathrm{P/p}}$ with the magnetic field Fig 4.11 shows that the polarization ratio $R_{\mathrm{P/p}}$ does not depend on the angle structure function S. This indicates that at least the main part of the

not introduce any spurious correlations between λ_{max} and dust evolution; however, it would increase the scatter in the data making it more difficult to detect an existing correlation. For this reason, further checks of contamination should be done.

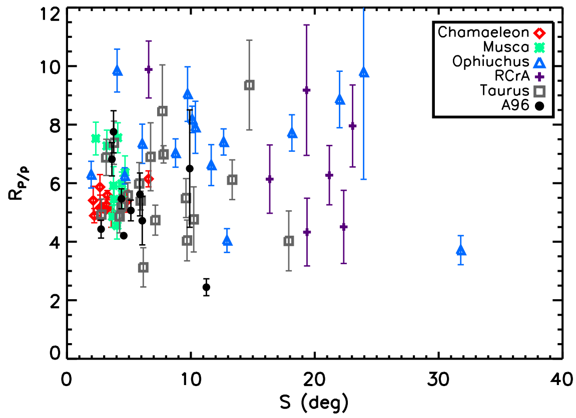

Fig. 4.11. Polarization ratio $R_{\mathrm{P/p}}$ as a function of the angle dispersion function S: no correlation is evident.

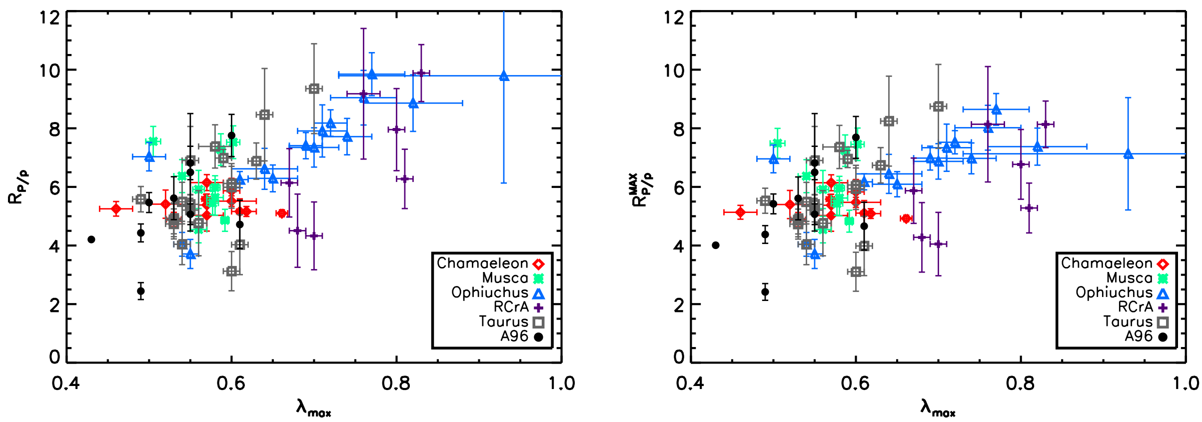

Fig. 4.12. Polarization ratio $R_{\mathrm{P/p}}$ as a function of λ_{max} (left): the correlation between the two quantities is noticeable, although rather shallow. We also trace $R^{max}_{\mathrm{P/p}} = P_{\mathrm{sub}}/p_{\mathrm{max}}$ as a function of λ_{max} (right) to eliminate the effect of a possible spurious anti-correlation between p_{V} and λ_{max} (see text): the trend is still noticeable.

dependence of the polarization fractions with the structure of the magnetic field has been removed in the polarization ratio $R_{\mathrm{P/p}} = P_{\mathrm{sub}}/p_{\mathrm{V}}$.

Dependence of $R_{\mathrm{P/p}}$ with dust alignment We find a positive correlation between λ_{max} and $R_{\mathrm{P/p}}$ as shown in the left half of Fig. 4.12. Does this indicate that the division of P_{sub} by p_{V} has not removed all the dependencies of the polarization fractions with the dust alignment efficiency? Our data for p_{V} is not from direct observation, but rather calculated from p_{max} and λ_{max} following the Serkowski formula, as explained in Sect. 4.2.1: this introduces an artificial anti-correlation between p_{V} and λ_{max} which could explain the observed trend of increasing $R_{\mathrm{P/p}}$ with increasing λ_{max}. To make sure that the trend is indeed real, we define another quantity not subject to this bias: $R^{max}_{\mathrm{P/p}} = P_{\mathrm{sub}}/p_{\mathrm{max}}$. The right half of Fig. 4.12 shows that a positive correlation is also observed between λ_{max} and $R^{max}_{\mathrm{P/p}}$, reinforcing our hypothesis that dust alignment affects $R_{\mathrm{P/p}}$, though very mildly (Pearson correlation coefficient: 0.51). For further confirmation, we ran the tests described in Appendix D on the λ_{max} and $R^{max}_{\mathrm{P/p}}$ data, and both tests gave positive results with a confidence of 99% or higher.

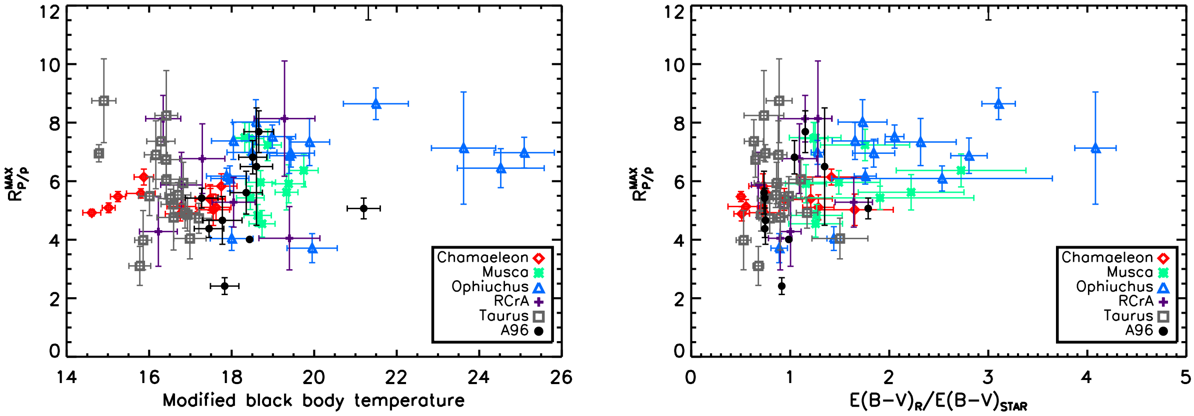

Fig. 4.13. The polarization ratio $R_{\mathrm{P/p}}$ shows no evident correlation with either dust temperature (left) or $G_0^{\mathcal{R}}$ (right), suggesting it might not be sensitive to ISRF intensity.

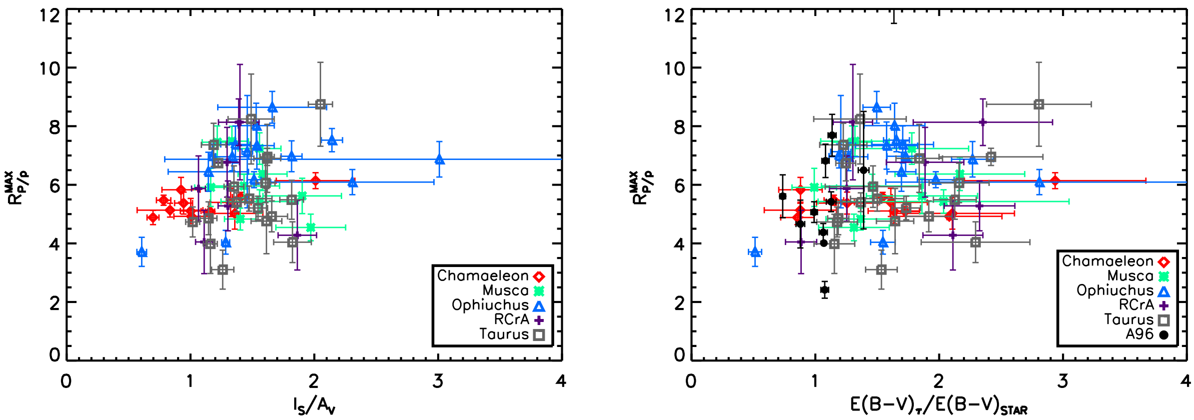

Fig. 4.14. Correlation between $R_{\mathrm{P/p}}^{max}$ and I/A_{V} (left) and $R_{\mathrm{P/p}}^{max}$ and the dust evolution parameter $E(B-V)_{\mathrm{S}}/E(B-V)$ (right).

Dependence of $R_{\mathrm{P/p}}$ with grain temperature In Fig 4.13, we check that this correlation is not driven by the decrease of the dust temperature with A_{V}, which affects P_{sub}, but not p_{V} neither p_{max}. The polarization ratio $R_{\mathrm{P/p}}^{max}$ does not correlate either (Fig. 4.13) with the dust temperature or with the dust radiation field intensity $G_0^{\mathcal{R}}$ inferred from the combination of the dust radiance with dust extinction[10].

This is not a surprise as the intensity at 353 GHz, *i.e.* in the Rayleigh-Jeans regime, is only weakly dependent on the grain temperature. We should also recall that the temperature of aligned grains, which is not measured by *Planck*, might differ from that of all grains taken together (Planck Collaboration Int. XXII 2015).

Dependence of $R_{\mathrm{P/p}}$ with dust evolution? Dust evolution in the optical or in the submillimeter range would affect both the total and polarization cross-sections. This could create a correlation between the ratios $R_{\mathrm{P/p}}^{max}$ and I/A_{V}, although the same effect could also be due the radiation field intensity affecting P_{sub} and I similarly (this effect is however weak in the Rayleigh-Jeans regime)

[10]More precisely, we use $5.4\,10^5 \cdot \mathcal{R}/\mathrm{E(B\text{-}V)}$ as our estimate of ISRF intensity

or to background effects. Fig. 4.14 (left), however, shows little or no correlation between $R_{\mathrm{P/p}}^{max}$ and I/A_{V} (Pearson correlation coefficient: 0.29). The search for correlation with the statistical tests of Appendix D also gives weak results: data fitting provides find a correlation when the binning is done on I/A_{V} but not on when it is done on $R_{\mathrm{P/p}}^{max}$, despite the two quantities having comparable uncertainties; at the same time, the k-test finds no correlation. The dust evolution scenario is further tested in Fig. 4.14 (right): we do not see any correlation between $R_{\mathrm{P/p}}$ and the parameter of dust evolution, $E(B-V)_{\mathrm{S}}/E(B-V)$. We should note that there is at least one evolution factor that will affect I/A_{V} without changing $R_{\mathrm{P/p}}$: the variations in the abundance of very small grains ($a \leq 5-10$ nm). Such grains only affect A_{V}. We will discuss in Section 4.6 how we could circumvent this problem.

Considering these results together with the weak evidence for correlation found for Fig. 4.9, we conclude that our analysis failed to reveal any convincing relation between the evolution of dust submillimeter opacity and the polarized observables we study. For the remainder of the analysis we decided to concentrate on the effect of dust alignment.

4.4 Methodology for the modeling

The correlation we found in Sect. 4.3.1 involves polarized quantities, one of which, λ_{max}, is often associated with alignment efficiency (*e.g.* Andersson et al. 2015). We decided to try and reproduce the correlation with a dust model with variable alignment. Our starting point should be a dust model compatible with the average observables for interstellar dust, including the new constraints on polarized emission derived from *Planck*.

4.4.1 Polarization model

The models used in Ch. 3 use spherical grains, and therefore predict no polarization. We need to use a different model with non-spherical grains. We adopt the model recently developed by Vincent Guillet (*work in progress*), which is built to correctly reproduce four observables as observed in the low-lattitude diffuse ISM: the extinction curve and the polarization in extinction up to 4 μm, the emission and polarization SED updated with *Planck* results. This implies that the average values of ratios such as I_λ/A_{V}, $R_{\mathrm{P/p}}$ and $R_{\mathrm{S/V}}$ are also correctly reproduced. The model is created starting from the classic C11 (Ch. 1, Sect. 1.3.3), with the following changes:

- To produce polarization, the big grains are now prolate spheroids with an axial ratio of 3. Oblate grains of equal axial ratio cannot reproduce the high P_{sub}/I observed by *Planck*, as will be described in this paper.
- The spectral index of silicates is the one from Draine & Lee (1984), rather than the updated version from Draine & Li (2001) which has a lower β at long wavelengths. This is because we need the polarizing grains to have a high β to reproduce a P_{sub}/I that decreases with wavelength, as revealed by *Planck*; meanwhile, the WMAP observation that Draine & Li (2001) was meant to explain is no longer critical[11].
- The model uses porous silicate grains, with an optical index calculated by adding 20% of vacuum, in volume, using the Bruggemann rule (Ch. 1, Sect. 1.2.2). Without this, $\tau_{\mathrm{FIR}}/\tau_{\mathrm{V}}$ is not high enough to reproduce the average value of $R_{\mathrm{P/p}}$ found in Planck Collaboration Int. XXI (2015). The increase in dust opacity obtained at 353 GHz by the shape and porosity effects is much higher than the decrease of the opacity due to the higher spectral index β.

[11] WMAP observed a much higher emission at 94 GHz than predicted by previous models, which prompted the reworking of the silicate optical index in Draine & Li (2001).

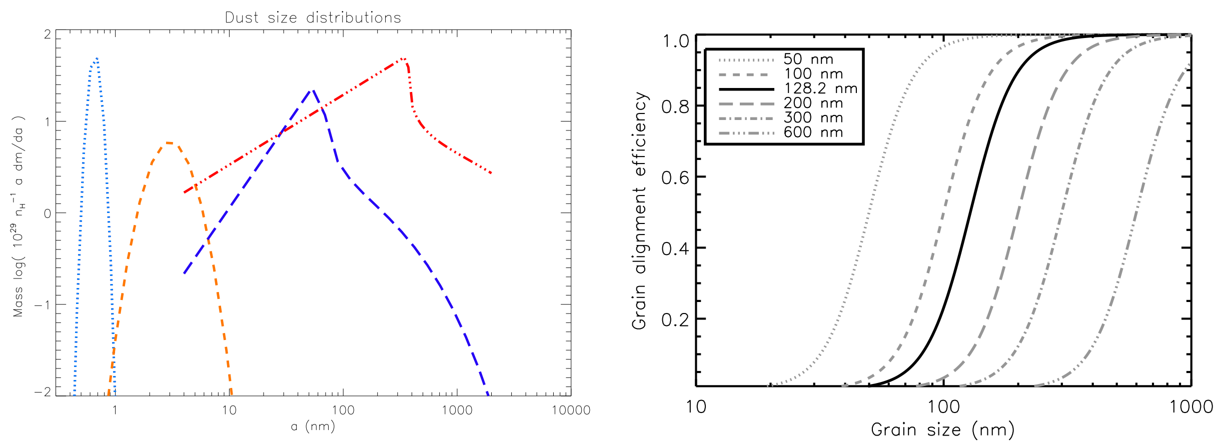

Fig. 4.15. *Left*: size distribution for the dust model used in this chapter. The dust populations present are: big silicate grains (red), big carbonaceous grains (dark blue), carbonaceous VSGs (orange) and PAHs (light blue). *Right*: shape of the alignment function (Eq. 4.2) for different values of $a_{\rm thresh}$, with the solid black line corresponding to the standard value (128.2 nm).

- Since we are interested in reproducing the far infrared and submillimeter emission, dominated by big grains, we simplify the model by neglecting the ionized PAHs and including only neutrals. Also, the VSGs are no longer a separate population, but they are incorporated in the amorphous carbon grain population, whose power-law size distribution is more weighed towards small grains.
- Two different versions of the model have been made to reproduce polarization, either with aligned silicates alone, or with aligned silicates and amorphous carbon grains (but no aligned PAHs). Both the grain size distribution and the alignment function of the grains depend on the version chosen for grain alignment.

The fact that some model parameters are degenerate means that even if it correctly reproduces the aforementioned observables the model is not necessarily the best description of interstellar dust: different combinations of grain size, shape and optical properties may reproduce the same observables as well. For this reason, the model is not intended as a faithful picture of interstellar dust; it is intended as starting point for studying the role of different dust characteristics on the variations of observables.

To keep the number of independent parameters to a minimum, we decided to study the case where only silicate grains are aligned. The corresponding size distribution and alignment function (*i.e.* the efficiency of alignment as a function of grain size) are shown in Fig. 4.15. The model requires a significant amount of very large ($\gtrsim 1\mu$m) silicate grains: this is necessary to reproduce the polarization in extinction at near-infrared wavelengths, where silicate grains have a rather low opacity.

4.4.2 Variable alignment

Once in possession of the model that explains the average ISM observations, we can apply variations to it and see what kind of change these cause in observables. Since it seems that alignment efficiency may play an important role, as remarked in Sect. 4.3.1, we observed the results of varying the alignment of grains as a function of size. In DustEM, the alignment function is parametrized as

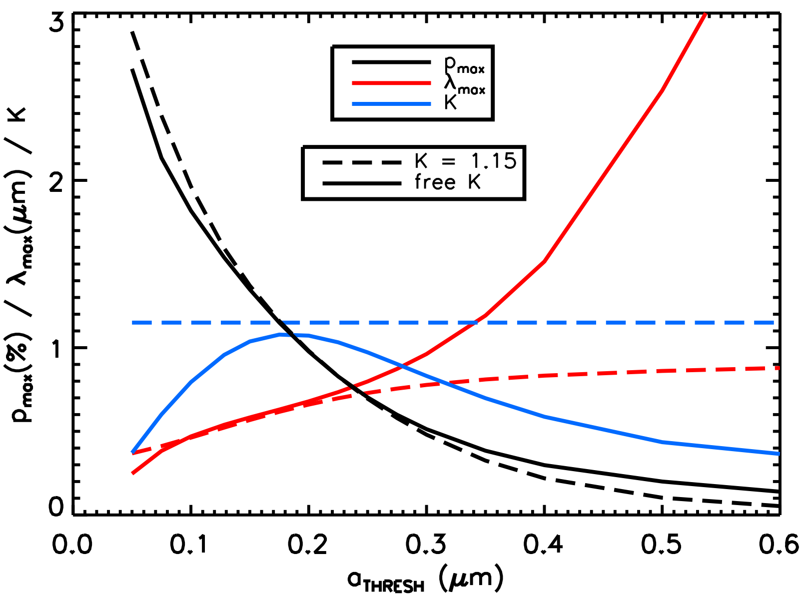

Fig. 4.16. Results of the Serkowski and Wilking fit to the model used in this chapter. The vertical scale in percentage points for $p_{\rm max}$, in μm for $\lambda_{\rm max}$. Both the fit with free K and the one with $K = 1.15$ are shown.

$$f(a) = f_{\rm max}\left(\frac{1}{2} + \frac{1}{2}\tanh\left(\frac{4\,\log(a/a_{\rm thresh})}{p_{\rm stiff}}\right)\right) \tag{4.2}$$

where $f_{\rm max}$ is the maximum alignment efficiency, $a_{\rm thresh}$ is the size threshold for grains alignment (more precisely, the size at which $f(a) = f_{\rm max}/2$), and the parameter $p_{\rm stiff}$ indicates the stiffness of the transition (a lower $p_{\rm stiff}$ value corresponds to a more sudden transition, approaching a step function for $p_{\rm stiff} \to 0$). Note that the alignment function increases monotonically with size, since it is known that small grains are generally unaligned (Ch. 1, Sect. 1.3.2).

We stress the fact that our modeling of grain alignment is phenomenological, but reproduces the dust observables in polarization (we did not test our model with observations of circular polarization, however). It is not designed to test any particular alignment process. Nevertheless, the alignment function choosen here is compatible with what one would expect from the radiative torque model.

To simulate the effects of different alignment efficiencies, we launched the model with different values of $a_{\rm thresh}$, keeping the same $p_{\rm stiff}$, for simplicity. The resulting alignment functions are plotted in Fig. 4.15. We did not change $f_{\rm max}$ because it has, in our model implemented within DUSTEM, the exact same effects on $p_{\rm V}$ and $P_{\rm sub}$, and it could have no effect on $R_{\rm P/p}$; $a_{\rm thresh}$, on the other hand, affects $p_{\rm V}$ and $P_{\rm sub}$ similarly but not identically, since polarization cross-section has different size-dependent behavior in the visible (where scattering is dominant) and in the submillimeter.

The model results are the extinction and emission curve, total and polarized. We obtain the model $A_{\rm V}$ as the value of the extinction curve at 550 nm and the model emission at 353 GHz as the value of the SED at the corresponding frequency, with a color correction applied at 353 GHz to account for the width of the *Planck* band. We obtain the parameters $\lambda_{\rm max}$ and $p_{\rm max}$ by fitting the polarization curve in extinction: for comparison we made both a Serkowski fit (with $K = 1.15$) and a Wilking fit with free K. It is remarkable, as seen in Fig. 4.16, that the two methods give similar $\lambda_{\rm max}$ and $p_{\rm max}$ even when K values are very different as long as one remains in the range $400\,{\rm nm} < \lambda_{\rm max} < 700\,{\rm nm}$. Outside this range, however, results quickly diverge, so fits with $K = 1.15$ clearly have very poor quality for extreme values of $\lambda_{\rm max}$.

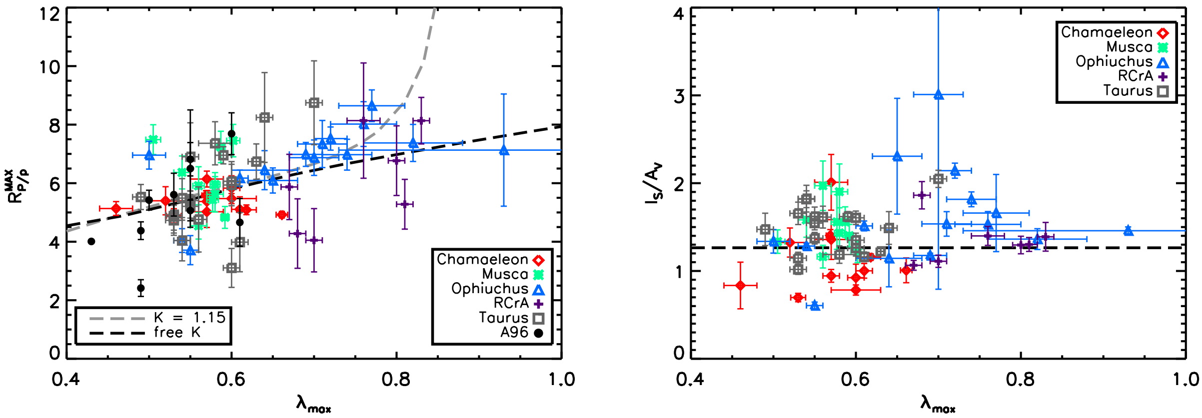

Fig. 4.17. Data and model comparison of the $R_{\mathrm{P/p}}^{max}$ vs. λ_{max} relation (left) and of the I/A_{V} vs. λ_{max} relation (right). Both the fixed K and the free K model are shown (see Sect. 4.4.2, Fig. 4.16), although only the model with free K is likely reliable at high λ_{max}.

4.5 Results

4.5.1 Polarization ratios

In this section we compare the observational data to the results of the model described in Sect. 4.4.1 and 4.4.2.

The relation between λ_{max} and $R_{\mathrm{P/p}}$ predicted by the model follows rather well the disposition of the data (Fig. 4.17, left), aside from a certain dispersion in the observed values (our model was not intended to explain this dispersion). The model also predicts that I/A_{V} be independent of grain alignment, and therefore of λ_{max}. The right side of Fig. 4.17 shows that this is indeed compatible with observations, although we cannot *a priori* exclude the presence of a shallow trend in the observations, hidden by the large data scatter. As a consequence, noise as well as other physical processes (namely dust evolution) must be responsible for the dispersion of the data around a model for the mean trend.

4.5.2 Polarization fraction

Both the observed $p_{\mathrm{V}}/A_{\mathrm{V}}$ and P_{sub}/I (Fig. 4.18) show a distribution enveloped by a decreasing function of λ_{max}, in qualitative accord with the expectations of Sect. 4.3.1. However, several lines of sight show values of $p_{\mathrm{V}}/A_{\mathrm{V}}$ and P_{sub}/I that are higher than the maximum predicted by the model: to have the predicted curve match the observations, the model needs to be approximately 50% more efficient in polarization, as shown by the dotted lines. This means that our reference model needs to be calibrated to achieve a higher polarization fraction in the optical and in the submillimeter, the 20% observed. A more recent model is able to achieve this, with only silicate aligned.

4.6 Conclusion & Perpectives

In this work, we have attempted to constrain the impact of the dust alignment efficiency and of dust evolution on dust polarization. We use the polarization ratio $R_{\mathrm{P/p}}$ to remove, at first order, the dependence of dust polarization with the magnetic field structure. This step is necessary even if the magnetic field, as probed by its orientation in the plane of the sky, appears to be rather uniform in the studied region.

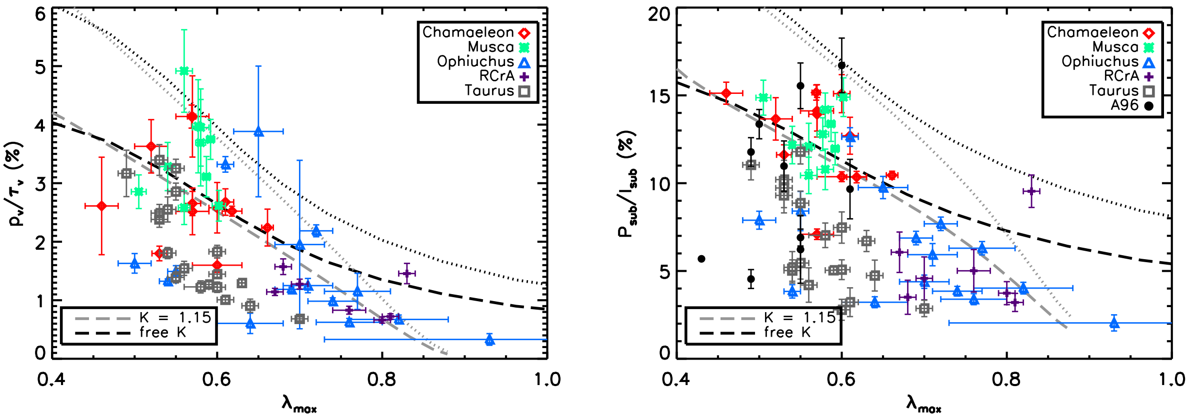

Fig. 4.18. Data and model comparison of the $\lambda_{\rm max}$ vs. $p_{\rm V}/\tau_{\rm V}$ and $\lambda_{\rm max}$ vs. $P_{\rm sub}/I$ relations. Both the fixed K and the free K model are shown as dashed lines (see Sect. 4.4.2, Fig. 4.16), although only the model with free K is likely to be more reliable at high $\lambda_{\rm max}$. Dotted lines show the model polarization multiplied by 1.5, showing how the model would work with an increase by 50% in polarization efficiency.

We observe a correlation between $\lambda_{\rm max}$ and $R_{\rm P/p}$ which is consistent with a model where variations in $\lambda_{\rm max}$ are driven by variations in the size threshold $a_{\rm thresh}$ for grain alignment. This correlation is independent of any assumption on the magnetic field configuration in each line of sight. The observed correlation is however weak, and should be statistically quantified. Our model results for the polarization fraction, $P_{\rm sub}/I$ and $p_{\rm V}/A_{\rm V}$, calibrated to be consistent with $\max(p_{\rm V}/A_{\rm V}) = 3\%$, correctly reproduce the trend observed but they underpredict the observed values. This study, which is a work in progress, will be revisited with a dust model calibrated to achieve 20% of polarization in emission.

Other interpretation are not excluded : both $\lambda_{\rm max}$ and $R_{\rm P/p}$ are affected by the optical properties of aligned grains. Still, no correlation has been found between $\lambda_{\rm max}$ and the tracer of average grain size $R_{\rm V}$ (Andersson & Potter 2007), nor between $\lambda_{\rm max}$ and the tracer of dust evolution found in this work (Sect. 4.3.1). This question of dust evolution needs more investigation.

4.6.1 Improved model

We have already mentioned that at first order $P_{\rm sub}$ and $p_{\rm V}$ have the same dependence on the alignment efficiency parameter $f_{\rm max}$. The fact that $R_{\rm P/p} = P_{\rm sub}/p_{\rm V}$ is not independent of alignment makes it clear that higher-order effects are not negligible in the interpretation of these observations. A second order effect that we neglected in our work is the dependence of both the extinction and thermal emission cross-sections on grain orientation: if the grains are non-spherical, the effective surface they offer to our observations depends on their alignment and on the orientation of the magnetic field lines. Such corrections – which DustEM is already equipped to make – may have some effect.

4.6.2 Improved data analysis

The use of the total extinction in the V band probably brings a lot of scatter to our analysis. It is indeed the only parameter that is affected by small, stochastically heated, grains ($a \leq 5$ nm): $I_{\rm sub}$ is dominated by large cold grains, and $P_{\rm sub}$, and $p_{\rm V}$ are not influenced by the small grains abundances because those grains are not aligned. To circumvent this problem, we will use extinction maps by Schneider et al. (2011), derived from 2MASS near-infrared color excess measurements. A first glance already shows a much better correlation between I and $A_{\mathrm{V}}^{\mathrm{2MASS}}$, and therefore much less scatter in I/A_{V} than in the present study.

4.6.3 Improved background detection

We mentioned in Sect. 4.3.1 that background contamination is still possible, and that it might make some correlations difficult to detect. We intend to make a further check of the effects of contamination using an alternative measure of dust extinction: again the extinction maps by Schneider et al. (2011), which ought to be accurate up to distances of 3 Kpc. If the use of these A_{V} maps improved the correlation between observables in extinction and in emission, it might mean that the stars from Andersson & Potter (2007) and Anderson et al. (1996) still have a non-negligible background.

Conclusions

Summary

In this thesis we show how the statistical comparison of emission to extinction in the optical can advance our understanding of interstellar dust in the diffuse ISM. The advantage of an emission-to-extinction dust comparison is double: 1) Standard extinction curves and SED tend to probe different media (since extinction curves are usually measured in relatively high-extinction zones), and therefore different dust, whereas a dedicated comparison of extinction with emission on carefully selected lines of sight will provide a consistent set of measures; 2) The correlation of emission with extinction, as opposed to gas column density N_{H}, also allows to derive a quantity that depends primarily on the dust optical properties, and can be used to constrain dust models. Submillimeter and optical/IR observations are adapted to that work because they both probe the larger grains ($a \sim 0.1\,\mu$m) of the size distribution.

Both unpolarized and polarized observations benefit from this approach. By correlating dust emission with A_{V} on the same lines of sight, we remove any dependence on the dust-to-gas ratio that arises from the correlation of dust emission with gas tracers such as H I or CO emission. By correlating dust polarized emission with the starlight polarization degree in the optical, we remove the first order dependence of the polarization fraction with the magnetic field structure and with the dust alignment efficiency, bringing an observable that is purely dust-related (optical properties, size-dependence of dust alignment).

Using unpolarized observations of the dust emission SED per unit dust extinction, building on the results of Planck Collaboration XI (2014) and Planck Collaboration Int. XXIX (2014), we estimated the contributions of the radiation field intensity and of the dust optical properties to the variations of dust emission SEDs in the diffuse ISM. In the process, we showed the limits of several modern dust models. We fitted the dust SEDs with different dust models from the literature, comparing the V band extinction from the model, $A_{\mathrm{V}}^{\mathrm{fit}}$, to the observed A_{V}. We found that: 1) the Jones et al. (2013) dust model is closest to the data, with $A_{\mathrm{V}}^{\mathrm{fit}} \sim A_{\mathrm{V}}$, while the $A_{\mathrm{V}}^{\mathrm{fit}}$ derived with the widely-used Draine & Li (2007) dust model departs from the data by a factor ~ 2; 2) all models present a bias on $A_{\mathrm{V}}^{\mathrm{fit}}/A_{\mathrm{V}}$ which is dependent on the dust temperature: models systematically show higher $A_{\mathrm{V}}^{\mathrm{fit}}/A_{\mathrm{V}}$ at low temperatures. We checked that variations in the size distribution of grains could not reproduce this trend. This demonstrates that the observed variations in the extinction-normalized dust SED cannot be explained by a model with fixed optical properties, but are due to variations of the dust optical properties in the diffuse ISM. We developed a new estimator for the radiation field intensity G_0, that combines extinction and emission measures. To reproduce the observed variations of the SED through the diffuse ISM as sampled by Planck Collaboration Int. XXIX (2014), we need to vary G_0 by a factor ~ 1.6 between the coldest and the warmest SED, while the ratio of submillimeter to V-band dust opacity must correspondingly decrease by a factor ~ 1.4: we conclude that the ISRF and the dust optical properties give a similar contribution to the variations of dust emission SEDs in the diffuse ISM. This contributes to the current changes in the way of picturing the diffuse ISM, from a relatively static and uniform environment to a dynamic, structured one.

On the subject of dust polarization, the *Planck* observations and the emission-to-extinction comparison allowed us to tackle the confusion between the three main factors at play in polarization data: the orientation of the magnetic field, the grain alignment and the dust properties. We concentrated especially on two polarization observables: the wavelength of maximum polarization in extinction, $\lambda_{\rm max}$, and the ratio between the polarization intensity at 353 GHz, $P_{\rm sub}$, and the starlight polarization degree at its peak (p at $\lambda = \lambda_{\rm max}$). Since $P_{\rm sub}$ and $p_{\rm max}$ have approximately the same dependency on magnetic field orientation and structure, the ratio $R^{max}_{\rm P/p} = P_{\rm sub}/p_{\rm max}$ normalizes out the contribution of the magnetic field. We correlated $R^{max}_{\rm P/p}$ with $\lambda_{\rm max}$ for a selection of lines of sight to stars through translucent and molecular clouds. We observe a correlation between $\lambda_{\rm max}$ and $R^{max}_{\rm P/p}$ that is consistent with a model where the variations in the starlight polarization degree and in the submillimeter polarization intensity are driven by variations in the dust alignment efficiency alone, without any need to change the dust properties; at the same time, we could not identify any correlation between polarization and dust evolution.

Our results, with their implications for the dependence of P/I on dust alignment, are complementary to those of the Planck Collaboration Int. XX (2015) team on the dependence of P/I with the magnetic field structure. Our work and its continuation insert themselves in the quest to understand the relative importance of the three players in the field of polarization: magnetic field, alignment and dust grain properties.

Next steps

Although the work on dust evolution in Ch. 2 and 3 was based on the comparison of emission and extinction, it should be remarked that the use of dust extinction was limited to a single band. Using the full extinction curve will allow us to include all grain populations. The ultraviolet section of the extinction curve, dominated by very small grains, would allow to normalize the mid-infrared emission and extend the analysis which, in the present thesis, is limited to grains in thermal equilibrium. Since the variations of the mid-infrared SED are sensitive to the presence of high-G_0 regions (Planck Collaboration Int. XXIX 2014), an analysis of small grain evolution could also improve our understanding of the distribution of the ISRF in diffuse Galactic lines of sight. Another limitation of this work is that, while the degeneration between the G_0 estimator and the dust optical properties has been partly corrected, the ISRF intensity is still degenerate with albedo. In particular, it should be noted that while the Jones et al. (2013) and Compiègne et al. (2011) dust model were better than the Draine & Li (2007) dust model at reproducing the SED per unit extinction, they do not reproduce the albedo in the optical so well like Draine & Li (2007), as estimated from the diffuse galactic light (Draine 2003). This unconsistency should be investigated.

The work on polarization presented in Ch. 4 is, as we mentioned, a work in progress. We showed that we are able to separate the effects of magnetic field tangling from alignment and dust properties, which will improve constraints on grain alignment models; however, a thorough and physically-justified analysis of dust alignment and polarization will require better treatment of the analysis as well as more adapted data where possible.

On the data side, these studies will benefit from extended and improved extinction measurements. For instance, the majority of high-$\lambda_{\rm max}$ stars in our sample come from a single cloud: Ophiuchus. To ensure that the relations found pertain to dust in general and not simply to this one cloud, it would be useful to add more examples of extreme $\lambda_{\rm max}$ values to our pool. The next step in our analysis will be to add the stars of Wilking et al. (1982) to our analysis. Another issue with data lies in the use of extinction measurements in the optical: $A_{\rm V}$ and E(B-V). Quantities that compare optical extinction to observables that depend on big grains alone show generally a very large scatter (see *e.g.* $I/A_{\rm V}$ in Fig. 4.18, right); contributions to this scatter might come from variations not only in the properties of big grains, but also in the properties and relative contribution of small grains. To reduce the uncertainty from this source one can use the extinction maps derived from the 2MASS survey: while the V band extinction is likely to include some contribution from small grains, NIR extinction is certain to come from big grains alone. We have already seen that, when tentatively remaking some of the plots using the 2MASS extinction maps rather than the optical A_{V}, the scatter decreases considerably. This however needs more work, especially regarding the determination of offsets in 2MASS maps.

The modelling side of our studies also has room for improvement. The model described in Sect. 4.4, for instance, uses the simplified "picket-fence" alignment where only three (orthogonal) orientations for the grain rotation axis are considered. The picket-fence model presents certain limitations; for instance, it implies that the effects of grain alignment are the same in extinction (scattering-dominated) and in emission (in the Rayleigh regime, where they are expressed by the Rayleigh reduction factor). This is only true as a first approximation (as discussed *e.g.* by Martin 2007); while Planck Collaboration Int. XXI (2015) shows that polarization in extinction and in emission are very well correlated, and therefore applying the Rayleigh reduction factor in extinction is a reasonable approximation, a more realistic model of grain alignment would be a useful check. I had already taken steps in this direction during the thesis: using the DUSTPROP tool (Sect. 1.3.3) I had calculated the extinction cross-section for both oblate and prolate grains as a function of their orientation. Subsequently, I averaged these cross-sections over the orientations that a grain assumes in its rotation and precession motions (Sect. 1.3.2). Preliminary results seemed to confirm that, for selected values of the precession angle β and the angle γ between the magnetic field and the plane of the sky, the Rayleigh reduction factor can be applied in extinction without introducing a significant error. The next step in this analysis will be to compare the results for a full distribution of orientations, preferably with a physical model such as Davis-Greenstein.

Another limitation of our current model is that it does not account for variations of the dust or environmental conditions on the line of sight; in particular, we have not studied the effects of the radiative transfer on our observables. Due to temperature effects, the polarized emission is more weighted towards the outer envelope of the clouds than polarization in extinction, which can introduce a bias on $R_{\mathrm{P/p}}$ and $R_{\mathrm{P/p}}^{max}$ just like it does in total emission and total extinction. It would be advisable to assess the effect of radiative transfer on the quantities used in Ch. 4.

Perespectives

The relevance of this thesis spans very diverse topics, from the extrapolation of the polarized dust SED to the microwave range in order to clean the CMB of foregrounds to the improvement of our understanding of dust evolution from the most diffuse ISM down to accretion disks where planetesimals form.

Polarization data in emission will benefit from the PILOT experiment: this stratospheric balloon is beginning now to observe the sky in channels that include polarization at 550 and 240 μm, where dust polarized emission is more intense and not far from its peak. In the future we will be able to test dust polarization models in the submillimeter with a whole polarized SED, including the temperature of aligned grains, akin to what we did in this thesis with unpolarized emission. PILOT will also provide the first large unpolarized sky survey at 240 μm, helping bridge the gap between the IRAS 100 μm band and the *Planck* 350 μm band; gap which happens to contain the dust SED peak ($\sim 150\,\mu$m).

The physics of accretion disks and the formation of solar systems in particular will be a fertile topic in the next few years, thanks to data of unprecedented quality that will come from the current and next generation of instruments – instruments such as the ALMA interferometer, which will observe big grain emission at the scales of accretion disks, or the James Webb Space Telescope, which will observe dust extinction in the infrared allowing to probe inside dense clouds. The science of ALMA and JWST will constitute a huge step forward for the study of dust properties, making them excellent projects to work in to study dust evolution toward the formation of planetesimals.

Part IV

Appendices

Appendix A

The $\mathrm{optEC_{(s)}}$ and $\mathrm{optEC_{(s)}(a)}$ models

Contents

The present section will describe the so-called $\mathrm{optEC_{(s)}}$ model for hydrogenated amorphous carbon, presented in Jones (2012a,b,c) using Robertson (1986) as a starting point. This is the model used for the refractive index of amorphous carbon in, *e.g.*, Jones et al. (2013, 2014); Köhler et al. (2014); Ysard et al. (2015).

A.1 Composition-dependent optical properties: the $\mathrm{optEC_{(s)}}$ model

The denomination *hydrogenated amorphous carbons* covers a large variety of materials that show very different optical properties, and which can essentially be classified based on the abundance of hydrogen in them. The fraction X_H of hydrogen atoms in the material can vary roughly between 0 and 0.6. These materials are referred to as a-C:H in the case of high hydrogen content and a-C in the case of low hydrogen content; a-C(:H) being the generic denomination for all of them.

The modeling of interstellar dust requires the knowledge of the optical properties of a-C(:H) over a wavelength range spanning from extreme ultraviolet (EUV) to cm wavelengths, and covering the whole range of possible X_H. The knowledge of the whole range of hydrogen content is essential, because these materials is can evolve by losing hydrogen through UV irradiation – photo-darkening – or thermal processes – annealing (*e.g.* Mennella et al. 2001; Jones 2012b and refs. therein). We expect the hydrogen content of a-C(:H) to depend locally on the grains' history, namely, the environment they've been in and the amount of time they've been subjected to it.

Since we do not yet have experimental data covering the full range of wavelengths and materials, modelling is needed to fill the information gaps. The $\mathrm{optEC_{(s)}}$ model provides an extension of experimental data on the refractive index $m = n+ik$ of a-C(:H) materials as a function of wavelength and for a grid of X_H values.

E_g [eV]	X_H	Color
-0.1	0.00	black
0.0	0.00	dark gray
0.1	0.02	mid gray
0.25	0.05	light gray
0.5	0.11	pink
0.75	0.17	red
1.0	0.23	brown
1.25	0.29	orange
1.5	0.35	yellow
1.75	0.41	green
2.0	0.47	blue
2.25	0.52	cobalt
2.5	0.58	violet
2.67	0.62	purple

Table A.1. The color code for X_H and E_g in the plots, from Jones 2012a, b, c, d, e.

A.1.1 The Tauc band gap E_g

Hydrogenated amorphous carbons are usually semiconductors and, as such, are characterized by a band gap. We can define for these materials a parameter called "Tauc band gap" E_g which is closely related to the material's hydrogenation.

Figure A.1 shows some experimental data on a-C(:H), presented as a so-called Tauc plot: $\sqrt{\alpha E}$ as a function of E, where α is the absorption coefficient ($\alpha = 4\pi k/\lambda$, where k is the imaginary part of the refractive index) and E is the energy of the photon. For all materials there is a portion of the plot that is linear, and can be extrapolated to find an intercept with the X axis. The value of this intercept is the so-called *Tauc band gap* E_g and it is the single most important parameter in the classification of a-C(:H) – in fact, the only parameter used in the optEC$_{(s)}$. E_g varies between ~ -0.1 and ~ 2.7 eV. For $E_g > 0$ there is a linear relation between E_g and X_H:

$$E_g = 4.3 \cdot X_H \tag{A.1}$$

so that they are essentially equivalent in the a-C(:H) classification.

A.1.2 Calculation of the IR absorption bands

In the optEC$_{(s)}$ model, a-C(:H) materials are essentially composed of clusters of aromatic rings connected by aliphatic bridges. UV photons can break C–H bonds, leaving hydrogen free to form H_2 and abandon the material and causing the C atoms with dangling bonds to form C=C pairs or C_6 aromatic rings. Aromatic domains are thus larger in a-C than in a-C:H which is why low-hydrogenation amorphous carbon are called "aromatic" and the high-hydrogenation carbon are calle "aliphatic".

Analytical expressions for the abundance of C_nH_m groups in a-C(:H) as a function of X_H can be found, using the *extended Random Covalent Network* (eRCN) or the *Defective Graphite* (DG) models depending on the X_H range where the material belongs (Jones 2012a). Using experimental values for he absorption cross-section for each of these groups, the X_H-dependent absorption bands for a-C(:H) materials can be calculated (Fig. A.2).

Another important quantity for which an analytical expression as a function of X_H can be obtained is a_R, the radius of the largest aromatic domains in the material, which is what effectively

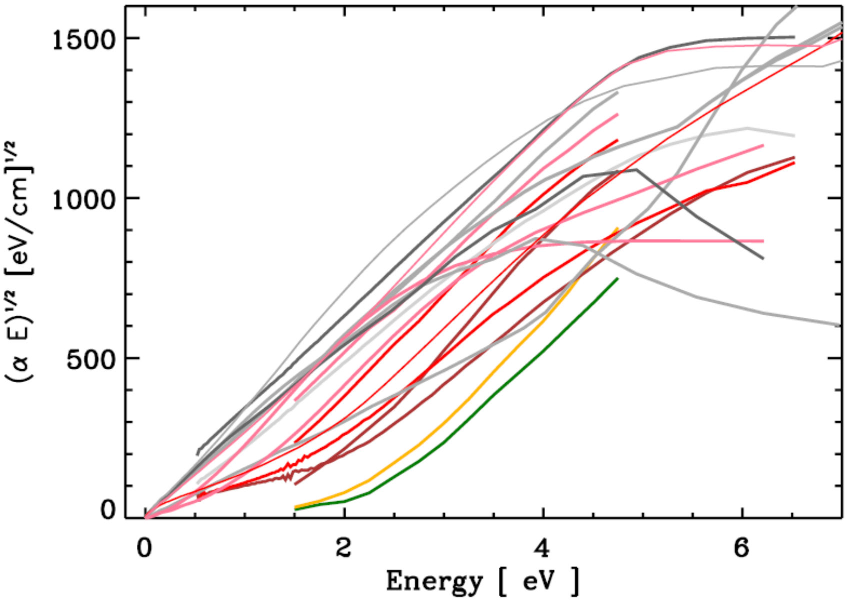

Fig. A.1. Tauc plot for several a-C(:H) materials. The materials are distinguished by their hydrogen content and are color-coded acording to table A.1. From Jones (2012b).

determines $E_{\rm g}$. Calling $N_{\rm R}$ the number of aromatic rings forming one domain or cluster, the relation between $a_{\rm R}$ and $E_{\rm g}$ is given by

$$N_{\rm R} = 5.8 \left[\frac{5.8}{E_{\rm g}(\rm eV)}\right] \qquad \text{(Robertson\&O'Reilly 1987)}$$
$$a_{\rm R} = 0.09\,[2\,N_{\rm R} + 3.5\,\sqrt{N_{\rm R}} + 0.5]^{1/2} \qquad \text{(Jones 2012b)} \tag{A.2}$$

A.1.3 Calculation of the long-wavelength continuum

In addition to the bands, an approximated underlying continuum for a-C(:H) materials can be obtained semi-empirically. The a-C(:H) materials show an approximately linear behavior at long wavelengths, and more precisely where photons have energies (measure in eV) lower than $4.5 - E_{\rm g}/1.2$. In this regime, an empirical expression can be found for k (Jones 2012b):

$$k(E, E_g) \propto E^{\eta} \qquad \text{where} \quad \eta = 2(E_g[eV] - 0.07) \tag{A.3}$$

This linear relation is entirely empirical and limited by the available data. Further experimental data will likely reveal a more complex picture.

A.1.4 Optical properties as a function of $E_{\rm g}$

Fig. A.3 shows the $E_{\rm g}$-dependent absorption and extinction coefficients obtained with optEC$_{(s)}$ for a-C(:H) materials. A few notable trends are:

- The absorption continuum increases with wavelength for small λ, peaks somewhere between the NUV and the visible depending on $E_{\rm g}$, then decreases. The peak's position shifts towards

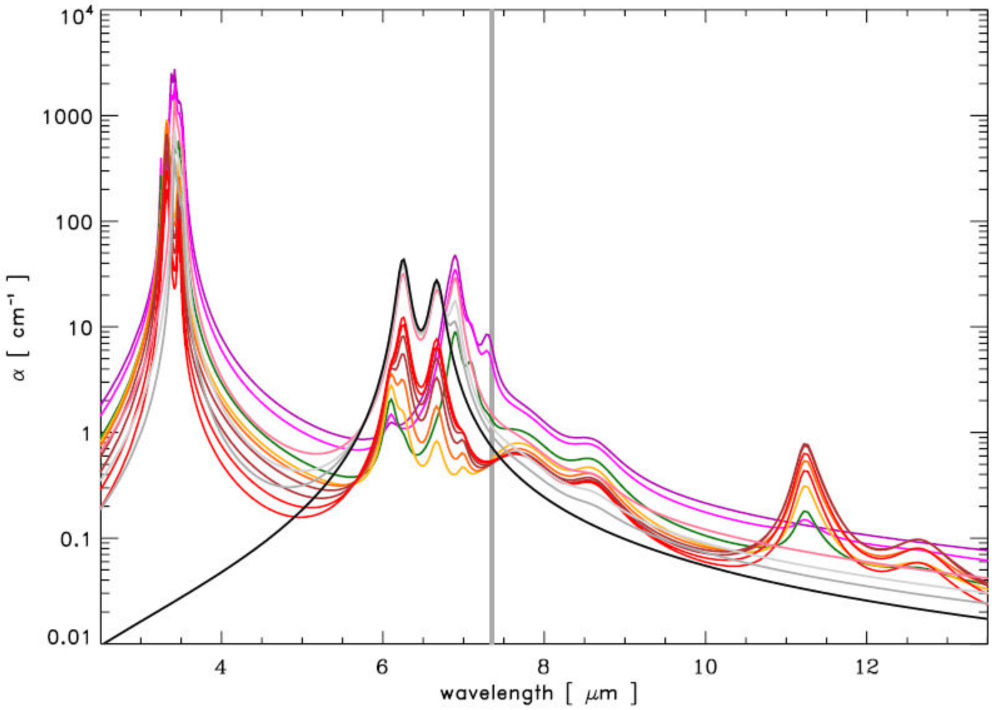

Fig. A.2. The IR absorption bands predicted by the optEC$_{(s)}$ model as a function of E_g. The color code for E_g is in tab. A.1. The vertical grey line marks $\lambda = 7.3\mu m$: at longer wavelengths laboratory data are scarce and the modeled bands are uncertain. From Jones (2012a)

longer wavelengths as E_g decreases: it is around $0.3\,\mu$m for $E_g \sim 2.5$ eV and around $0.7\,\mu$m for $E_g \lesssim 0$ eV.

- Absorption increases with E_g in the UV (essentially for $\lambda < 0.4\,\mu m$), while the opposite is true in the optical ($\lambda > 0.4\,\mu m$).
- In the far infrared and submillimeter, where $Q_{ext} = Q_{abs} \propto \lambda^{-\beta}$, the spectral index β has a strong dependency on E_g: its value is ~ 2 for the most aliphatic material, it increases to ~ 2.7 for $E_g = 1$ eV, then drops to ~ 1.3 for $E_g = 0.1$ eV and rises again to ~ 1.7 for the lowest E_g.

A.2 Size-dependent optical properties: the optEC$_{(s)}$(a) model

The optical properties described by the optEC$_{(s)}$ model are valid in an infinitely extended network – which is the reason of their name, *bulk material* optical properties – and they are a good approximation for large enough grains ($a \gtrsim 30$ nm). However, for interstellar dust grains of sub-nm size – not much larger than the average interatomic bond – the approximation is no longer valid. For these grains there are two correction to make to the model:

- Surface effects become important. Specifically, if we truncate the network at the grain's surface, there will be carbon atoms with dangling bonds that need passivating. The model passivates these bonds by adding hydrogen atoms, which increases the number of C–H bonds. For grains small enough that a relevant fraction of atoms is on the surface, this addition is enough to alter the optical properties, even without changing the material's E_g.

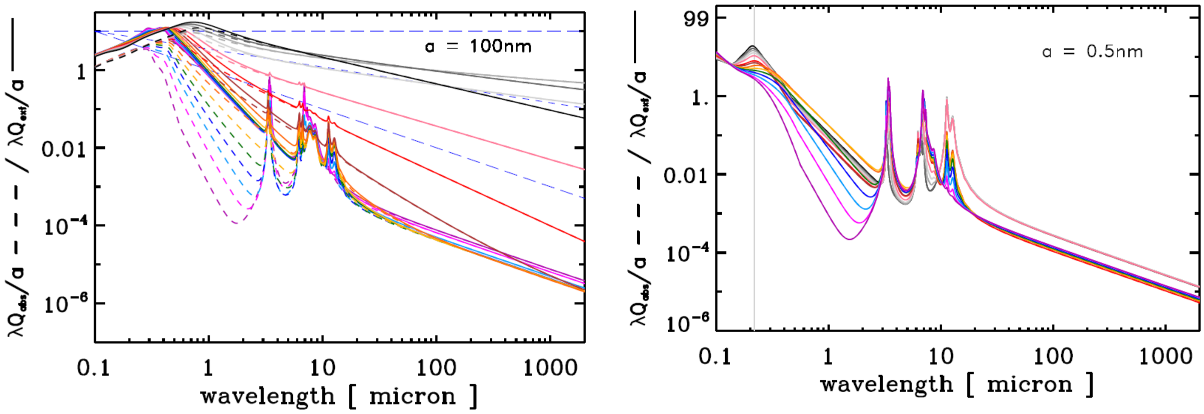

Fig. A.3. The absorption ($Q_{\rm abs}$, short slashed lines) and extinction ($Q_{\rm ext}$, solid lines) coefficients of optEC$_{(s)}$ data, plotted for clarity as $\lambda Q/a$. The right side shows the case $a = 100$ nm, where optical properties are identical to those of the bulk material; the left side shows the case $a = 0.5$ nm, where size effects are evident (Sect. A.2). The long slashed blue lines show $\lambda^{-\beta}$ with $\beta = 1$, 1.5, and 2 (top to bottom), for comparison. From Jones (2012c).

- The domain size $a_{\rm R}$ has now an upper limit given by the grain's size and it no longer depends only on $X_{\rm H}$. Since $a_{\rm R}$ is what determines the effective band gap (larger $a_{\rm R}$ give lower $E_{\rm g}$), small grains can have more "aliphatic" characteristics than larger grains with the same $X_{\rm H}$. How strong is this effect depends on both grain size and $X_{\rm H}$: the more aliphatic the material, the smaller grains must be before the effect becomes noticeable, since $a_{\rm R}$ is smaller. As can be seen in fig. A.4, the result is that the smallest grains always have e high effective $E_{\rm g}$.

The $X_{\rm H}$-$E_{\rm g}$ relation given by eq. A.1 is no longer valid: now the band gap depends also on the grain radius, and $E_{\rm g} = E_{\rm g}(X_H, a)$. This can also be written as $E_{\rm g} = E_{\rm g}(E_{\rm g(bulk)}, a)$, where $E_{\rm g(bulk)}$, the "bulk material bandgap" can be calculated from $X_{\rm H}$ using eq. A.1.

A.3 Astrophysical processing: evolutionary timescales

Carbon grains in the ISM evolve due to loss and acquisition of hydrogen. Understanding the nature of interstellar grain carbon, aromatic or aliphatic, requires to compare the time of permanence in the ISM to the grain processing time-scale. Let us take the example of a carbonaceous grain in the diffuse ISM, where photo-darkening is the prevalent process (Jones et al. 2014). We will show the estimation for the optEC$_{(s)}$ photo-darkening rate used in (Jones 2012b); a more sophisitcated version can be found in Jones et al. (2014). The processing rate can be written as:

$$\Lambda_{\rm UV} = F_{\rm EUV} \cdot \sigma_{\rm CH} \cdot Q_{\rm abs}(a, E) \cdot \epsilon \tag{A.4}$$

where $F_{\rm EUV}$ is the flux of photons with $E > 10$ eV (the energy needed to break a C–H bond), $\sigma_{\rm CH}$ the C–H bond photodissociation cross-section, $Q_{\rm abs}(a, E)$ the size- and composition-dependent grain absorption coefficients, and ϵ the band photo-darkening efficiency (not all absorbed photons break bonds, some cause heating or fluorescence). Photo-dissociation studies on CH_4 put $\sigma_{\rm CH}$ at 10^{-19}cm^2, centered at 1070 Å and with a 330 Å bandwidth (10-13.6 eV, centered at 11.6). For a typical ISRF we have $F_{\rm EUV} = 10^5$ photons cm$^{-2}s^{-1}$Å^{-1}, which integrated over the $\sigma_{\rm CH}$ bandwidth gives $F_{\rm EUV} \simeq 3 \cdot 10^7$ photons cm$^{-2}s^{-1}$.

Substituting these results in Eq. A.4 we can find the relevant time-scale: $\tau_{\rm UV} = \Lambda_{\rm UV}^{-1} \simeq \frac{10^4}{Q_{\rm abs}(a,E)\epsilon}$.

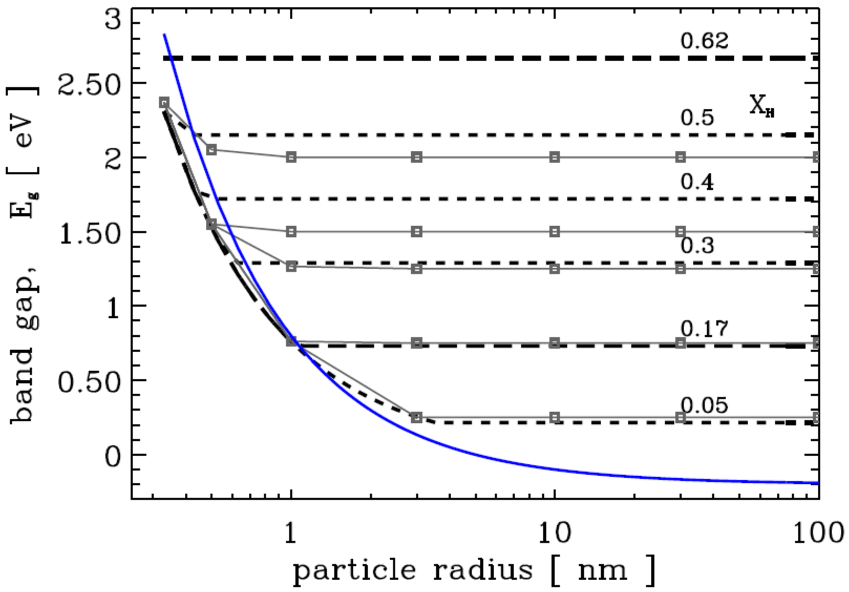

Fig. A.4. The black dashed lines are the bandgaps of optEC$_{(s)}$(a) particles as a function of of X_{H} (numbers) and size (X axis). Below a few nm in size, bandgaps increase even at constant X_{H}. The limiting size is larger for lower hydrogenation. The blue curve is an approximate empirical fit for the value of E_{g} over which domain size effects are negligible, $E_{\mathrm{g}}(eV) = a(nm)^{-1} - 0.2$.

Assuming $Q_{\mathrm{abs}}(a, E) \simeq 1$ in the EUV (which corresponds to the linear growth in the short wavelength region of Fig. A.3) and $\epsilon = 0.1$, we obtain $\tau \simeq 10^5 yr$. For the smallest grains, in the Rayleigh regime, Q_{abs} is lower, and the characteristic time can become as long as $10^6 yr$.

As mentioned in Ch. 1, Sect. 1.1.4, the typical time of permanence in the diffuse ISM for a dust grain is of the order of $10^6 yr$, so interstellar dust grains have the time to be fully processed to a depth equal to the optical depth for UV photons in a-C(:H) materials, $\sim$ 20 nm. Since a-C(:H) materials form at relatively high hydrogenation (Jones et al. 1990), we can expect that small grains ($a \lesssim 20$ nm) be completely aromatized, but larger grains assume a core-mantle structure, with an aliphatic interior and an aromatic exterior, as seen in the J13 model.

Appendix B

Poster for *The Life Cycle of Dust in the Universe* conference, Taiwan, 2013

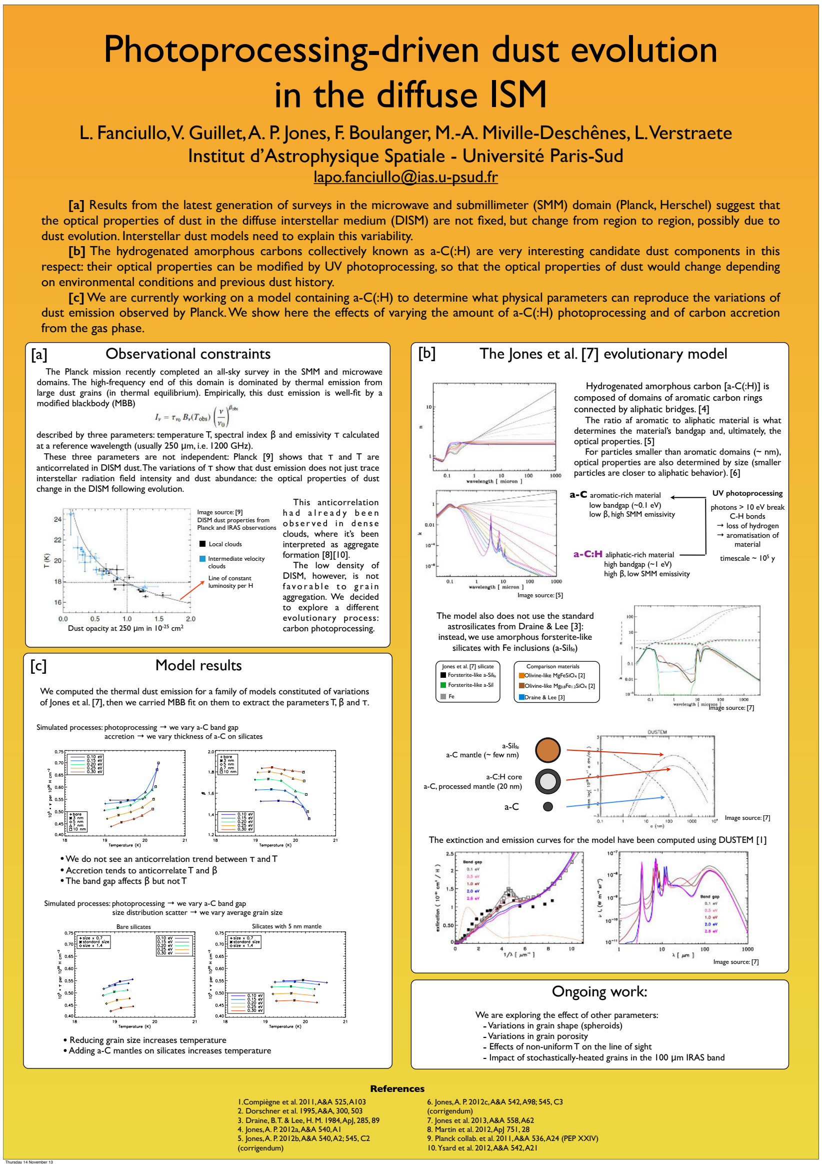

Appendix C

Emission-to-extinction conversion for the *Planck* all-sky survey

Planck Collaboration XI (2014) provides two empirical relations to relate emission quantities to E(B-V) which make full use of the new *Planck* data. To find these two empirical relations it was necessary to know E(B-V) for a large number of lines of sight, and compare it to *Planck* submillimeter observables on the same lines of sight. This was possible thanks to the measurement of quasars from the seventh Sloan Digital Sky Survey (SDSS) data release (Schneider et al. 2010). The survey provides the colors $m_X - m_Y$ for a sample of 53 399 QSOs, where X and Y indicate two bands in the u, g, r, i, z system and m is the measured magnitude in those bands. To compute the reddening in each band one also needs to know the QSO spectrum and its intrinsic colours $m_{X_0} - m_{Y_0}$. The intrinsic colours can be estimated by correlating the observed extinction with a column density tracer. Using $N_{\mathrm{H_I}}$ to trace column density, Planck Collaboration XI (2014) found the colors as:

$$m_X - m_Y = \eta \times N_{\mathrm{H_I}} + m_{X_0} - m_{Y_0} \tag{C.1}$$

This estimation presents two difficulties: first, the intrinsic colour depends on the redshift z, so the QSOs had to be binned by redshift and the fit executed independently on each bin. Secondly, at the low values of extinction measured here (E(B-V) ~ 0.1) the noise is very important: it was overcome thanks to the large number of QSO used.

A consistency check was made: since QSOs have rather regular spectra, composed of emission lines superposed on a power-law continuum, template spectra are available; Planck Collaboration XI (2014) used the template spectra of Vanden Berk et al. (2001) to compute the expected $m_{X_0} - m_{Y_0}$ as a function of z and compare them to the fit results.

Once in possession of the QSO colour excesses $(m_X - m_Y) - (m_{X_0} - m_{Y_0})$, Planck Collaboration XI (2014) interpolated them using the Global Mean Curve from Fitzpatrick (1999) with an R_{V} of 3.1, obtaining the reddening E(B-V). Each QSO resides in a *Planck* pixel, for which a value of τ_0 and a $\mathcal{R}$ exist; so it is possible to fit E(B-V) as a function of them.

Appendix D

Statistical tests for correlation

Contents

One of the main purposes of the work exposed in Ch. 4 was to find interesting correlations between observables, to be used to test dust and alignment models. Sometimes the correlations between quantities, or lack thereof, are evident to the eye; however, in some cases a more stringent test is needed. In particular, we want to examine the relation between dust evolution and $\lambda_{\rm max}$ (see Fig. 4.9), between $\lambda_{\rm max}$ and $R^{max}_{\rm P/p}$ (Fig. 4.12, right) and between $R^{max}_{\rm P/p}$ and $I/A_{\rm V}$.

We use three different methods: the fit of a linear model to the data, with binning to get rid of the data scatter, the χ^2 two-sample test or *k-test*, and the Spearman rank for correlation (Wall & Jenkins 2012). The purpose of these tests is not to show the correctness of some physical model, but to understand in what cases we are justified in considering two quantities correlated, to decide if the correlation is worth studying in more detail.

D.1 Data fit (with binning)

We want to check whether or not two quantities, X and Y, are correlated. To do this, first we need a mathematical description of the two alternative hypotheses to be compared:

H_0: The two quantities are independent. We assume that this is equivalent to claiming that, in a Y vs. X plot, the values of Y are scattered around a constant value.

H_1: The two quantities are related. We assume that this is equivalent to Y being a linear function of X plus a scatter. We limit ourselves to linear models because all of the data set that we consider present a large scatter, which will mask any dependence more detailed than that.

The idea is to test these two hypotheses with a χ^2 test. This kind of test, however, requires that one knows the distribution of the residuals on the data: this, in the general case, it will depend on the parameters that influence the quantities X and Y[1], which we do not know. We can circumvent this difficulty by binning the data on either X or Y and creating a new data set: in the new dataset, the value of each point is the average on a bin and the uncertainty of each point is the standard deviation of the data in each bin divided by $\sqrt{n_i}$ (where n_i is the number of measurements in each bin i).

[1]The parameters in question obviously depend on what quantities X and Y are. Since the quantities examined in Ch. 4 pertain mainly to dust emission, optical properties and polarization, the relevant parameters will include the grain composition, size distribution, shape and structure.

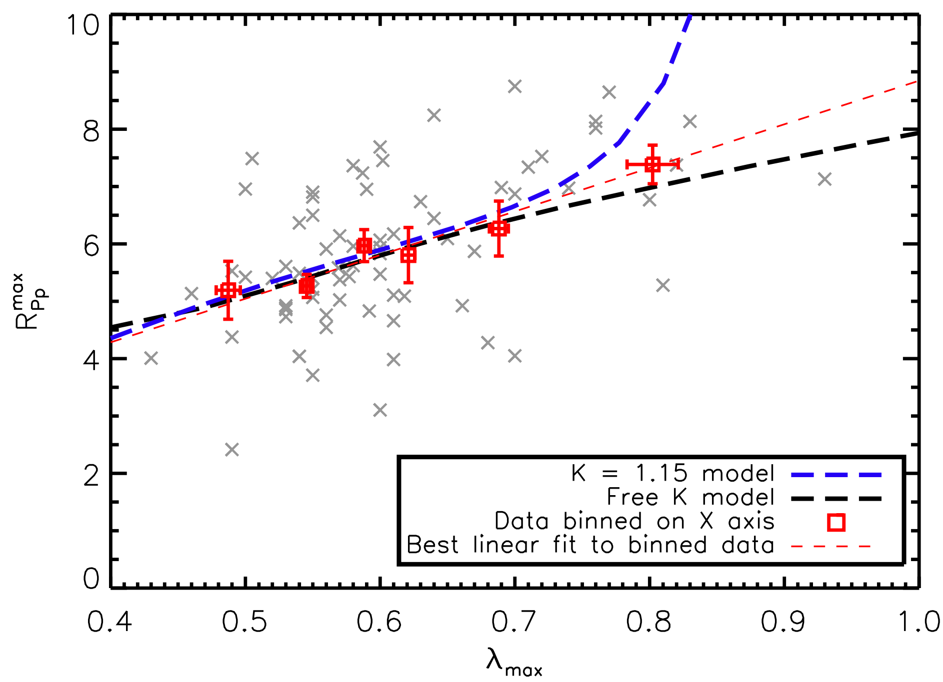

Fig. D.1. $R^{max}_{\mathrm{P/p}}$ as a function of $\lambda_{\max}$ after binning (red squares): the correlation is now much more evident. A linear fit on the binned data (red dashed line) comes close to one of the dust alignment models already presented on the right side of Fig. 4.12 (black and blue dashed lines). Unbinned data are shown in grey.

In the comparison between two quantities the choice of which one counts as X and which counts as Y is arbitrary, so we are free to choose whether to bin on X or on Y. We decided to bin over the quantity that has the smallest relative error; thus, we binned over X ($\lambda_{\max}$) when testing for the $R^{max}_{\mathrm{P/p}}$ vs. $\lambda_{\max}$ correlation and over Y ($\lambda_{\max}$ again) for the $\lambda_{\max}$ vs. dust evolution correlation. However, in the case of $R^{max}_{\mathrm{P/p}}$ vs. I/A_{V} the uncertainties are not univocally larger for one of the quantities, so we chose to test the binning on both X and Y.

D.2 k-test

If there is a trend in a data set (X,Y) we expect that the data distribution in Y will be markedly different at low X and at higher X. One can test the presence of a trend by choosing a threshold value X_{thr}, dividing the data in two groups – those with $X < X_{\mathrm{thr}}$ and those with $X > X_{\mathrm{thr}}$ – and comparing the two groups to see whether they have the same distribution.

The χ^2 two-sample test, or $k - test$, is used to check whether or not k different data samples follow the same distribution (Wall & Jenkins 2012). Each sample is binned in r different bins: this results in a $k \times r$ table, with occupation values O_{ij}, i being the index on r and j being the index on k. In our case, the k samples are the two groups with $X < X_{\mathrm{thr}}$ and $X > X_{\mathrm{thr}}$, while the binning is on Y and we chose $r = 3$.

Under the hypothesis H_0 that the k samples are identically distributed, we can compute the expectation values E_{ij}:

$$E_{ij} = \frac{\sum_{j=1}^{k} O_{ij} \sum_{i=1}^{r} O_{ij}}{\sum_{j=1}^{k} \sum_{i=1}^{r} O_{ij}} \tag{D.1}$$

If the difference between O_{ij} and E_{ij} is too high, the hypothesis H_0 of identical distribution is falsified. If we have enough data in each bin – in practice, if $O_{ij} > 5$ for each i, j – the variance will be distributed as a χ^2 with $(k-1)(r-1)$ degrees of freedom (2 in our case). We can then compute

$$\chi^2 = \sum_{j=1}^{k} \sum_{i=1}^{r} \frac{(E_{ij} - O_{ij})^2}{E_{ij}} \tag{D.2}$$

and check that its value is superior to a certain threshold to reject H_0 (if one requires *e.g.* a confidence of 99%, we need the χ^2 with 2 degrees of freedom to be 9.21 or more). Note that this test does not required that the distribution be known.

Appendix E

Résumé de la thèse en français

Les poussières interstellaires sont une composante clé du milieu interstellaire (MIS). Elles jouent non seulement un rôle important dans la physique et la chimie du MIS, mais elles servent également de traceur, du gaz *via* leur émission thermique, et du champ magnétique interstellaire *via* la polarisation de cette émission. Leur compréhension est donc importante pour l'tude de la structure et de la dynamique du MIS. De nombreux modèles de poussières ont été créé qui reproduisent les principales observables sur les poussières (la courbe d'extinction, la distribution spectrale d'énergie (SED), la polarisation en extinction), tout en respectant les abundances cosmiques élémentaires.

Notre compréhension des poussières reste cependant toujours incomplète, en particulier sur l'origine physique des variations observées de la dépendance spectrale de l'extinction et de l'émission des poussières dans le MIS. Que l'opacité des poussières soit différente dans le milieu diffus et dans les nuages moléculaires, cela est bien établi, et des modèles physiques d'interprétation ont été proposés. Avec ses cartes de l'émission submillimétrique de tout le ciel à plusieurs longueurs d'onde, le survey submillimétrique de *Planck* nous permet pour la première fois de mesurer la température des poussières dans le milieu diffus, et ainsi d'étudier les variations d'opacité des poussières. Cette thèse, basée sur une comparaison des données *Planck* avec des mesures, combine modélisation et analyse de données, afin de contraindre les variations des propriétés optiques des poussières dans le MIS diffus, et d'estimer les contributions respectives de l'alignement et de l'évolution des poussières à leur émission polarisée.

La première partie de la thèse se focalise sur l'émission non polarisée des poussières dans le MIS diffus: en partant de l'hypothèse que les matériaux carbonés dans les poussières sont sous forme de carbone amorphe hydrogéné, ou a-C(:H), on explore la possibilité que l'évolution de ces matériaux soit à l'origine des variations de propriétés des poussières. Les processus étudiés sont l'accretion du carbone de la phase gazeuse sur les grains, et surtout le *photoprocessing*, *c.a.d.* la transformation du carbone aliphatique en aromatique suite à la perte d'hydrogène causé par le rayonnement UV interstellaire. Nous utilisons le modèle $\mathrm{optEC_{(s)}(a)}$ pour les matériaux carbonés: ce modèle, développé et présenté dans Jones (2012a,b,c), permet de calculer les propriétés optiques des a-C(:H) en fonction de leur niveau d'aromatisation et de la taille du grain. Deux modèles utilisant $\mathrm{optEC_{(s)}(a)}$ ont été examinés: Jones et al. (2013) ou J13, et une version modifiée du modéle de poussières de Compiègne et al. (2011), appelée “hybride”, où le carbone amorphe a été changé en $\mathrm{optEC_{(s)}(a)}$.

On a simulé l'évolution des poussières en faisant varier le niveau d'aromatisation et l'accrétion de carbone sur les grains, et on a ainsi obtenu des simulations des différentes observables des poussières: la température T, l'indice spectrale β et la profondeur optique τ à 250 μm. La Fig. E.1 compare les corrélations entre les observables simulées et les observables de *Planck*. Deux remarques s'imposent. D'une part, les résultats sont très dependants du modèle utilisé, avec des tendances inverses. D'autre part, aucun des deux modèles n'arrive à reproduire toutes les corrélations observées.

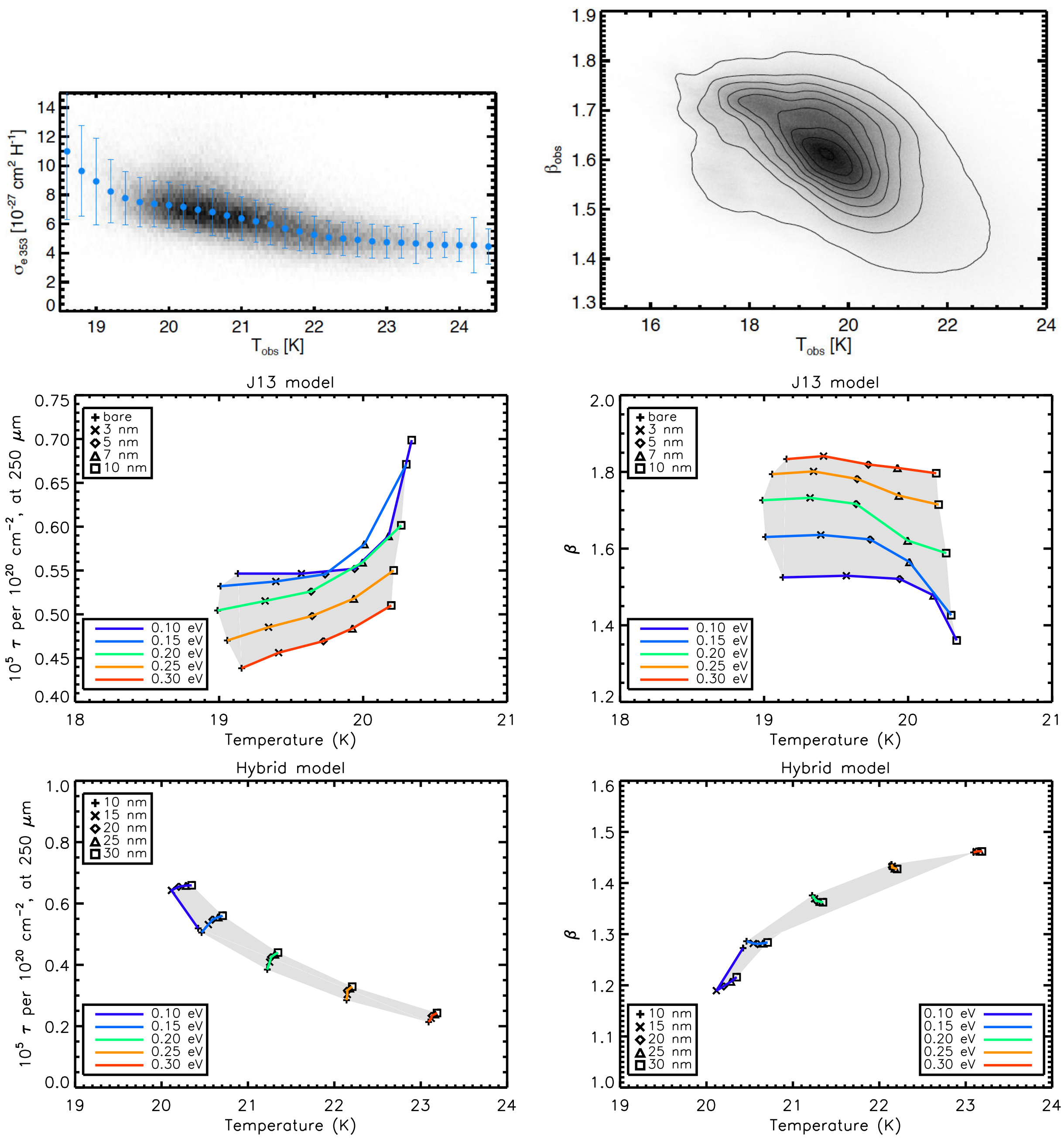

Fig. E.1. *Gauche*: relation entre la température des poussières T et l'opacité à 250 μm normalisé par $N_{\rm H}$ ($\sigma = \tau/N_{\rm H}$). L'anticorrélation observée (*haut*) n'est pas reproduite par la modèle J13 (*milieu*), mais elle est bien reproduite par la modèle hybride (*bas*). *Droite*: relation entre la température des poussières T et l'indice de refraction β. L'anticorrélation observée (*haut*) est bien reproduite par la modèle J13 (*milieu*), mais pas par la modèle hybride (*bas*).

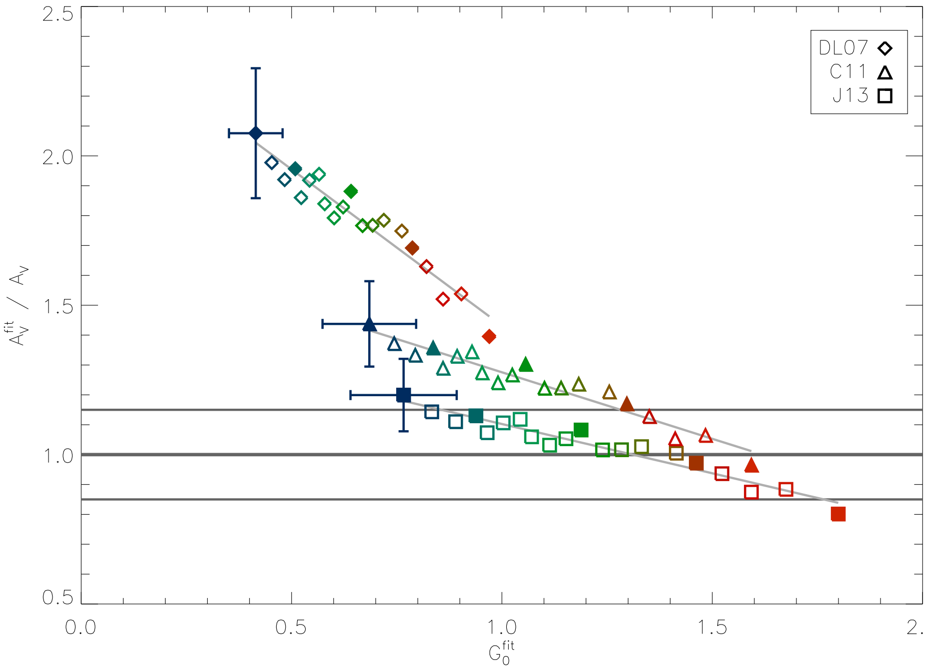

Fig. E.2. Résultats des fit des SED: l'intensité estimée du rayonnement interstellaire $G_0^{\rm fit}$ et le rapport entre l'$A_{\rm V}$ du modèle et l'$A_{\rm V}$ observé, $A_{\rm V}^{\rm fit}/A_{\rm V}$. Idéalement, les modèles devraient obtenir $A_{\rm V}^{\rm fit}/A_{\rm V} = 1$; cette image montre qu'ils ont des performances très différentes. Les performances dependent aussi de la température (rouge = chaud, bleu = froid), ce qui signifie que le poussière à températures différentes a des propriétés différentes.

Dans une deuxième partie, nous avons essayé de séparer ce qui, dans les variations d'émission des poussières, est attribuable aux variations du champ de rayonnement de ce qui est attribuable aux variations des propriétés optiques des poussières. Planck Collaboration Int. XXIX (2014) a synthétisé les variations observées de la SED des poussières sous la forme d'une famille de 20 SEDs de température croissante, normalisées en extinction en bande V. Nous effectuons des fit sur ces 20 SEDs à l'aide de trois modèles de poussière (Draine & Li 2007; Compiègne et al. 2011; Jones et al. 2013, ou DL07, C11 et J13). Chaque modèle reproduit bien la forme des SEDs, pour des valeurs de l'intensité du champ de rayonnement interstellaire (G_0) et de l'extinction des poussières en bande V ($A_{\rm V}$) qui dépendent des propriétés optiques employées par le modèle. L'$A_{\rm V}$ estimé par le fit ($A_{\rm V}^{\rm fit}$) est ensuite comparé à l'$A_{\rm V}$ observé comme montré sur la Fig. E.2 pour les trois modèles. D'une part, les modèles ont des performances très différentes, et le meilleur accord entre modèle et observations est obtenu pour le modèle utilisant les grains plus émissifs Jones et al. (2013) dont les propriétés optiques sont basées sur des données de laboratoires portant sur les silicates et carbones amorphes. D'autre part, pour tous les modèles l'écart entre modèle et observations est corrélé avec la température, ce qui démontre que l'opacité submillimétrique des poussières varie dans le milieu diffus.

Une conséquence du biais des modèles est que l'intensité G_0 du champ de rayonnement obtenue par un fit de la SED est biaisé comme l'est $A_{\rm V}^{\rm fit}$. Nous proposons un nouvel estimateur de l'intensité du rayonnement interstellaire dérivé de l'intégrale de la SED par unité d'$A_{\rm V}$, qui s'avère moins biaisé que celui obtenu par le fit. Aucun des modèles n'arrive cependant à reproduire les variations des SEDs partir de ce nouveau G_0. À l'aide de ce nouvel estimateur, nous démontrons que la variation des propriétés optiques et de l'intensité du rayonnement interstellaire ont des contributions

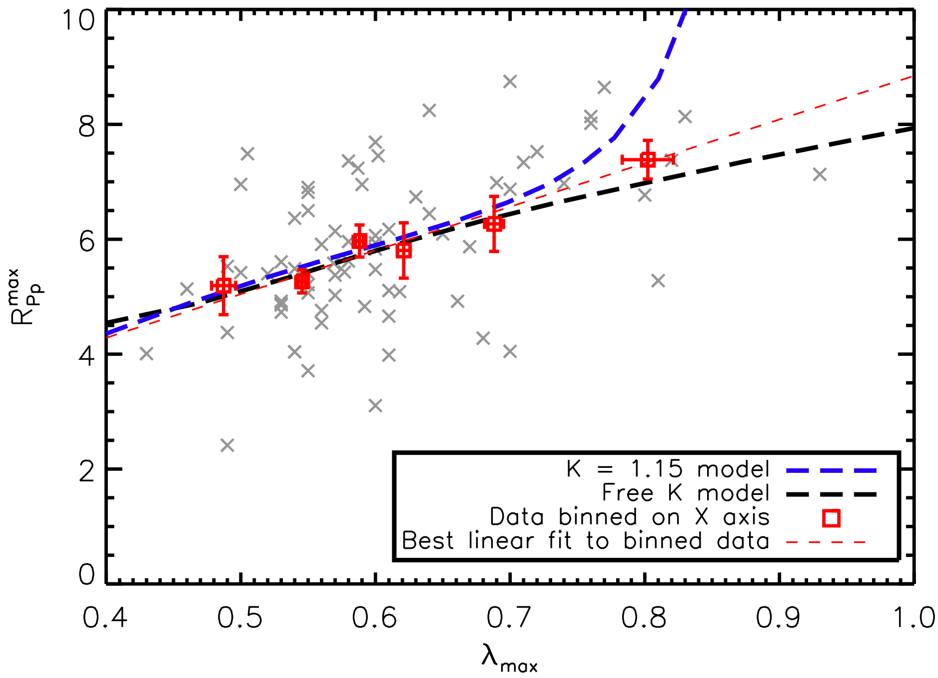

Fig. E.3. Les données observationnels pour $\lambda_{\max}$ et $R_{\mathrm{P/p}}^{max}$ (croises grises), comparées aux résultats du modèle. Deux versions du modèle sont montrées: avec K fixé à 1.15 (ligne bleue), et laissé comme paramètre libre (ligne noire). Les carrés rouges montrent les données binnées en $\lambda_{\max}$, ce qui met en évidence la corrélation. La ligne rouge pointillée montre le fit aux données binnées, qui est très proche de un des modèles.

comparables aux variations observées des SED dans le MIS diffus.

La partie finale de la thèse se focalise sur l'extinction et l'émission polarisées des poussières dans les nuages moléculaires translucents. En combinant des données polarisées *Planck* et des observations de la polarisation stellaire à un modèle de poussières, nous trouvons une corrélation entre le rapport de la polarisation en émission au maximum de polarisation en extinction, $R_{\mathrm{P/p}}^{max} = P_{353\,\mathrm{GHz}}/p_{\max}$, et la longueur d'onde de polarisation maximale en extinction, $\lambda_{\max}$, qui trace la taille typique des grains alignés. A l'aide d'un nouveau modèle de poussières basé sur les données *Planck*, nous démontrons que la variation de la taille minimale des grains alignés suffit à elle seule à reproduire la corrélation observée, sans avoir à modifier ni la distribution en taille ni les propriétés optiques des poussières. Ce modèle prédit de plus des tendances compatibles avec la chute observée des fractions de polarisation avec $\lambda_{\max}$ (Fig. E.3). D'autres interprétations ne sont cependant pas exclues.

Bibliography

Aden, A. L. & Kerker, M. 1951, Journal of Applied Physics, 22, 1242

Alata, I., Cruz-Diaz, G. A., Muñoz Caro, G. M., & Dartois, E. 2014, A&A, 569, A119

Allamandola, L. J., Tielens, A. G. G. M., & Barker, J. R. 1985, ApJ, 290, L25

Amari, S., Lewis, R. S., & Anders, E. 1995, Geochim. Cosmochim. Acta, 59, 1411

Anders, E. & Zinner, E. 1993, Meteoritics, 28, 490

Anderson, C. M., Weitenbeck, A. J., Code, A. D., et al. 1996, AJ, 112, 2726

Andersson, B.-G. 2012, ArXiv e-prints

Andersson, B.-G., Lazarian, A., & Vaillancourt, J. E. 2015, ARA&A, 53, 501

Andersson, B.-G. & Potter, S. B. 2007, ApJ, 665, 369

Aniano, G., Draine, B. T., Calzetti, D., et al. 2012, ApJ, 756, 138

Arnal, E. M., Morras, R., & Rizzo, J. R. 1993, MNRAS, 265, 1

Barnett, S. J. 1915, Physical Review, 6, 239

Beichman, C. A. 1987, ARA&A, 25, 521

Benoît, A., Ade, P., Amblard, A., et al. 2003, A&A, 399, L19

Benoît, A., Ade, P., Amblard, A., et al. 2004, A&A, 424, 571

Bernard, J. P., Abergel, A., Ristorcelli, I., et al. 1999, A&A, 347, 640

Berné, O., Joblin, C., Rapacioli, M., et al. 2008, A&A, 479, L41

Bocchio, M., Jones, A. P., & Slavin, J. D. 2014, A&A, 570, A32

Boggess, N. W., Mather, J. C., Weiss, R., et al. 1992, ApJ, 397, 420

Bohlin, R. C., Savage, B. D., & Drake, J. F. 1978, ApJ, 224, 132

Bohren, C. F. & Huffman, D. R. 1983, Absorption and scattering of light by small particles

Bolatto, A. D., Wolfire, M., & Leroy, A. K. 2013, ARA&A, 51, 207

Bot, C., Helou, G., Boulanger, F., et al. 2009, ApJ, 695, 469

Boulanger, F., Falgarone, E., Puget, J. L., & Helou, G. 1990, ApJ, 364, 136

Boulanger, F., Prevot, M. L., & Gry, C. 1994, A&A, 284, 956

Boulares, A. & Cox, D. P. 1990, ApJ, 365, 544

Bradley, J. P. 1994, Science, 265, 925

Cañameras, R., Nesvadba, N. P. H., Guery, D., et al. 2015, A&A, 581, A105

Cameron, A. G. W. 1973, in IAU Symposium, Vol. 52, Interstellar Dust and Related Topics, ed. J. M. Greenberg & H. C. van de Hulst, 545

Cardelli, J. A., Clayton, G. C., & Mathis, J. S. 1989, ApJ, 345, 245

Cecchi-Pestellini, C., Cacciola, A., Iatì, M. A., et al. 2010, MNRAS, 408, 535

Chandrasekhar, S. & Fermi, E. 1953, ApJ, 118, 113

Chiar, J. E., Adamson, A. J., Whittet, D. C. B., et al. 2006, ApJ, 651, 268

Clayton, D. D. & Nittler, L. R. 2004, ARA&A, 42, 39

Compiègne, M., Verstraete, L., Jones, A., et al. 2011, A&A, 525, A103

Cordes, J. M. & Lazio, T. J. W. 2003, ArXiv Astrophysics e-prints

Costantini, E., Freyberg, M. J., & Predehl, P. 2005, A&A, 444, 187

Coupeaud, A., Demyk, K., Meny, C., et al. 2011, A&A, 535, A124

Covino, E., Palazzi, E., Penprase, B. E., Schwarz, H. E., & Terranegra, L. 1997, A&AS, 122, 95

Davis, Jr., L. & Greenstein, J. L. 1951, ApJ, 114, 206

Desert, F.-X., Boulanger, F., & Puget, J. L. 1990, A&A, 237, 215

Dolginov, A. Z. & Mytrophanov, I. G. 1976, Ap&SS, 43, 257

Domgorgen, H. & Mathis, J. S. 1994, ApJ, 428, 647

Draine, B. T. 1988, ApJ, 333, 848

Draine, B. T. 2003, ARA&A, 41, 241

Draine, B. T. 2006, in IAU Joint Discussion, Vol. 11, IAU Joint Discussion, 8

Draine, B. T. 2011, Physics of the Interstellar and Intergalactic Medium

Draine, B. T., Dale, D. A., Bendo, G., et al. 2007, ApJ, 663, 866

Draine, B. T. & Flatau, P. J. 1994, Journal of the Optical Society of America A, 11, 1491

Draine, B. T. & Fraisse, A. A. 2009, ApJ, 696, 1

Draine, B. T. & Lee, H. M. 1984, ApJ, 285, 89

Draine, B. T. & Li, A. 2001, ApJ, 551, 807

Draine, B. T. & Li, A. 2007, ApJ, 657, 810

Draine, B. T. & Weingartner, J. C. 1996, ApJ, 470, 551

Draine, B. T. & Weingartner, J. C. 1997, ApJ, 480, 633

Dwek, E. 2005, in American Institute of Physics Conference Series, Vol. 761, The Spectral Energy Distributions of Gas-Rich Galaxies: Confronting Models with Data, ed. C. C. Popescu & R. J. Tuffs, 103–122

Fanciullo, L., Guillet, V., Aniano, G., et al. 2015, A&A, 580, A136

Fanciullo, L., Guillet, V., Jones, A., et al. 2013, in Proceedings of The Life Cycle of Dust in the Universe: Observations, Theory, and Laboratory Experiments (LCDU2013)., 58

Federrath, C. & Klessen, R. S. 2012, ApJ, 761, 156

Ferrière, K. M. 2001, Reviews of Modern Physics, 73, 1031

Finkbeiner, D. P., Davis, M., & Schlegel, D. J. 1999, ApJ, 524, 867

Fitzpatrick, E. L. 1999, PASP, 111, 63

Fitzpatrick, E. L. & Massa, D. 2007, ApJ, 663, 320

Fitzpatrick, E. L. & Massa, D. 2009, ApJ, 699, 1209

Gondhalekar, P. M., Phillips, A. P., & Wilson, R. 1980, A&A, 85, 272

Górski, K. M., Hivon, E., Banday, A. J., et al. 2005, ApJ, 622, 759

Greenberg, J. M. 1968, Interstellar Grains, ed. B. M. Middlehurst & L. H. Aller (the University of Chicago Press), 221

Greenberg, J. M. & Shah, G. A. 1971, A&A, 12, 250

Grenier, I. A., Casandjian, J.-M., & Terrier, R. 2005, Science, 307, 1292

Habing, H. J. 1968, Bull. Astron. Inst. Netherlands, 19, 421

Haffner, L. M., Reynolds, R. J., & Tufte, S. L. 1999, ApJ, 523, 223

Hall, J. S. 1949, Science, 109, 166

Han, J. L. & Qiao, G. J. 1994, A&A, 288, 759

Heiles, C. 2000, AJ, 119, 923

Heiles, C. & Robishaw, T. 2009, in IAU Symposium, Vol. 259, IAU Symposium, ed. K. G. Strassmeier, A. G. Kosovichev, & J. E. Beckman, 579–590

Hennebelle, P. & Iffrig, O. 2014, A&A, 570, A81

Heymann, D. & Dziczkaniec, M. 1979, in Lunar and Planetary Science Conference Proceedings, Vol. 10, Lunar and Planetary Science Conference Proceedings, ed. N. W. Hinners, 1943–1959

Hildebrand, R. H. 1988, QJRAS, 29, 327

Hiltner, W. A. 1949a, ApJ, 109, 471

Hiltner, W. A. 1949b, Science, 109, 165

Hoang, T., Lazarian, A., & Martin, P. G. 2013, ApJ, 779, 152

Høg, E., Fabricius, C., Makarov, V. V., et al. 2000, A&A, 355, L27

Hollenbach, D., Kaufman, M. J., Bergin, E. A., & Melnick, G. J. 2009, ApJ, 690, 1497

Hough, J. H., Aitken, D. K., Whittet, D. C. B., Adamson, A. J., & Chrysostomou, A. 2008, MNRAS, 387, 797

Jarosik, N., Bennett, C. L., Dunkley, J., et al. 2011, ApJS, 192, 14

Jones, A. P. 2004, in Astronomical Society of the Pacific Conference Series, Vol. 309, Astrophysics of Dust, ed. A. N. Witt, G. C. Clayton, & B. T. Draine, 347

Jones, A. P. 2012a, A&A, 540, A1

Jones, A. P. 2012b, A&A, 540, A2

Jones, A. P. 2012c, A&A, 542, A98

Jones, A. P., Duley, W. W., & Williams, D. A. 1990, QJRAS, 31, 567

Jones, A. P., Fanciullo, L., Köhler, M., et al. 2013, A&A, 558, A62

Jones, A. P. & Nuth, J. A. 2011, A&A, 530, A44

Jones, A. P., Tielens, A. G. G. M., Hollenbach, D. J., & McKee, C. F. 1994, ApJ, 433, 797

Jones, A. P., Ysard, N., Köhler, M., et al. 2014, Faraday Discussions, 168, 313

Jones, R. V. & Spitzer, Jr., L. 1967, ApJ, 147, 943

Jones, T. J., Bagley, M., Krejny, M., Andersson, B.-G., & Bastien, P. 2015, AJ, 149, 31

Jones, T. J., Klebe, D., & Dickey, J. M. 1992, ApJ, 389, 602

José, J., Hernanz, M., Amari, S., Lodders, K., & Zinner, E. 2004, ApJ, 612, 414

Kalberla, P. M. W. & Haud, U. 2015, A&A, 578, A78

Keller, L. P. & Messenger, S. 2011, Geochim. Cosmochim. Acta, 75, 5336

Köhler, M., Guillet, V., & Jones, A. 2011, A&A, 528, A96

Köhler, M., Jones, A., & Ysard, N. 2014, A&A, 565, L9

Köhler, M., Stepnik, B., Jones, A. P., et al. 2012, A&A, 548, A61

Kruegel, E. 2003, The physics of interstellar dust

Lagache, G., Abergel, A., Boulanger, F., & Puget, J.-L. 1998, A&A, 333, 709

Laureijs, R. J., Clark, F. O., & Prusti, T. 1991, ApJ, 372, 185

Lazarian, A. & Hoang, T. 2007, MNRAS, 378, 910

Lee, H. M. & Draine, B. T. 1985, ApJ, 290, 211

Leger, A. & Puget, J. L. 1984, A&A, 137, L5

Li, A. & Draine, B. T. 2001, ApJ, 554, 778

Li, A., Greenberg, J. M., & Zhao, G. 2002, MNRAS, 334, 840

Li, A., Wang, S., Gao, J., & Jiang, B. W. 2015, ArXiv e-prints

Martin, P. G. 2007, in EAS Publications Series, Vol. 23, EAS Publications Series, ed. M.-A. Miville-Deschênes & F. Boulanger, 165–188

Martin, P. G., Adamson, A. J., Whittet, D. C. B., et al. 1992, ApJ, 392, 691

Martin, P. G., Clayton, G. C., & Wolff, M. J. 1999, ApJ, 510, 905

Mathis, J. S. 1990, ARA&A, 28, 37

Mathis, J. S., Mezger, P. G., & Panagia, N. 1983, A&A, 128, 212

Mathis, J. S., Rumpl, W., & Nordsieck, K. H. 1977, ApJ, 217, 425

McKee, C. 1989, in IAU Symposium, Vol. 135, Interstellar Dust, ed. L. J. Allamandola & A. G. G. M. Tielens, 431

McKee, C. F. & Ostriker, J. P. 1977, ApJ, 218, 148

Mennella, V., Muñoz Caro, G. M., Ruiterkamp, R., et al. 2001, A&A, 367, 355

Mezger, P. G. 1990, in IAU Symposium, Vol. 139, The Galactic and Extragalactic Background Radiation, ed. S. Bowyer & C. Leinert, 63–73

Mezger, P. G., Mathis, J. S., & Panagia, N. 1982, A&A, 105, 372

Miville-Deschênes, M.-A. & Lagache, G. 2005, ApJS, 157, 302

Montier, L., Plaszczynski, S., Levrier, F., et al. 2015, A&A, 574, A136

Planck Collaboration Early I. 2011, A&A, 536, A1

Planck Collaboration Early XIX. 2011, A&A, 536, A19

Planck Collaboration Early XXIV. 2011, A&A, 536, A24

Planck Collaboration Early XXV. 2011, A&A, 536, A25

Planck Collaboration Int. IX. 2014, A&A, 571, A9

Planck Collaboration Int. XIX. 2015, A&A, 576, A104

Planck Collaboration Int. XX. 2015, A&A, 576, A105

Planck Collaboration Int. XXI. 2015, A&A, 576, A106

Planck Collaboration Int. XXII. 2015, A&A, 576, A107

Planck Collaboration Int. XXIX. 2014, ArXiv e-prints

Planck Collaboration Int. XXXII. 2014, ArXiv e-prints

Planck Collaboration Int. XXXV. 2015, ArXiv e-prints

Planck Collaboration VIII. 2014, A&A, 571, A8

Planck Collaboration VIII. 2015, ArXiv e-prints

Planck Collaboration XI. 2014, A&A, 571, A11

Planck Collaboration XIII. 2014, A&A, 571, A13

Plaszczynski, S., Montier, L., Levrier, F., & Tristram, M. 2014, MNRAS, 439, 4048

Purcell, E. M. 1979, ApJ, 231, 404

Purcell, E. M. & Pennypacker, C. R. 1973, ApJ, 186, 705

Rachford, B. L., Snow, T. P., Destree, J. D., et al. 2009, ApJS, 180, 125

Reach, W. T., Koo, B.-C., & Heiles, C. 1994, ApJ, 429, 672

Robertson, J. 1986, Advances in Physics, 35, 317

Robertson, J. & O'Reilly, E. P. 1987, Phys. Rev. B, 35, 2946

Savage, B. D. & Sembach, K. R. 1996, ARA&A, 34, 279

Schlegel, D. J., Finkbeiner, D. P., & Davis, M. 1998, ApJ, 500, 525

Schneider, D. P., Richards, G. T., Hall, P. B., et al. 2010, AJ, 139, 2360

Schneider, N., Bontemps, S., Simon, R., et al. 2011, A&A, 529, A1

Serkowski, K., Mathewson, D. S., & Ford, V. L. 1975, ApJ, 196, 261

Serra Díaz-Cano, L. & Jones, A. P. 2008, A&A, 492, 127

Shetty, R., Kauffmann, J., Schnee, S., & Goodman, A. A. 2009a, ApJ, 696, 676

Shetty, R., Kauffmann, J., Schnee, S., Goodman, A. A., & Ercolano, B. 2009b, ApJ, 696, 2234

Siebenmorgen, R., Voshchinnikov, N. V., & Bagnulo, S. 2014, A&A, 561, A82

Simmons, J. F. L. & Stewart, B. G. 1985, A&A, 142, 100

Smith, C. H., Wright, C. M., Aitken, D. K., Roche, P. F., & Hough, J. H. 2000, MNRAS, 312, 327

Smoot, G. F., Bennett, C. L., Kogut, A., et al. 1992, ApJ, 396, L1

Soifer, B. T., Neugebauer, G., & Houck, J. R. 1987, ARA&A, 25, 187

Solomon, P. M., Rivolo, A. R., Barrett, J., & Yahil, A. 1987, ApJ, 319, 730

Spitzer, L. 1998, Physical Processes in the Interstellar Medium

Spitzer, Jr., L. 1990, ARA&A, 28, 71

Stahl, O., Casassus, S., & Wilson, T. 2008, A&A, 477, 865

Stein, W. 1966, ApJ, 144, 318

Stepnik, B., Abergel, A., Bernard, J.-P., et al. 2003, A&A, 398, 551

Tauber, J. A., Mandolesi, N., Puget, J.-L., et al. 2010, A&A, 520, A1

Tielens, A. G. G. M. & Hagen, W. 1982, A&A, 114, 245

Tielens, A. G. G. M., Hony, S., van Kerckhoven, C., & Peeters, E. 1999, in ESA Special Publication, Vol. 427, The Universe as Seen by ISO, ed. P. Cox & M. Kessler, 579

van de Hulst, H. C. 1957, Light Scattering by Small Particles

van Dishoeck, E. F., Blake, G. A., Draine, B. T., & Lunine, J. I. 1993, in Protostars and Planets III, ed. E. H. Levy & J. I. Lunine, 163–241

Vanden Berk, D. E., Richards, G. T., Bauer, A., et al. 2001, AJ, 122, 549

Vrba, F. J., Coyne, G. V., & Tapia, S. 1993, AJ, 105, 1010

Wall, J. V. & Jenkins, C. R. 2012, Practical Statistics for Astronomers

Weingartner, J. C. & Draine, B. T. 2001, ApJ, 548, 296

Whittet, D. C. B. 1992, Dust in the galactic environment

Whittet, D. C. B., ed. 2003, Dust in the galactic environment

Whittet, D. C. B., Bode, M. F., Baines, D. W. T., Longmore, A. J., & Evans, A. 1983, Nature, 303, 218

Whittet, D. C. B., Gerakines, P. A., Hough, J. H., & Shenoy, S. S. 2001a, ApJ, 547, 872

Whittet, D. C. B., Gerakines, P. A., Hough, J. H., & Shenoy, S. S. 2001b, ApJ, 547, 872

Whittet, D. C. B., Hough, J. H., Lazarian, A., & Hoang, T. 2008, ApJ, 674, 304

Wilking, B. A., Lebofsky, M. J., Kemp, J. C., Martin, P. G., & Rieke, G. H. 1980, ApJ, 235, 905

Wilking, B. A., Lebofsky, M. J., & Rieke, G. H. 1982, AJ, 87, 695

Wilson, T. L. & Rood, R. 1994, ARA&A, 32, 191

Wolfire, M. G., Hollenbach, D., McKee, C. F., Tielens, A. G. G. M., & Bakes, E. L. O. 1995, ApJ, 443, 152

Wolfire, M. G., McKee, C. F., Hollenbach, D., & Tielens, A. G. G. M. 2003, ApJ, 587, 278

Wright, E. L. 1987, ApJ, 320, 818

Ysard, N., Juvela, M., Demyk, K., et al. 2012, A&A, 542, A21

Ysard, N., Köhler, M., Jones, A., et al. 2015, A&A, 577, A110

Zinner, E. 1998, Annual Review of Earth and Planetary Sciences, 26, 147

Zubko, V. G., Mennella, V., Colangeli, L., & Bussoletti, E. 1996, MNRAS, 282, 1321


Spece Caelum
Oculis Quamquam
Pulverulentis

Titre: Nouveaux aperçus sur les propriétés des poussières à partir des données *Planck* en intensité et polarisation

Mots clés: Milieu interstellaire, Poussières, Polarisation, *Planck*, Modélisation

Résumé: Les poussières interstellaires sont une composante clé du milieu interstellaire (MIS), et plusieurs modèles de poussières ont été créés pour reproduire ses principales observables, parmi lesquelles la courbe d'extinction, la distribution spectrale d'énergie (SED), et la polarisation en extinction et en émission. Malgré cela, notre compréhension des poussières reste incomplète. Entre autres questions, nous ne comprenons toujours pas l'origine des variations des propriétés optiques des poussières, car leur effet sur les observables est souvent dégéneré avec d'autres grandeurs physiques comme l'intensité du champ de rayonnement interstellaire ou la structure du champ magnétique (pour la polarisation).
Dans cette thèse, je tire profit des données du relevé submillimétrique *Planck*, qui pour la première fois nous fournit des cartes multi-longueur d'onde d'émission des poussières sur tout le ciel, y compris dans le milieu interstellaire diffus. Je compare des modèles de poussière avec ces observations et je montre que cette dégénerescence peut être partiellement levée si on étudie le rapport entre émission et extinction, plutôt que les deux séparément.
Cette thèse examine les variations des propriétés des poussières sous deux angles. À partir des variations de SED par unité d'extinction dans le MIS diffus, je quantifie les variations des propriétés optiques des poussières et de l'intensité du champ de rayonnement. En comparant extinction et émission polarisées dans les nuages translucents, j'améliore notre compréhension des rôles respectifs joués par la structure du champ magnétique sur la ligne de visée, par l'alignement des grains le long des lignes de champ et par les propriétés optiques des poussières sur les observables en polarisation.

Title: New insights on dust properties from *Planck* intensity and polarization data

Keywords: Interstellar medium, Dust, Polarization, *Planck*, Modeling

Abstract: Interstellar dust is a key component of the interstellar medium (ISM), and many dust models have been made to reproduce the main dust observables, which include extinction curve, spectral energy distribution (SED) in emission, and polarization in extinction and emission. Our understanding of interstellar dust, however, is still incomplete. In particular, the the variations in dust optical properties and their origin are not fully understood, since their contributions to dust observables is sometimes degenerate with other quantities, such as the intensity of the interstellar radiation field (ISRF) or the structure of the magnetic field (for polarization).
In this thesis I use data from the *Planck* submillimatric survey, which provides the first multi-wavelength, all-sky maps of dust emission, including the diffuse ISM. I compare these observations to dust models, and I show that the degeneracy can be partly removed by studying the ratio between dust emission and extinction, rather than each separately.
This thesis explores the variations of dust properties under two angles. Using the variations of dust SED per unit extinction in the diffuse ISM I quantify the variations in dust optical properties and in ISRF intensity. By comparing polarized extinction and emission in translucent clouds I improve our understanding on the effects played (on polarized observables) by the structure of the magnetic field, the alignment of dust grains on magnetic field lines, and the optical properties of dust, respectively.